UNIVERSITY OF COPENHAGEN
NIELS BOHR INSTITUTE

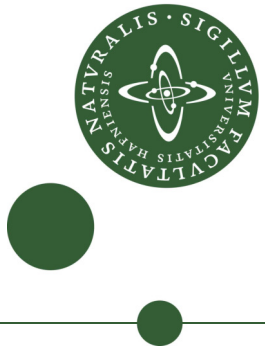

PH.D. THESIS IN PHYSICS

Mesoscopic Superconductivity towards Protected Qubits

Author:
Thorvald Wadum Larsen

Supervisor:
Charles M. Marcus

This thesis has been submitted to the PhD School of
The Faculty of Science, University of Copenhagen
October 30, 2018

Center for
Quantum
Devices

Abstract

This thesis presents results from experimental studies of three different approaches towards protected qubits based on novel semiconductor nanowires proximitized by an epitaxially grown aluminium shell.

Superconducting transmon qubits are promising candidates as building blocks in protected qubits based on quantum error correction. A Josephson junction formed in an InAs/Al core/shell nanowire exhibit a tunable Josephson energy achieved by an electrostatic gate depleting the carrier density of a semiconducting weak link region. We integrate an InAs/Al nanowire Josephson junction into a transmonlike circuit forming a gatemon. Embedding a gatemon into a microwave cavity we observe a vacuum-Rabi splitting and in the dispersive regime we measure relaxation times up to 5 μs. Additionally, we demonstrate universal control of a two-qubit device.

Next we exploit the non-cosinusoidal energy-phase relation of high-transmission, nanowire Josephson junctions in a superconducting interference device to form a 0-π qubit. The 0-π qubit can act as a fundamental building block for topologically protected qubits. Furthermore, voltage control of the semiconductor Josephson junctions creates a unique superconducting circuit allowing *in situ* tuning between widely different qubit regimes: transmon, flux, and 0-π qubit. Close to the 0-π regime we observe enhanced lifetimes indicating protected qubit states.

Finally, it has been proposed to measure the direct coupling of two separated topological phases, required for control and readout of topological qubits, in a transmonlike circuit. We demonstrate the coherence of a transmon circuit based in InAs/Al nanowire Josephson junctions surviving up to magnetic fields of 1 T sufficient to enter a topological phase. Furthermore, we present a phenomenological model for coherent modes present at high magnetic fields coupling to transmon states.

Dansk Resumé

Denne afhandling præsenterer resultater fra eksperimentelle undersøgelser af tre forskellige teknikker til fejlbeskyttede kvantebits baseret på nye halvleder nanotråde proximitized af et epitaksielt påført aluminiumslag. Superledende transmon kvantebits er lovende kandidater til byggesten i fejlbeskyttede kvantebits baseret på kvante fejlkorrektion.

En Josephson kontakt, dannet i en InAs/Al kerne/skal nanotråd, har en justerbar Josephson energi kontrolleret af en elektrostatisk gate, som formindsker tætheden af ladningsbærer i en svag halvlederforbindelse. En gatemon dannes bed at integrerer en InAs/Al nanotråd Josephson kontakt i et transmonlignende kredsløb. Ved at indsætte en gatemon i en mikrobølgeresonator observerer vi en vakuum-Rabi splittelse og i spredningsregimet måler vi levetider op til 5 μs. Derudover demonstrerer vi universel kontrol af en doublekvantebitprøve.

Efterfølgende udnytter vi det ikke-cosinusformede energi-fase forhold mellem høj transmissions nanotråde Josephson kontakter i en superledende interferens enhed til at danne en 0-π kvantebit. 0-π kvantebiten kan fungere som en grundlæggende byggesten for topologisk fejlbeskyttede kvantebits. Spændingskontrol af halvleder Josephson kontakter skaber et unikt superledende kredsløb med *in situ* tuning mellem vidt forskellige kvantebitregimer: transmon, flux, og 0-π kvantebit. Tæt på 0-π regimet observerer vi en indikation på fejlbeskyttede kvantebittilstande i form af forbedret levetid.

Endelig er det blevet foreslået at måle den direkte kobling af to adskilte topologiske faser, som kræves til kontrol og udlæsning af topologiske kvantebits, i et transmonlignende kredsløb. Vi demonstrerer at kvantekohærens i et transmon kredsløb baseret på en InAs/Al nanotråd Josephson kontakt overlever op til magnetfelter på 1 T tilstrækkeligt for at tilgå topologiske faser. Desuden præsenterer vi en fænomenologisk model for tilstande observeret ved høje magnetfelter, som kobler til transmontilstande.

Acknowledgements

My work would not have been possible without the support from countless people. First, I would like to thank my supervisor Charlie Marcus. Charlie, it has been a pleasure to work under your guidance with the possibilities to redirect my research path to new topics and challenges during my studies. It has been a privilege to work in your laboratory both due to the high-end equipment and the open culture you facilitate leading to innumerable, enjoyable discussions and collaborations.

Next, I would like to thank Karl Petersson who has been my acting co-supervisor. Thank you for introducing me to the complicated world of high-frequency measurements and superconducting qubits. I have been happy to part of transmon team since its inception guided by your thoughtful approach and attention to detail.

I am thankful to everyone in the transmon team who has supported and contributed to my work. Special thanks to Lucas Casparis, who has contributed immensely both with measurements, fabrication, and ideas. Anders Kringhøj, thank you for the amazing teamwork and for always joining my off-schedule coffee breaks. I have had a plethora of great discussions on quantum control with Natalie Pearson but somehow we manage to never agree on the details of software architectures. Also a big thanks to Rob McNeil for always bringing a smile as well as all the fabrication you have done for me. Oscar Erlandsson, thank you for selflessly letting me be part of measurements on samples you fabricated.

I would like to thank Andrew Higginbotham who taught me the ropes of experimental condensed matter physics. Also thanks to Ferdinand Kuemmeth for always providing new perspectives to measurements and always having new curious thought experiments. Misha Gershenson, thank you for sharing your expertise and many discussions on designs and measurements of novel experiments. I would like to thank Matthias Christiandl, Gorjan Alagic, and Héctor Bombín for answering countless questions in discussions and journal clubs on quantum information science. In the later part of my PhD I got the opportunity to work on topological materials together with the cQED qubit team in Microsoft. I would like thank Angela Kou and everyone else in the Delft team for a close collaboration. Also a big thanks to Bernard van Heck and the theory team in Santa Barbara for answering many unreasonably hard questions about topological materials.

My first years in QDev wouldn't have been nearly as pleasant without Christian Olsen. Thank you for the many late hours at QDev juggling interesting research and less interesting course work. We were fortunate enough to also share office with great

officemates Morten Hels and Jerome Mlack. Henri Suominen and Giulio Ungaretti thank you for many enjoyable lab dinners as well as many Wednesday traditions. Also thanks to Shivendra Upadhyay inviting me to your wedding. I would also like to thank Sven Albrecht for a nice trip to Austin. Many thanks to everyone in QDev who makes it such a great place to work and learn.

Of course a laboratory is non-functioning without the great support from technicians and secretaries who are really making the research possible. Big thanks to Shivendra Upadhyay and Dorthe Bjergskov and everyone else making this possible. Also thanks to the QCoDeS team in Copenhagen both for teaching me how to code and providing the software required in lab.

During my PhD I had the privilege of visiting Will Oliver's Lab at MIT for three months. I would like to thank Will for opportunity to visit and being immediately trusted with ongoing measurements. Also thanks to all my fellow students and researches in the group which made my stay incredibly enjoyable and educating. Especially, thanks to Morten Kjærgaard for welcoming me to Boston and the many elucidating coffee discussions. I hope I will have the opportunity for many more visits in the future.

Lastly, I would like to thank my family who has supported me throughout even when my studies seemed to take precedence over everything else.

Contents

1 Introduction **1**

1.1 Outline . . . 3

1.2 Publications . . . 4

2 Theory of Quantum Computing **5**

2.1 Quantum Bits . . . 5

2.2 Qauntum Error Correction . . . 9

2.3 Passive Error Correction . . . 13

2.4 Topological Material . . . 14

2.5 Fault-Tolerant Quantum Computing . . . 17

3 Circuit Quantum Electrodynamics **19**

3.1 Quantized Harmonic Oscillators . . . 20

3.2 Artificial Atoms in Superconducting Circuits . . . 22

3.3 Semiconductor Based Josephson Junctions . . . 26

3.4 Coupled Artificial Atoms and Harmonic Oscillators . . . 29

3.5 Single Qubit Control . . . 33

3.6 Two-Qubit Operations . . . 34

4 Fabrication and Experimental Setup **38**

4.1 Fabrication . . . 38

4.2 Experimental Setup . . . 39

5 Semiconductor-Based Superconducting Qubits **41**

5.1 The Gatemon . . . 41

5.2 Gatemon Benchmarking and Two-Qubit Operations . . . 49

5.3 Conclusion . . . 53

6 A Superconducting 0-π Qubit Based on High Transmission Josephson Junctions **54**

6.1 Supplementary Information . . . 63

7 High field compatible transmon circuit **65**

7.1 Coherent Control up to 1 T . . . 67

7.2 Coupled Qubit and Junction states . . . 71

7.3 Conclusion 71

8 Outlook **74**

Appendices **76**

A Second order perturbation theory **77**

B Magnetic field response of NbTiN resonator **79**

C Schematics of Experimental Setups **80**

D Fabrication Recipes **85**

D.1 Single qubit devices presented in Chapter 5 85

D.2 Two-qubit device presented in Chapter 5 86

D.3 Device presented in Chapter 6 87

D.4 Device presented in Chapter 7 88

Bibliography **90**

List of Figures

2.1 The Bloch Sphere . . . 6
2.2 Qubit State Rotation. . . . 7
2.3 Single-qubit Clifford gates . . . 8
2.4 Qunatum teleportation circuit . . . 9
2.5 The Surface Code. . . . 12
2.6 Passive Error Correction. . . . 13
2.7 The Kitaev Chain. . . . 15
2.8 Majorana Nanowire. . . . 16
2.9 Error Propagation in CNOT. . . . 17

3.1 An LC resonant circuit. . . . 20
3.2 A distributed microwave cavity. . . . 21
3.3 Schematic of a Josephson junction . . . 23
3.4 The transmon circuit . . . 24
3.5 Transmon energy spectrum . . . 25
3.6 Schematic of a semiconductor Josephson junction . . . 27
3.7 The nanowire Josphson junction . . . 28
3.8 Potentials of Josephson junctions . . . 29
3.9 Transmon-resonator circuit . . . 30
3.10 Resonant Jaynes-Cummings energy levels . . . 31
3.11 Jaynes-Cummings energy spectrum in dispersive regime . . . 32
3.12 Two transmon qubits coupled capacitively. . . . 35
3.13 Two transmon qubits coupled via a resonator. . . . 35
3.14 Two-qubit energy spectrum . . . 37

5.1 Physical realization of a gatemon . . . 43
5.2 Vacuum-Rabi splitting of a gatemon-cavity system . . . 45
5.3 Gatemon spectroscopy . . . 45
5.4 Coherent gatemon manipulation . . . 46
5.5 Gatemon coherence . . . 48
5.6 Optical image of a two-qubit sample . . . 50
5.7 Single Qubit Gate Benchmarking . . . 51
5.8 Qubit-Qubit coupling of gatemons . . . 52

5.9 Controlled Phase Gate 53

6.1 Circuit schematic and 0-π qubit 55
6.2 Qubit Spectroscopy as a function of flux 57
6.3 Voltage control of middle barrier 59
6.4 Coherent control 60
6.5 Qubit relaxation time 61
6.6 Energy spectrum 64
6.7 Charge matrix elements 64

7.1 Energy states 66
7.2 Sample schematic 67
7.3 Majorana transmon in magnetic field 68
7.4 Low field coherence 69
7.5 Coherence of Majorana transmon at $B = 1$ T 70
7.6 Junction states vs magnetic field 72
7.7 Gate dependence of junction states 72

B.1 NbTiN resoantor response as a function of magnetic field. 79

C.1 Measurement setup Chapter 5 – single qubit devices. 81
C.2 Measurement setup Chapter 5 – two qubit device. 82
C.3 Measurement setup Chapter 6. 83
C.4 Measurement setup Chapter 7. 84

Chapter 1

Introduction

The continued digital transformation of society since the invention of the transistor [1, 2] and the integrated circuit [3] has been driven by Moore's law stating that the number of transistors per area will grow exponentially [4]. However, as Moore's law is coming to an end, due to the size of transistors reaching physical limitations, several problems are still thought intractable even on tomorrow's supercomputers. One such problem is the accurate simulation of large quantum systems with applications in drug development, chemical reactions, materials science as well as general understanding of nature. Realizing the potential of quantum simulaitons Richard Feynman proposed a new type of computer, a quantum computer, capable of simulating nature [5]. Since then several concrete algorithms has been proposed with widespread applications for molecule simulations [6, 7], machine learning [8], and database searching [9]. Most notably in 1994 Peter Shor published a quantum algorithm efficiently breaking RSA encryption [10] exemplifying the widespread influence of a quantum computer on society.

A digital quantum computer is based on replacing the classical bit with a quantum bit (qubit), a quantum mechanical two-level system. This allows the information itself of a computation to be in entangled superposition states opening new possibilities in algorithms. A modest 300 qubit quantum computer can work with 2^{300} different states simultaneously - that is more states than there are atoms in the universe! While qubits allows new algorithms they also introduce new sources of errors. The challenge lies in building a qubit decoupled from any noise but easily manipulated to perform computations. Several qubit platforms are actively being investigated: ion traps [11–13], superconducting qubits [14–18], spin-qubits [19, 20], and topological material [21–25] among many others. Qubit performance continues to improve dramatically each year but orders of magnitude better qubits are required for a fully functional quantum computer.

The next milestone is the development of a topologically protected qubits in which the control mechanisms are topologically different from noise sources. The goal is to encode a qubit into a non-local degree of freedom which is exponentially decoupled from local noise sources as the system size is increased. Topological protection can be achieved via quantum error correction [26–28], passive quantum error correction [29], or topological materials [30]. This thesis investigates each approach to protected qubits in mesoscopic super-

conducting devices incorborating hybrid InAs-Al semiconductor-superconductor nanowires [31].

The basic idea of quantum error correction is to confine the Hilbert space of a multi-qubit system to a non-local subspace by local measurements. Any local noise is then detectable from the eigenvalues of the local measurements protecting the non-local subspace. State-of-the-art superconducting qubits are rapidly approaching a quality and quantity sufficient for quantum error correction [32–34]. Mesoscopic, condensed matter systems are promising candidates for error corrected qubits due to the potential for scalability by leveraging existing fabrication technology from the semiconductor industry. In this thesis we investigate hybrid semiconductor-superconductor qubits, gatemons, combining field effect tunable semiconductors with dissipationless superconductors. Superconducting qubits are anharmonic resonant circuits formed by a Josephson junction shunted by a capacitor. In gatemons the Josephson junctions are created from proximitized semiconductor materials allowing *in situ* voltage tuning of qubit parameters.

Passive quantum error correction similarly relies on confining a subspace spanned by non-local degrees of freedom. However, instead of confining the subspace by active measurements a Hamiltonian is designed to inherently form degenerate non-local ground states. Each measurement of an error correcting code is replaced by an energy gap in the Hamiltonian which act as a passive measurement by the system itself. The Hamiltonian will have non-local, degenerate ground states isolated from local noise due to an energy gap. A fundamental element required to engineer such systems are qubits with degenerate ground states. Ongoing investigations relie on superconducting circuits with insulator junctions [35–37]. Hybrid semiconductor-superconductor junction introduces a new circuit element similar to insulator junction but with crucial differences due to the high mobility of semiconductors. We explore simple mesoscopic circuit architectures utilizing high-transmission junctions for protected qubits.

The specific material combination of one-dimensional InAs/Al, which has a strong spin-orbit coupling and superconductivity has long been investigated as a topological material hosting non-local excitations. For topological materials the non-local nature of excitations is achieved on the microscopic level of electron-electron interactions. In this thesis we develop a superconducting circuit, taking advantage of control techniques from superconducting qubits, designed to probe the coupling of topological phases essential for control and readout of topological qubits. We demonstrate that coherent superconducting circuits be realized with control circuitry and high magnetic fields required for topological qubits in InAs/Al nanowires.

This PhD thesis is written as part of the so-called integrated (4+4)PhD program at University of Copenhagen. Thus, parts of Chapter 3 and 5 presented in this thesis also appear in the authors master thesis (reference [38]). We note that this practice is consistent with the spirit and regulations of the integrated PhD program.

1.1 Outline

The outline of this thesis is as follows:

In Chapter 2 we introduce the basics of qubits and quantum information as well as the theory of protected qubits. The theory of mesoscopic harmonic oscillators and artificial atoms in superconducting circuits, circuit quantum electrodynamics, is presented in Chapter 3. Furthermore, the semiconductor-superconductor Josephson junction and its characteristics is introduced. Chapter 4 gives a description of the fabrication flow for each sample as well as a overview of the experimental setup and measurement techniques. In Chapter 5 the development of the gatemon qubit is presented and single and two-qubit operations are benchmarked. The first steps towards protected qubits with passive quantum error correction based on high-transmission Josephson junction are presented in Chapter 6. We show that degenerate qubits can be formed with signatures of protected states. Lastly, in Chapter 7 we introduce a high magnetic field compatible superconducting qubit for detection of topological phases. Chapter 8 gives an outlook on the field of experimental quantum computing.

1.2 Publications

The work during the thesis project has resulted in the following publications.

- **T. W. Larsen***, K. D. Petersson*, F. Kuemmeth, T. S. Jespersen, P. Krogstrup, J. Nygård & C. M. Marcus.
"Semiconductor-Nanowire-Based Superconducting Qubit"
Physical Review Letters **115**, 127001 (2015).

- C. M. Marcus, P. Krogstrup, K. D. Petersson, T. S. Jespersen, J. Nygård, **T. W. Larsen** & F. Kuemmeth.
"Semiconductor Josephson Junction and a Transmon Qubit Related Thereto"
US Patent Application US20170133576A1.

- L. Casparis, **T. W. Larsen**, M. S. Olsen, F. Kuemmeth, P. Krogstrup, J. Nygård, K. D. Petersson & C. M. Marcus.
"Gatemon Benchmarking and Two-Qubit Operations"
Physical Review Letters **116**, 150505 (2016).

- A. Kringhøj, L. Casparis, M. Hell, **T. W. Larsen**, F. Kuemmeth, M. Leijnse, K. Flensberg, P. Krogstrup, J. Nygård, K. D. Petersson & C. M. Marcus.
"Anharmonicity of a superconducting qubit with a few-mode Josephson junction"
Physical Review B **97**, 060508 (2018).

- L. Casparis, N. J. Pearson, A. Kringhøj, **T. W. Larsen**, F. Kuemmeth, J. Nygård, P. Krogstrup, K. D. Petersson & C. M. Marcus.
"Voltage-Controlled Superconducting Quantum Bus"
ARXIV:1802.01327, *submitted*.

- L. Casparis, M. R. Connolly, M. Kjaergaard, N. J. Pearson, A. Kringhøj, **T. W. Larsen**, F. Kuemmeth, T. Wang, C. Thomas, S. Gronin, G. C. Gardner, M. J. Manfra, C. M. Marcus & K. D. Petersson.
"Superconducting gatemon qubit based on a proximitized two-dimensional electron gas"
Nature Nanotechnology **13**, 915 (2018).

- N. J. S. Loft, M. Kjaergaard, L. B. Kristensen, C. K. Andersen, **T. W. Larsen**, S. Gustavsson, W. D. Oliver & N. T. Zinner.
"High-fidelity conditional two-qubit swapping gate using tunable ancillas"
ARXIV:1809.09049, *submitted*.

- **T. W. Larsen**, L. Casparis, A. Kringhøj, N. J. Pearson, R. P. G. McNeil, F. Kuemmeth, M. E. Gershenson, P. Krogstrup, J. Nyård, C. M. Marcus & K. D. Petersson.
"A Superconducting 0-π Qubit Based on High Transmission Josephson Junctions"
In preparation.

* These authors contributed equally.

Chapter 2

Theory of Quantum Computing

In this chapter we first introduce the mathematical concept of a qubit, qubit operations and a simple quantum algorithm. Next we introduce the each of the different approaches to topological protection necessary for practical quantum computing.

2.1 Quantum Bits

A classical bit is some physical system that can take two values commonly denoted as 0 and 1. In computers calculation are performed on bits of information represented by *low* or *high* voltage with a threshold voltage defining if it is 0 or 1.

A quantum bit, or qubit, is some quantum system that has two linearly independent states commonly denoted as $|0\rangle$ and $|1\rangle$. While a bit can only be in two states the state of a qubit, $|\psi\rangle$, can be any linear combination of $|0\rangle$ and $|1\rangle$:

$$|\psi\rangle = \alpha|0\rangle + \beta|1\rangle, \tag{2.1}$$

where α and β are complex numbers normalized by $|\alpha|^2 + |\beta|^2 = 1$. The state of an isolated single qubit can be parametrized by three real numbers

$$|\psi\rangle = e^{i\gamma}\left(\cos\frac{\theta}{2}|0\rangle + e^{i\varphi}\sin\frac{\theta}{2}|1\rangle\right). \tag{2.2}$$

As the global phase of the state, γ, is not observable in a single qubit system we can ignore this factor. We are left with two numbers θ and ϕ which can be visualized as a points on a sphere - the Bloch sphere. Figure 2.1**A** visualizes the Bloch sphere with state $|\psi\rangle$ marked as a point. The Bloch sphere is an incredibly powerful tool for understanding single-qubit operations. An operation U applied to state $|\psi\rangle$ can represented as a rotations (up to a global phase) of the qubit state on the Bloch sphere [Figure 2.1**B**].

The qubit state can be at any point on the Bloch sphere but when measured the qubit will only take one of two values. A projective measurement of the eigenvalue of

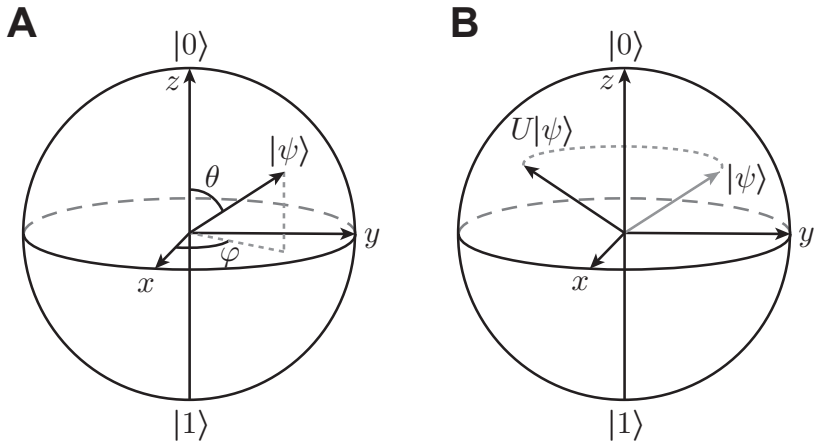

Figure 2.1: **A** The qubit state $|\psi\rangle$ represented on the Bloch Sphere. **B** Any single-qubit operation U can up to a global phase be visualized as a rotation of the qubit state on the Bloch sphere.

$\hat{\sigma}_z = |0\rangle\langle 0| - |1\rangle\langle 1|$ will yield $+1$ with probability $|\alpha|^2$ and -1 with probability $|\beta|^2$.

The Hamiltonian describing the time-evolution of the qubit state is ideally given by:

$$\widehat{H} = 0, \tag{2.3}$$

that is the qubit state is a constant in time[1]. A qubit operation can be described as a controlled time-evolution by changing the Hamiltonian. Without loss of generality we can decompose the Hamiltonian into three independent terms:

$$\widehat{H} = \hbar\frac{\Omega_x(t)}{2}\hat{\sigma}_x + \hbar\frac{\Omega_y(t)}{2}\hat{\sigma}_y + \hbar\frac{\Omega_z(t)}{2}\hat{\sigma}_z, \tag{2.4}$$

where $\hat{\sigma}_i$ are Pauli matrices and $\Omega_i(t)$ describes the applied operation. A rotation around the x axis shown in Figure 2.2 can be induced by setting $\Omega_x(t) = \Omega$ while keeping $\Omega_y(t) = \Omega_z(t) = 0$. The time evolution of the qubit state is then given by:

$$R_x(\Omega t)|\psi\rangle = e^{-i\frac{\Omega t}{2}\hat{\sigma}_x}|\psi\rangle = \left[\cos\frac{\Omega t}{2}\mathbb{1} - i\sin\frac{\Omega t}{2}\hat{\sigma}_x\right]|\psi\rangle = \begin{bmatrix}\cos\frac{\Omega t}{2} & -i\sin\frac{\Omega t}{2}\\ -i\sin\frac{\Omega t}{2} & \cos\frac{\Omega t}{2}\end{bmatrix}|\psi\rangle. \tag{2.5}$$

After a time t the qubit will have rotated an angle Ωt around the x axis of the Bloch sphere. For example for $\Omega t = \pi$ the rotation applies the operation $-i\hat{\sigma}_x|\psi\rangle = -iX|\psi\rangle$, where X is the conventional notation for the Pauli matrix σ_x in computer science. Similarly rotations can be induced around y and z by Ω_y and Ω_z respectively. Practically it is enough to implement control of just two orthogonal axes as any single-qubit operation can be decomposed as $U = e^{i\alpha}R_x(\beta)R_y(\gamma)R_x(\delta)$, where α, β, γ, and δ are real numbers [39].

Multi qubit systems has many of the same properties as a single qubit. The system state now has four linearly independent states often represented in the computational

[1]In practice $\widehat{H} = 0$ is often described in a rotating frame of reference.

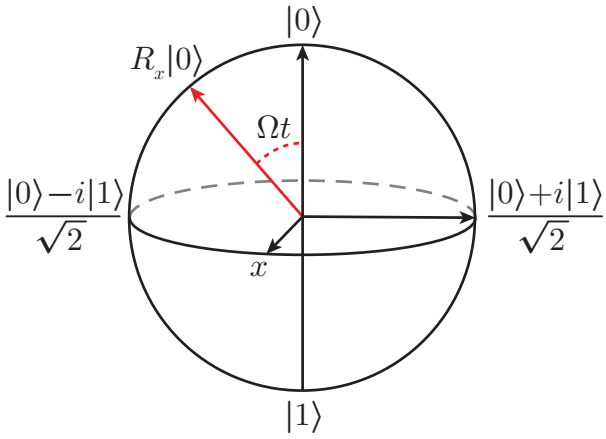

Figure 2.2: Induced rotation of initial qubit state $|0\rangle$ with $R_x = e^{-i\frac{\Omega t}{2}\sigma_x}$. After a time t the state will have rotated an angle Ωt around the x-axis.

basis as

$$|\psi_2\rangle = \alpha_{00}|00\rangle + \alpha_{01}|01\rangle + \alpha_{10}|10\rangle + \alpha_{11}|11\rangle, \tag{2.6}$$

where α_{ij} are complex numbers. Unfortunately, a visual representation of a two-qubit state would require a 7-dimensional space. Universal control of a two-qubit system can be achieved with universal single-qubit gates and one entangling two-qubit gate [40]. Practically, this is an incredibly important result as only a single type of qubit-qubit coupling needs to be designed and optimized. The specific gate being implemented depends on the details of the system.

A common group of gates, which plays an important role for protected qubits, is the Clifford group. The group of Clifford gates is generated by the gate set[2]:

$$H = \frac{1}{\sqrt{2}}\begin{bmatrix}1 & 1\\ 1 & -1\end{bmatrix}, S = \begin{bmatrix}1 & 0\\ 0 & i\end{bmatrix}, \text{CNOT} = \begin{bmatrix}1 & 0 & 0 & 0\\ 0 & 1 & 0 & 0\\ 0 & 0 & 0 & 1\\ 0 & 0 & 1 & 0\end{bmatrix}, \tag{2.7}$$

where CNOT is the controlled-not gate. The controlled-not gate, also sometimes referred to as CX (controlled X), performs an X gate on a target qubit dependent on the state of a control qubit, e.g. $\text{CNOT}_{01}|10\rangle = |11\rangle$ where subscript 01 refers to index 0 and 1 of control qubit and target qubit respectively. The Clifford group for a single qubit can be visualized as any gate that preserves the octahedron of the Bloch sphere as shown in Figure 2.3. There are 24 gates in the single-qubit Clifford group - the number of orientations the octahedron can take. The two-qubit Clifford group has 11,520 elements [41].

Having introduced qubits and gates we can now look at a simple non-trivial circuit taking advantage of the quantum mechanical nature: teleportation of quantum informa-

[2]A group generated by a set of generators means that any element in the group can be expressed as a finite combination of elements from the generating set.

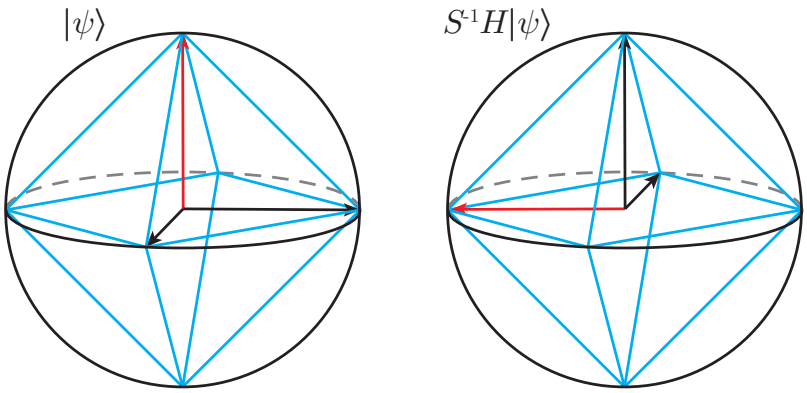

Figure 2.3: Single qubit Clifford gates will rotate the octahedron from one orientation to another keeping the vertices of the octahedron along the coordinate axes.

tion. Figure 2.4 depicts the 3-qubit circuit which teleports the state $|\psi\rangle = \alpha|0\rangle + \beta|1\rangle$ of qubit 1 onto qubit 3 without gaining any information about the state. The circuit consist of single qubit gates and CNOT gates as well as classical information from measurement results depicted as double lines.

First qubit 2 and 3 are put in a two-qubit entangled state, a Bell state, such the total state of the system at $|\psi_1\rangle$ is

$$|\psi_1\rangle = \text{CNOT}_{23} H_2 |\psi\rangle|00\rangle \tag{2.8}$$

$$= |\psi\rangle \frac{|00\rangle + |11\rangle}{\sqrt{2}} \tag{2.9}$$

$$= \alpha \frac{|000\rangle + |011\rangle}{\sqrt{2}} + \beta \frac{|100\rangle + |111\rangle}{\sqrt{2}}, \tag{2.10}$$

where the subscripts of the gate refers to which qubit(s) it is applied to. Next qubit 2 is entangled with qubit 1 leading to the system state

$$|\psi_2\rangle = H_1 \text{CNOT}_{12} |\psi_1\rangle \tag{2.11}$$

$$= \frac{1}{2} \left[\alpha(|000\rangle + |100\rangle + |011\rangle + |111\rangle) + \beta(|010\rangle - |110\rangle + |001\rangle - |101\rangle)\right]$$

$$= \frac{1}{2} \left[|00\rangle(\alpha|0\rangle + \beta|1\rangle) + |10\rangle(\alpha|0\rangle - \beta|1\rangle) + |01\rangle(\alpha|1\rangle + \beta|0\rangle) + |11\rangle(\alpha|1\rangle - \beta|0\rangle)\right]$$

$$= \frac{1}{2} \left[|00\rangle|\psi\rangle + |10\rangle Z|\psi\rangle + |01\rangle X|\psi\rangle + |11\rangle XZ|\psi\rangle\right]. \tag{2.12}$$

By measuring the states of qubit 1 and 2 the system will collapse into one of the four possible states in equation (2.12) leaving qubit 3 in state $|\psi\rangle$ up to a single qubit gate. Depending on the results of the two measurements correction gates are applied to qubit 3 to complete the teleportation of a still unknown state.

Teleportation is a simple algorithm with only six gates and two measurements making up the full algorithm, which state-of-the-art qubits can readily implement and run with very high efficiency [42]. However, we are far from computing larger and actually useful computations containing orders of magnitudes more gates due to non-ideal operations.

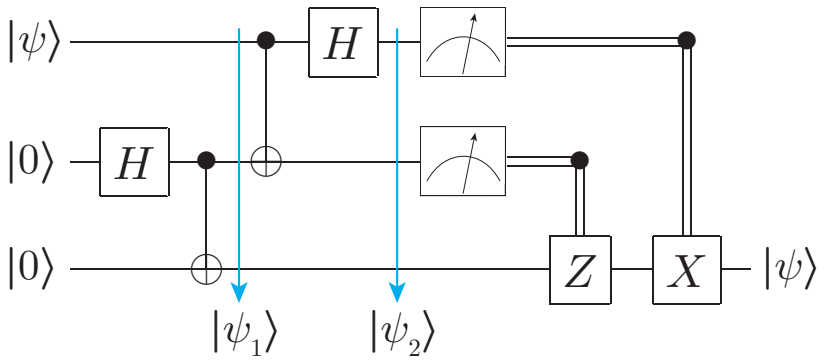

Figure 2.4: Quantum teleportation algorithm.

2.2 Qauntum Error Correction

The classical repetition code is a simple example of error correction. It takes a single bit of information and encodes it in three physical bits $\bar{1} = 111$ and $\bar{0} = 000$, where the bar notation represents the encoded (logical) information. The physical representations of the logical information, here 111 and 000, are called the codes codewords. If a bit-flip error happens on a single bit one can still decode the encoded information by taking a majority vote of all the bits. However, if two bit-flip errors happen in different bits the decoding by a majority vote will give the wrong answer. For bits with error rate ρ the three-bit repetition code will have error rate of order ρ^2 assuming the errors are independent.

One cannot directly use the same type of error correction for qubits. A repetition code relies on copying the information of one bit to several bits - a process that is impossible for qubits due to the no-cloning theorem [39]. Furthermore, to detect an error in the repetition code one has to measure all the bits which would collapse any superposition state of the qubit. Instead, quantum error correcting codes works by encoding the qubit state in a multi-qubit degree of freedom reducing many qubits to an effective two-level system [39, 43]. Error detection is achieved by measuring a specific set of multi qubit operators, also called the codes stabilizers[3], rather than single-qubit states.

The stbilizer formalism is incredibly powerfull for describing a error correcting codes [44]. A quantum state $|\psi\rangle$ is stabilized by a stabilizer S if $S|\psi\rangle = |\psi\rangle$. For a two-qubit state an example of a stabilizer could be X_1X_2 which stabilizes any linear combination of the two quantum states $\left\{\frac{|00\rangle+|11\rangle}{\sqrt{2}}, \frac{|01\rangle+|10\rangle}{\sqrt{2}}\right\}$. Here a single stabilizer X_1X_2 uniquely defines a subspace of the two-qubit Hilbert space without having to specify eigenstates spanning the subspace. This formalism turns out to be very powerful for describing quantum error-correcting codes whose quantum states becomes very long and unintuitive written in the computational basis.

Returning to the repetition code we can describe the quantum version using stabilizers. The quantum repetition code is defined by the group of stabilizers generated by $g_1 = Z_1Z_2I_3$ and $g_2 = I_1Z_2Z_3$, where I_i is the identity operator. The full group of stabilizers is

[3]Other non-stabilizer quantum error correcting codes exists but are not covered here.

formed from any combination of the generators: $\mathcal{S} = \{I_1I_2I_3, Z_1Z_2I_3, I_1Z_2Z_3, Z_1I_2Z_3\}$. The codewords of the code are then given by the quantum states stabilized by $\mathcal{S}$: $\{|000\rangle, |111\rangle\}$. The protected qubit state can be written as:

$$\left|\bar{\psi}\right\rangle = \alpha|000\rangle + \beta|111\rangle. \tag{2.13}$$

In general a quantum code made of n qubits with m generators can encode $n-m$ protected qubits[4]. Similarly to the classical version the code can detect a single bit-flip error on any qubit. By definition of stabilizers we can measure the eigenstate of any stabilizer without disturbing the encoded information: $S_i\left|\bar{\psi}\right\rangle = +1\left|\bar{\psi}\right\rangle$. Error detection can be performed by measuring the eigenvalues of stabilizers of the code. It is sufficient to measure a set of generators of the stabilizer group as the eigenvalues of other stabilizers can be computed from these. The set of measured eigenvalues is called the error syndrome.

Assume the code had a bit-flip error X_1 leaving the code in state

$$X_1|\psi\rangle = \alpha|100\rangle + \beta|011\rangle. \tag{2.14}$$

Measuring the error syndrome we find eigenvalues $g_1X_1|\psi\rangle = -X_1g_1|\psi\rangle = -X_1|\psi\rangle$ and $g_2X_1|\psi\rangle = X_1g_2|\psi\rangle = X_1|\psi\rangle$ revealing an error as a change in the eigenvalue of g_1. Two errors could have lead to the error syndrome $\langle g_1\rangle = -1$ and $\langle g_2\rangle = 1$: $\{X_1, X_2X_3\}$. The stabilizer formalism allows one to find this set simply by analysing possible errors which anti-commutes with g_1 and commutes with g_2. The most likely error to have happened is the single qubit error X_1, which can be recovered by applying a recovery gate $X_1^\dagger = X_1$ to the system.

In general a stabilizer code defined by stabilizers $\mathcal{S}$ can correct any error E_j from the set $\mathcal{E}$ if [39]

$$\forall E_j, E_k \in \mathcal{E}; \quad \exists S \in \mathcal{S}; E_j^\dagger E_k S E_k^\dagger E_j \notin \mathcal{S} \text{ or } E_j^\dagger E_k \in \mathcal{S}. \tag{2.15}$$

One needs to consider two error operations $E_j^\dagger$ and E_k as the recovery gate found from the error syndrome is itself an error. Effectively the code needs to be able to detect two errors simultaneously to allow error correction of a single error. Detect that an error happened and detect which recovery gate will remove the error.

We have described how a single bit-flip error can be detected and corrected by the repetition code. However, a bit-flip error is just one of an infinite number of errors that can happen to a qubit. An error can be a very small rotation of the qubit or a complete entanglement with an uncontrolled part of the environment. It is not trivial that error correction of a quantum state is even possible - how does one measure which error happened from a continuous set of errors? Quantum error correction is made possible by the fact that a superposition state collapses into just one state when measured effectively reducing the set of possible errors from infinite to finite.

[4]This intuitively makes sense as each generator g_i confines the state $|\psi\rangle$ to the part of the Hilbert space which has $g_i|\psi\rangle = |\psi\rangle$ - thereby excluding the other half with $g_i|\psi\rangle = -|\psi\rangle$.

g_1	Z_1Z_2
g_2	Z_2Z_3
g_3	Z_4Z_5
g_4	Z_5Z_6
g_5	Z_7Z_8
g_6	Z_8Z_9
g_7	$X_1X_2X_3X_4X_5X_6$
g_8	$X_4X_5X_6X_7X_8X_9$

Table 2.1: Stabilizers defining the Shor code which is formed from four repetition codes.

Any single qubit error E can be expanded into a linear combination of Pauli errors

$$E = e_I I + e_X X + e_Y Y + e_Z Z, \tag{2.16}$$

where e_i is the probability for error i happening on the qubit. The qubit state after an error is $E|\psi\rangle = e_I|\psi\rangle + e_X X|\psi\rangle + e_Y Y|\psi\rangle + e_Z Z|\psi\rangle$. Error detection of the Pauli errors X, Y, Z will detect the error syndrome which will collapse the superposition into just one of the four options. That is a quantum error correcting code being able to correct Pauli errors can correct *any* single qubit error as the error is discreetized by the detection.

Returning to the quantum repetition code defined by generators $\{Z_1Z_2, Z_2Z_3\}$ which can correct bit flip errors of the type $\{X_1, X_2, X_3\}$. To allow the repetition code to correct for any single qubit error one has to expand it to also detect errors Z_i (it is enough to correct for X_i and Z_i as $Y_i = X_iZ_i$). This code is known as the Shor code from the inventor Peter Shor [45]. First one realizes from symmetry that a repetition code with generators $\{X_1X_2, X_2X_3\}$ can correct the error set Z_1, Z_2, Z_3 - also called phase-flip errors. To correct for both X and Z errors the repetition code is concatenated. Three bit-flip repetition codes each able to correct bit-flip errors is used as single qubits in a phase-flip repetition code. In total nine qubits are combined with four repetition codes defined by eight stabilizers shown in Table 2.1. The first six stabilizers defines the three separate bit-flip repetition codes. The last two combines these three codes using the logical operators of each in the stabilizers. It is easily shown that any two single qubit errors E_jE_k either anticommutes with at least one stabilizer or is itself a stabilizer fulfilling Equation (2.15). E.g. Y_2Z_3 anticommutes with the stabilizer $g_1 = Z_1Z_2$.

The extension of the repetition code to the Shor code exemplifies the power of the stabilizer formalism. The quantum states of the codewords are given by:

$$\begin{aligned} |\bar{0}\rangle &= \frac{(|000\rangle + |111\rangle)(|000\rangle + |111\rangle)(|000\rangle + |111\rangle)}{2\sqrt{2}} \\ |\bar{1}\rangle &= \frac{(|000\rangle - |111\rangle)(|000\rangle - |111\rangle)(|000\rangle - |111\rangle)}{2\sqrt{2}} \end{aligned} \tag{2.17}$$

The codewords are superposition of eight states in the computational basis. Stabilizers allows us to define the full code from just eight stabilizers while the codewords are large superposition states.

The Shor code can be expanded to detect larger and larger error sets by increasing the

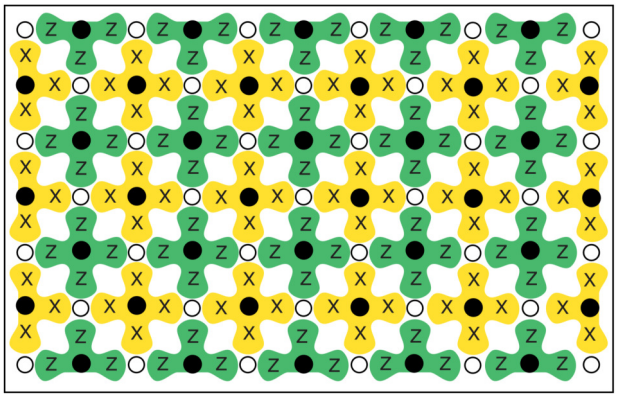

Figure 2.5: A 4x6 qubit surface code shown with qubits shown as open circles. Local stabilizers are shown in green and yellow. Figure adapted from [46].

number of qubits. However, other codes have shown better performance for scalability. The most exciting codes currently being investigated both theoretically and experimentally are topological codes. These are codes that are defined by *local* stabilizers with *global* logical operators. One such example is the surface code [26] shown in Figure 2.5. Qubits are shown as open circles while four-body stabilizers are shown in green and yellow for $Z_{i,1}Z_{i,2}Z_{i,3}Z_{i,4}$ and $X_{i,1}X_{i,2}X_{i,3}X_{i,4}$ respectively. The quantum information is encoded as a global degree of freedom while the stabilizers are local. Any local error (a row of errors not extending half-way across the code) can be detected. It follows that by making the code larger it can correct for larger errors.

The surface code has received a great deal of experimental attention due to the low error-threshold and relatively simple implementation [46]. Only nearest neighbour couplings of qubits and Clifford gates are necessary to fully implement a patch of surface code. The threshold is the maximum error rate at which making the code larger will extend the lifetime of the encoded qubit. Estimating thresholds is very depended on assumptions about the physical implementation, the error model, and the syndrome decoder. A code can be implemented in any qubit system, however the implementation of stabilizer measurements can vary drastically from system to system. Naturally this also effects the error rates of stabilizer measurement which effects the error threshold. Syndrome decoding is an interesting and complicated topic on its own. To correct for errors, syndrome decoding collects all the local stabilizer measurements in classical logic and performs a global computation of the most likely set of errors. Adding that the stabilizer measurements themselves can be faulty one has to do several stabilizer measurements, in between which new errors can happen. It turns out the problem of optimal syndrome decoding becomes an intractable problem which a classical computer cannot efficiently solve [47]! Fortunately, new algorithms achieving suffcient (although not optimal) performance has been developed so that we don't need a quantum computer to be able to error correct a quantum computer [48].

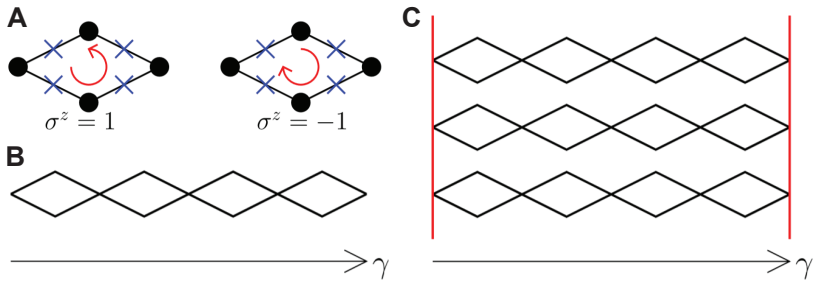

Figure 2.6: . **A** Rhombus structure with two degenerate ground states denoted $\sigma_z = \pm 1$. **B** A row of rhombi with a total phase γ. **C** Multiple rows are coupled to form a protected qubit. Figure adapted from [29].

2.3 Passive Error Correction

In the previous section we introduced stabilizer codes. These codes relies on measurements of error syndromes to detect, decode, and correct the errors. This potentially adds a huge overhead in control electronics and computation time. An alternative path is to implement passive quantum error correction [29]. The basic idea is to form physical system that effectively separates stabilizer eigenstates in energy. A Hamiltonian implementing the Shor code is given by

$$\widehat{H} = -\frac{\Delta}{2} \sum_{S_i \in \mathcal{S}} S_i, \tag{2.18}$$

where $\mathcal{S}$ is the group of stabilizers with generators given in Table 2.1. In this Hamiltonian the effective ground state is doubly degenerate separated by an energy gap Δ from all other eigenstates of the system.

To build such a system the first step is to build energy degenerate qubits which are then coupled by specific terms as described by the Hamiltonian. These qubits need to be defined by degenerate two-level systems as any energy difference between the qubit states will modify the Hamiltonian. B. Douçot and L. B. Ioffe describe in [29] a possible system for protected qubits based on passive quantum error correction. The basic building block in the system is a superconducting rhombus structure in which the degenerate ground states are given by a superconducting phase difference across the circuit of $\pm\frac{\pi}{2}$ [Figure 2.6**A**]. We can describe these two states with Pauli operators where the states $\left|\pm\frac{\pi}{2}\right\rangle$ are eigenstates of σ_z.

To form a Hamiltonian as above the one first places a several qubits in an array as shown in Figure 2.6**B**. The total phase across the array will be $\gamma = \frac{\pi}{2} \prod_j \sigma_{z,j}$ for an odd number of rhombi and $\gamma = \frac{\pi}{2} \left(\prod_j \sigma_{z,j} + 1 \right)$ for an even number. In Figure 2.6**C** multiple arrays are connected enforcing an common phase across the arrays. Due to the common phase there is a high energy cost associated to a single qubit switching σ_z eigenvalue. However, if two qubits switch it will not affect $\prod_i \sigma_{z,j}$. Adding a coupling term between qubits, for superconducting qubits the coupling is achieved by a small charging energy,

in the same array the effective Hamiltonian is given by [29]

$$\widehat{H} = -\frac{\Delta_z}{2}\sum_{i,i'}\prod_{j}\sigma_{z,ij}\prod_{j}\sigma_{z,i'j} - \frac{\Delta_x}{2}\sum_{i}\sum_{j,j'}\sigma_{x,ij}\sigma_{x,ij'}, \tag{2.19}$$

where i refers to each row and j refers to the index within each row. This Hamiltonian describes a qubit system which passively implements the Shor code (X and Z terms are reversed compared to the stabilizers in 2.1). While this example focused on the implementation of the Shor code one can also design a system that implements the surface code [29].

Passive error correction has the advantage that no costly syndrome analysis has to be performed as errors effectively are gapped out by the system. Reducing the amount of classical control needed for error correction frees up encoded qubit to compute actual quantum algorithms. While the error correction is implemented by connecting many degenerate qubits it is still possible to probe a single qubit, or rhombus [36], at a time to gain information of the basic building blocks of the code. When the single qubit behaves as expected several can be connected to add error correction to the system. The difficulty lies in the fact that an inherently protected qubit is increasingly difficult to measure and control.

2.4 Topological Material

The goal of error correction, both passive and active, is to remove errors from a non-perfect system. What if instead nature provided a topological material with degenerate, non-local ground states protected from errors by an energy gap? This idea was proposed by A. Kitaev in [30] as an alternative path to a high-fidelity quantum computer. The model proposed, known as the Kitaev chain, is a one-dimensional chain of electrons at sites i described by the Hamiltonian

$$H = -\mu\sum_{i}\hat{c}_i^\dagger\hat{c}_i - \frac{t}{2}\sum_{i}\left(\hat{c}_i^\dagger\hat{c}_{i+1} + \hat{c}_{i+1}^\dagger\hat{c}_i\right) - \frac{\Delta}{2}\sum_{i}\left(e^{i\phi}\hat{c}_i\hat{c}_{i+1} + e^{-i\phi}\hat{c}_{i+1}^\dagger\hat{c}_i^\dagger\right), \tag{2.20}$$

where $\hat{c}^\dagger$ and $\hat{c}$ are fermion creation and annihilation operators respectively, μ is the chemical potential, t is the nearest-neighbor hopping term, and Δ is a superconducting electron-electron coupling term with phase ϕ. A detailed review of the properties of this Hamiltonian is given in [49]. Here we will focus on two specific cases: a trivial case with $\mu < 0$ and $\Delta = t = 0$ and a topological regime with $\mu = 0$ and $\Delta = t \neq 0$.

To understand the physics of the two regimes it is beneficial to rewrite the Hamiltonian using Majorana fermion operators. A Majorana fermion is a particle which is its own anti-particle and follows fermion anticommutation relations.

$$\begin{aligned} \hat{\gamma}_\alpha &= \hat{\gamma}_\alpha^\dagger, \\ \{\hat{\gamma}_\alpha, \hat{\gamma}_\beta\} &= 2\delta_{\alpha\beta}. \end{aligned} \tag{2.21}$$

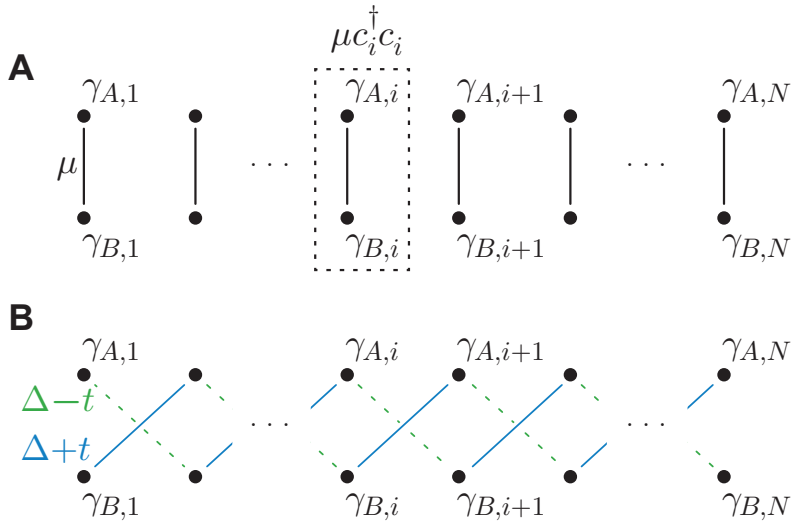

Figure 2.7: **A** The Kitaev chain represented in the Majorana basis. Each black circle is a Majorana fermion with two at each site making up a single electron as indicated by the dashed box. Black lines depict chemical potential μ as an on-site Majorana coupling. **B** Inter-site Majorana coupling in the Kitaev chain with strength $\Delta + t$ and $\Delta - t$ respectively. For $\Delta = t$ Majorana fermions $\hat{\gamma}_{A,1}$ and $\hat{\gamma}_{B,N}$ are uncoupled from the chain forming a single, non-local degree of freedom described by $\hat{c}_M = \frac{1}{2}(\hat{\gamma}_{A,1} + i\hat{\gamma}_{B,N})$.

A single electron can be decomposed into two Majorana fermions.

$$\begin{aligned} \hat{c}_i &= \frac{e^{-i\theta}}{2}(\hat{\gamma}_{B,i} + i\hat{\gamma}_{A,i}), \\ \hat{c}_i^\dagger &= \frac{e^{i\theta}}{2}(\hat{\gamma}_{B,i} - i\hat{\gamma}_{A,i}). \end{aligned} \tag{2.22}$$

where θ is a global phase. Setting $\theta = \phi/2$ Equation (2.20) can be written as

$$H = -\frac{\mu}{2}\sum_i (1 + i\hat{\gamma}_{B,i}\hat{\gamma}_{A,i}) - \frac{t+\Delta}{4}\sum_i i\hat{\gamma}_{B,i}\hat{\gamma}_{A,i+1} - \frac{\Delta - t}{4}\sum_i i\hat{\gamma}_{A,i}\hat{\gamma}_{B,i+1}, \tag{2.23}$$

where $\mathcal{P}_i = i\gamma_{B,i}\gamma_{A,i} = \pm 1$ is the parity of the fermion at site i defined as -1 for vacuum and $+1$ for filled fermion. In the regime of $\mu < 0$ and $\Delta = t = 0$ the latter two terms disappear leaving a fermion counting term as shown in Figure 2.7**A**. The Hamiltonian has a single ground state given by vacuum. Any excitation is gapped by an energy cost μ for introducing a fermion in the system.

Setting the $\mu = 0$ we can understand the last two terms of the Hamiltonian as inter-site Majorana couplings depicted in green and blue in Figure 2.7**B**. In the case of $\Delta = t$ only one inter-site coupling is non-zero. Coupled Majorana fermions $\hat{\gamma}_{B,i}$ and $\hat{\gamma}_{A,i+1}$ form electron degrees of freedom with an energy $\Delta + t$ for each filled electron state. The bulk of the Kitaev chain is again described by a vacuum ground state now with energy gap $\Delta + t$. However, this leaves a single, uncoupled Majorana fermion at each end of the chain. These can be described by a non-local electron with $\hat{c}_M = \frac{1}{2}(\hat{\gamma}_{A,1} + i\hat{\gamma}_{B,N})$. As $\hat{c}_M^\dagger \hat{c}_M$ is not present in the Hamiltonian they form a zero-energy two-level system which

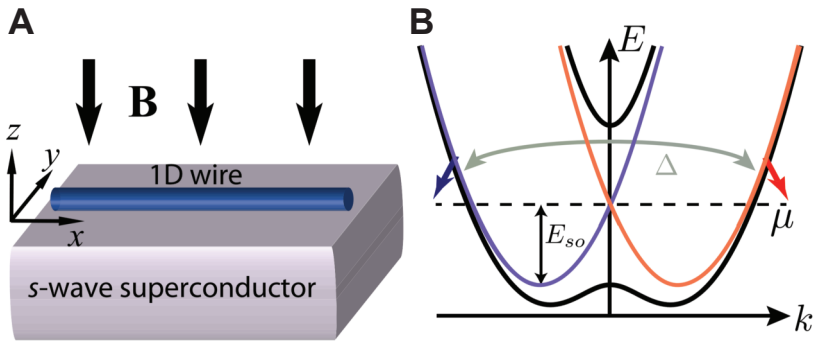

Figure 2.8: **A** Schematic of a 1-dimensional nanowire coupled to a superconductor and placed in a magnetic field. **B** A spin-orbit coupling displaces the spin parabolas in k-space indicated by blue and red parabolaes. An additional Zeeman splitting due to a magnetic field opens a gap as shown in balck bands. Placing the chemical potential in the gap forms an effective spin-less system. Figure adapted from [49].

is protected from the noise due to its non-local nature. The appearance of uncoupled Majorana states at each end originates from a change in the topology of the material. This enforces a stability of the states to small changes of the parameters μ, t, and Δ. It is not only the single point $\mu = 0$ and $\Delta = t \neq 0$ in phase space that is topological but a surrounding domain [49].

If such states can be created and controlled in nature one can take advantage of the inherent protection afforded by the topological material. One challenge for an experimental realization is that the Kitaev chain is spin-less. If formed by an electron system with Kramer's degeneracy there will be two Majorana states at each end - one for each spin flavor. Any spin-orbit interaction will couple these states forming local electron states breaking the protection. Luthyn et al. and Oreg. et al. proposed in 2010 [50, 51] a solution to this problem based on a one-dimensional nanowire with spin-orbit coupling, placed in a magnetic field, and strongly coupled to superconductor as shown in Figure 2.8**A**. The Kramer's degeneracy is lifted due to the combination of spin-orbit coupling and Zeeman splitting while the superconductivity provides the electron-electron coupling present in the Kitaev chain. Spin-orbit coupling can be understood in momentum space of the electron bands in the nanowire as a separation of spin-bands shown in red and blue in Figure 2.8**B**. To freeze the spin-degree of freedom at the fermi surface a magnetic field is added to open a gap between the two parabolas at $k = 0$. With the chemical potential placed in the gap only one electron band is present at the fermi surface effectively forming a spin-less system.

Topological materials with non-local, protected degrees of freedom offer a unique path to high-fidelity qubits. The challenge lies in creating the topological material, and maybe even more challenging, do it in such a way that the protected qubit can be both controlled and measured.

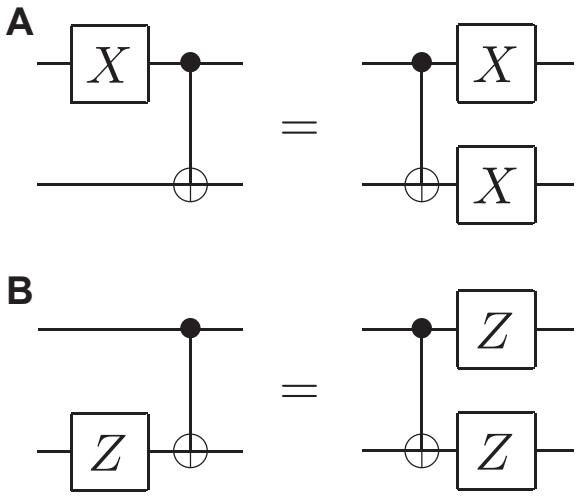

Figure 2.9: **A-B** Certain single qubit errors before a CNOT gate are equivalent to two single-qubit errors happening after the CNOT gate.

2.5 Fault-Tolerant Quantum Computing

The previous sections described three different paths to protected qubits based on encoding qubits in non-local degrees of freedom. However, this alone will only form quantum memory while a quantum computer needs to perform computations. Here we will briefly touch on the subject of fault-Tolerant quantum computing to put in perspective the challenges still ahead of us[5].

First focusing on a protected qubit with quantum error correction. Assume that a single qubit error happens before a CNOT gate as in Figure 2.9. For certain errors a single qubit error before the two-qubit gate is equivalent to having two qubit errors after it. The single error got multiplied by the operation posing a huge problem for error correction. If qubit operations are performed thoughtlessly a single qubit error can potentially spread throughout the code corrupting the protected information. Any control, including syndrome measurements, has to be implemented in fault-tolerant manner i.e. any error before an operation should remain correctable after the operation. This effectively limits the possible operations that can be performed on an encoded qubit to a finite set dependent on the specific code. The same limitations hold for fault-tolerant gate sets in topological materials and with passive error correction.

In all cases of topological quantum computers actively being pursued the set of possible gates is either the Clifford group or a subset thereof. However, the Clifford gate set is not a universal and is therefore not enough to build a universal quantum computer. In fact such a limited quantum computer has been proven to be no better than a classical computer. The solution is to add one more allowed gate to the quantum computer - the gate $T = R_Z(\frac{\pi}{4})$ plus the Clifford group is sufficient for universal quantum computing[6].

[5] In most cases theoretical solutions have been found but whether they are experimentally practical on an encoded qubit remains to be seen.

[6] The set of Clifford gates and the T-gate cannot strictly perform all gates. Rather it is a dense

How then to perform fault-tolerant T-gates? One way is to perform magic state distillation of T-gates [52, 53]. Magic state distillation is an algorithm which produces high fidelity $T|0\rangle$ states from a many noisy $T|0\rangle$ states. With this a non-fault-tolerant version of a T-gate is sufficient for quantum computing. The downside is that some estimates indicated that a quantum computer will have an enormous overhead just creating T-gates [54]. There are alternative approaches such as guage fixing and code deformation [55, 56] but these have their own difficulties.

gate-set which can perform gates arbitrarily close to any gate - analogous to a rational number being arbitrarily close to any real number.

Chapter 3

Circuit Quantum Electrodynamics

Electrical currents in condensed matter are carried by electrons each following the laws of quantum mechanics. The strong coulomb force ensures a smooth density of electrons without fluctuations throughout the material[1]. Remarkably, this allows us to describe a current not as an enormous number of individual electrons but as an ensemble of electrons with only a few degrees of freedom. In superconductors we can further ignore low-energy single-particle excitation as these excitations are gapped. The only low-energy excitations left are divergenceless excitations in the ensemble density with charge build-up at boundaries of the material (capacitors). At low temperatures the low-energy degrees of freedom in the ensemble of electrons behaves quantum mechanically with a quantized energy spectrum. As we will see superconducting circuits can form ensemble modes behaving like artificial atoms or harmonic oscillators. Circuit quantum electrodynamics (cQED) is the quantum mechanical description of such coupled atom and oscillator modes analogous to light-matter interactions in cavity quantum electrodynamics, where an atom is coupled to light in a cavity.

This chapter will introduce the ideas of quanticed electrical circuits, cQED [57] and superconducting qubits loosely following notes by Steven M. Girvin [58]. First section describes a quantized Harmonic oscillator both as a lumped element resonator and a distributed circuit. Second section introduces the ideas of Josephson junctions and artificial atoms both with traditional aluminium tunnel junctions and hybrid semiconductor-superconductor junctions. Following the introduction of artificial atoms the third section describes the interaction of artificial atoms in the resonant and dispersive regimes as well as introducing qubit readout. Last sections describes qubit control for single-qubit gates and two-qubit coupling and gates for quantum computing algorithms.

[1] Assuming no excitations at frequencies above the plasma frequency of the material. Above this frequency excitations can form waves in the electron density.

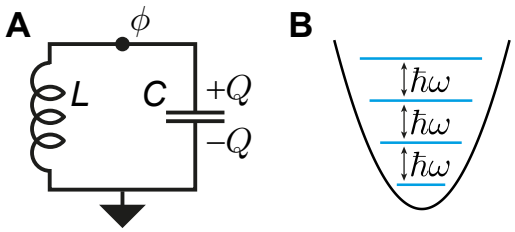

Figure 3.1: **A** An LC resonant circuit. **B** The energy spectrum of the quantized harmonic oscillator.

3.1 Quantized Harmonic Oscillators

The simplest harmonic oscillator in an electrical circuit is the LC oscillator in Figure 3.1**A**. To find the equations of motion of the circuit we first define the node flux at point ϕ as our coordinate[2]. A node is a connecting branch between two or more lumped elements [59]. Each node has a node flux defined as

$$\phi(t) = \int^t V(t')dt', \tag{3.1}$$

$$\dot{\phi}(t) = V(t), \tag{3.2}$$

where $V(t)$ is the voltage at the node. In Figure 3.1**A** there are two nodes: the upper node defined as ϕ and the bottom node defined as ground which by definition has node flux $\phi_{\text{Ground}} = \int^t V_{\text{Ground}}(t')dt' = 0$.

The voltage across the inductor can be related to the node flux as

$$\dot{\phi}(t) - \dot{\phi}_{\text{Ground}}(t) = \dot{\phi}(t) = V(t) = L\dot{I}(t). \tag{3.3}$$

By integration we can identify $\phi = LI$ as the magnetic flux stored in the inductor. The energy of the inductor $E_L = LI^2/2 = \phi^2/2L$ in coordinates of ϕ looks like a potential energy. Similarly the energy of the capacitor as a function of ϕ is $E_C = CV^2/2 = C\dot{\phi}^2/2$ looks like a kinetic energy. With the potential and kinetic energy of the system we can write the Lagrangian of the system with the node flux ϕ as the coordinate:

$$\mathcal{L} = \frac{C}{2}\dot{\phi}^2 - \frac{1}{2L}\phi^2. \tag{3.4}$$

From the Lagrangian we identify the conjugate momentum of the node flux $Q = d\mathcal{L}/d\dot{\phi} = C\dot{\phi} = CV$ as the charge stored on the capacitor. The Hamiltonian of the system can be found from the Lagrangian with a Legendre transformation

$$H = Q\dot{\phi} - \mathcal{L} = \frac{1}{2C}Q^2 + \frac{1}{2L}\phi^2. \tag{3.5}$$

We recognise the Hamiltonian as that of a harmonic oscillator formed by a particle on

[2]The LC circuit is more commonly solved with the charge of the capacitor as the coordinate. However, when working with Josephson junctions the node flux is a more convenient choice of coordinate.

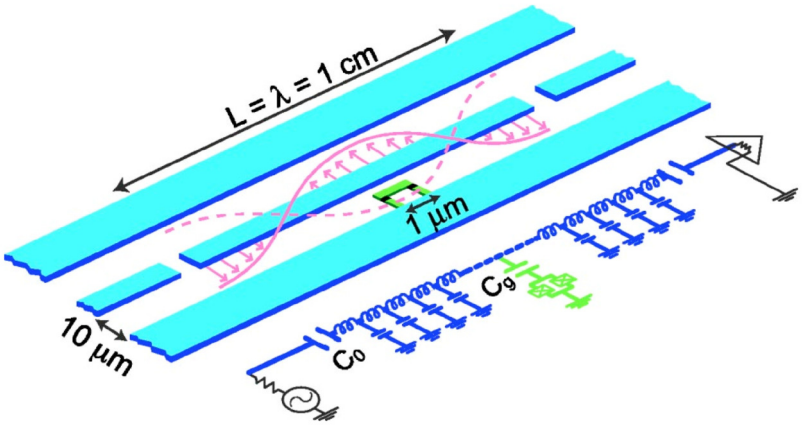

Figure 3.2: A distributed microwave cavity. Figure adapted from [57].

a spring, where the particle has coordinate $\phi(t)$, momentum $Q(t)$, and mass C and the spring has spring constant $1/L$. With this in mind the resonance frequency of the harmonic oscillator is readily found as $\omega = 1/\sqrt{LC}$.

The LC circuit is quantized by promoting the coordinate and its conjugate momentum to quantum operators obeying the canonical commutation relation

$$[\hat{\phi}, \widehat{Q}] = i\hbar. \tag{3.6}$$

The Hamiltonian of the harmonic oscillator can as usual be rewritten with raising and lowering operators

$$\widehat{H} = \frac{1}{2C}\widehat{Q}^2 + \frac{1}{2L}\hat{\phi}^2 = \hbar\omega\left(\hat{a}^\dagger\hat{a} + \frac{1}{2}\right), \tag{3.7}$$

where the raising and lowering operators $\hat{a}^\dagger$ and $\hat{a}$ are given by

$$\begin{aligned} \hat{a} &= \frac{1}{\sqrt{2L\hbar\omega}}\hat{\phi} + i\frac{1}{\sqrt{2C\hbar\omega}}\widehat{Q}, \\ \hat{a}^\dagger &= \frac{1}{\sqrt{2L\hbar\omega}}\hat{\phi} - i\frac{1}{\sqrt{2C\hbar\omega}}\widehat{Q}. \end{aligned} \tag{3.8}$$

The energy spectrum of the harmonic oscillator is shown in Figure 3.1**B** with the well known equidistant energy levels. An eigenstate $|n\rangle$ of the quantized LC circuit is commonly referred to as a photon number state with n photons, where n is the eigenvalue of the number operator $\hat{n} = \hat{a}^\dagger\hat{a}$. The name originates from light cavities, which are harmonic oscillators whose eigenstates are given by the number of light photons.

Harmonic oscillators formed by lumped element components are instructive to solve to introduce the theory of cQED. However, in practice harmonic oscillators, also commonly referred to as resonators, are often (and exclusively in the work presented in this thesis) formed in distributed elements such as coplanar waveguides (CPWs) shown in Figure 3.2. Distributed CPWs can be modelled as a circuit with inductance l and capacitance c per

unit length with a continuous, spatially dependent node flux, $\hat{\phi}(x,t)$. Microwave cavities are created by introducing boundary conditions such as breaks or shorts of the center conductor in a length of CPW. We will not go through a full derivation of the modes of a distributed cavity, which can be found in [58], and instead focus on the results. The system can be modelled as a sum of non-interacting harmonic oscillators

$$\widehat{H} = \sum_n \left(\hbar\omega_n a_n^\dagger a_n + \frac{1}{2} \right), \tag{3.9}$$

where ω_n are resonance frequencies described by standing-wave solutions in the spatial degree of freedom of the node flux. For a CPW with wave velocity $v_\mathrm{p} = 1/\sqrt{lc}$ and wavelength of standing waves λ_n the frequencies are given by $\omega_n = v_\mathrm{p}/\lambda_n$. The wavelengths, $lambda_n$, of a cavity depends on boundary conditions of the system. A break in the center conductor as in Figure 3.2 forms a current node (no current can run out of the conductor) and correspondingly a voltage anti-node. Two breaks separated by a length L creates standing waves with wavelength $\lambda_n = 2L/n$ with $n \geq 1$ each describing a harmonic oscillator mode with resonance frequency $\omega_n = nv_\mathrm{p}/2L$. The voltage oscillation of mode $n = 2$ is depicted in pink in Figure 3.2. Such a cavity is known as a $\lambda/2$ cavity as its length is half of the wavelength of the lowest mode. If one side instead has a short from center conductor to ground one forms a voltage node as a boundary condition on this side. This cavity will have standing waves with wavelength $\lambda_n = 4L/(2n+1)$ with $n \geq 0$ and is correspondingly named a $\lambda/4$ cavity as $\lambda_0/4 = L$.

As the resonance frequency of the second-lowest harmonic mode of a distributed cavity is two or three times larger than the lowest mode, one can in most cases model it as a single harmonic oscillator described by the lowest frequency mode. For the remainder of this thesis we will treat distributed cavities as a single harmonic oscillator.

3.2 Artificial Atoms in Superconducting Circuits

As we ultimately are looking to create qubits in superconducting circuits we need a way to isolate a single two-level system. The energy spectrum of a harmonic oscillator is described by equidistant, non-degenerate energy levels with a single resonance frequency making it impossible to energetically isolate two eigenstates as a qubit. In contrast the spectrum of an atom is uneven and can have degenerate levels that can readily be utilized as qubits in ion traps. Superconducting artificial atoms are circuits that similarly have uneven energy spectra allowing a qubit subspace to be energetically separated from the rest of the Hilbert space. An uneven energy spectrum is achieved by adding a non-linear element to the circuit[3].

In superconducting circuits the non-linearity is found as the Josephson effect, which was theoretically predicted by B. D. Josephson in 1962 [62]. Superconductivity originates from an electron-electron interaction that causes electrons to pair up as bosonic Cooper pairs which condense into a boson condensate described by a single wave function ψ

[3]It is possible use cavities as qubits by instead implementing nonlinearity in the control circuit [60, 61]. Recent results have shown active error correction in such systems [16].

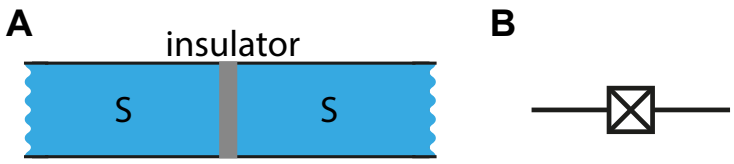

Figure 3.3: **A** Two superconducting electrodes (blue) sandwiching an insulator (grey) forms a Josephson junction. **B** The circuit symbol of a Josephson junction.

[63]. The magnitude of the wavefunction $|\psi|^2$ is equal to the density of Cooper pairs in the superconductor while its phase only manifests itself when coupling two superconductors. Josephson considered the case of a superconductor-insulator-superconductor (SIS) junction as shown in Figure 3.3. The Cooper pairs in each superconducting electrode can tunnel through the thin insulator allowing a current to flow. Josephson made two predictions for such a weak link Josephson junction[4]

$$I_s = I_c \sin\varphi, \tag{3.10}$$

$$\frac{d\varphi}{dt} = \frac{2eV}{\hbar}, \tag{3.11}$$

where I_s is a dissipationless supercurrent tunnelling through the insulator and φ is the phase difference between the two wavefunctions describing each superconductor. Equation (3.10) is the current-phase relation that describes the dissipationless current flowing across a junction as a function of phase difference φ. The parameter I_c is the critical current of the Josephson junction given by the maximal dissipationless current that can flow across the junction above which the junction will turn resistive. The energy stored in a Josephson junction as a function of φ is readily calculated by combining the two equations (3.10, 3.11):

$$\begin{aligned} E(\varphi) &= \int I_s V(t) dt \\ &= \frac{\hbar I_c}{2e} \int \sin(\varphi) d\varphi \\ &= -E_J \cos\varphi, \end{aligned} \tag{3.12}$$

where $E_J = \hbar I_c / 2e$ is the Josephson energy.

Equation (3.11) is very similar to the definition of node flux ϕ given in equation (3.1) leading one to similarly consider φ as a position coordinate. With φ as a coordinate the energy of (3.12) looks like a potential energy similar to that of an inductor. Importantly the potential energy of a Josephson junction is non-linear. A difference between ϕ and φ not visible in the equations is that φ is a periodic coordinate on the range $[-\pi, \pi]$ while ϕ can take any real value. However, in the special case where the wavefunctions of the circuit vanishes at $\varphi = \pm\pi$ we find that $\phi \approx \frac{\hbar}{2e}\varphi = \frac{\Phi_0}{2\pi}\varphi$, where $\Phi_0 = h/2e$ is the superconducting flux quantum.

Although the potential energy of a Josephson junction resembles that of an inductor

[4]Weak link means that each Cooper pair has a low probability for tunnelling through the insulator.

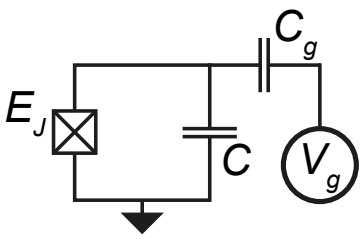

Figure 3.4: A Josephson junction in parallel with a capacitor and a voltage source coupled capacitively to the circuit.

the current flow is radically different. The current across a junction is carried by single Cooper pairs tunnelling across the junction. Consequently a capacitor plate coupled only through Josephson junctions will have a discreet charge given by an integer number of Cooper pairs. The energy states of the system can be described by charge states $|n\rangle$, where n is the number of Cooper pairs on the capacitor (not to be confused with photon number states introduced in the previous section). A circuit of a Josephson junction in parallel with a capacitor and a nearby voltage source V_g is shown in Figure 3.4. Identifying the energy of the capacitor as the kinetic energy and the potential energy given by the Josephson junction we can write down the Hamiltonian of the system

$$\widehat{H} = 4E_C(\hat{n} - n_g)^2 - E_J \cos\hat{\varphi}, \tag{3.13}$$

where $E_C = e^2/2(C + C_g)$ is the charging energy of the island, $\hat{n}$ is the number operator for the number of Cooper pairs on the island, and $n_g = -C_g V_g/2e$ is a charge offset. This is known as the Cooper pair box Hamiltonian due to the upper part of the capacitor acting as a box with a discreet number of Cooper pairs. The voltage source V_g describes both the coupling of a controlled charge offset and an uncontrolled environment.

The Cooper pair box Hamiltonian can be simulated numerically in the charge basis with $\hat{n}|n\rangle = n|n\rangle$ and $\cos\hat{\varphi} = \sum(|n\rangle\langle n+1| + |n+1\rangle\langle n|)$ [58]. In Figure 3.5 the energy levels are plotted as a function of the offset charge for different values of E_J/E_C. Left panel shows $E_J = E_C$ which is known as the Cooper pair box regime. In this regime eigenstates are described by a single number of Copper pairs on the capacitor with energies given by parabolas defined by E_C as a function of offset charge n_g (blue dashed lines). The Josephson junction acts as a coupling term between charge states creating avoided crossings between parabola of charge states. The charge dispersion, the change of energy as a function of offset charge n_g, arises due to the discreetized charge flow through the Josephson junction. While the Cooper pair box can be used as a qubit [64–66] large charge dispersion is undesirable as any charge noise in the vicinity of the capacitor will induce decoherence.

J. Koch et al. proposed a charge-insensitive regime, the transmon regime, defined by $E_J/E_C \gg 1$ [67]. The charge dispersion of the energy levels flattens exponentially with $\sqrt{E_J/E_C}$ making them insensitive to n_g as shown in right panel of Figure 3.5. While the Hamiltonian is readily solved numerically it is beneficial to calculate an approximate solution analytically by approximating the Hamiltonian with that of an LC oscillator.

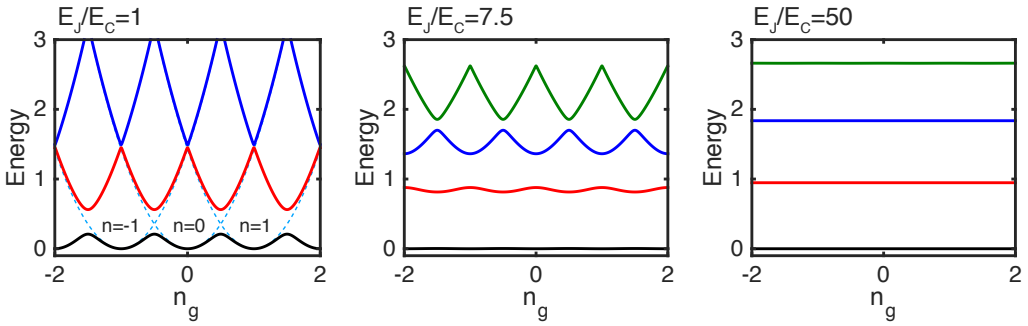

Figure 3.5: The lowest energy levels of the Cooper-pair-box Hamiltonian in Equation (3.13) for different values of E_J/E_C. The energy of the Hamiltonian with $E_J = 0$ is plotted as light blue dotted parabolas in left panel. In all figures the energy is normalized by $\sqrt{8E_C E_J}$.

We note that the node flux is proportional to the superconducting phase difference, $\phi = \frac{\Phi_0}{2\pi}\varphi$, and the discreet Cooper pair number n can be related to charge by $Q = 2en$. In coordinates of ϕ and Q the Hamiltonian can be written as (setting $n_g = 0$ for the moment)

$$\begin{aligned}\widehat{H} &\approx \frac{1}{2C}\widehat{Q}^2 - E_J \cos\left(2\pi\frac{\hat{\phi}}{\Phi_0}\right) \\ &\approx \frac{1}{2C}\widehat{Q}^2 + E_J\left(\frac{2\pi}{\Phi_0}\right)^2\frac{\hat{\phi}^2}{2} \\ &= \frac{1}{2C}\widehat{Q}^2 + \frac{1}{2L_J}\hat{\phi}^2 \end{aligned} \tag{3.14}$$

where we kept only the quadratic term of an Taylor expansion around $\phi = 0$ and $L_J = (\hbar/2e)^2/E_J$ is the inductance of the Josephson junction. The approximate Hamiltonian is that of a Harmonic LC circuit with resonance frequency $\omega = 1/\sqrt{CL_J} = \sqrt{8E_J E_C}/\hbar$.

The Taylor expansion around $\phi = 0$ is only valid if the quantum fluctuations of the solutions are consistent with the assumption $\phi \ll \pi$. The mean square amplitude of the zero point fluctuations is

$$\phi_{ZPF}^2 = \langle 0|\hat{\phi}^2|0\rangle = \left(\frac{\Phi_0}{2\pi}\right)^2\left(\frac{2E_C}{E_J}\right)^{1/2}, \tag{3.15}$$

where $|0\rangle$ refers to the ground state of the Harmonic oscillator with raising and lowering operators defined in (3.8). We find that in the transmon limit $E_J/E_C \gg 1$ the Taylor expansion is indeed valid. The same result validates the assumption $\phi = \frac{\Phi_0}{2\pi}\varphi$ as the periodicity of φ has no effect for $|\varphi| \ll \pi$.

To second order in the Taylor expansion the transmon acts as a harmonic oscillator. To show that the transmon is in fact an artificial atom with an uneven energy spectrum

the fourth order term of the Taylor expansion is added as a perturbation

$$\begin{aligned} \widehat{H} &\approx \widehat{H}_0 + \widehat{V}, \\ \widehat{V} &= -E_J \left(\frac{2\pi}{\Phi_0}\right)^4 \frac{\hat{\phi}^4}{24}, \end{aligned} \tag{3.16}$$

where $\widehat{H}_0$ is the harmonic Hamiltonian given in Equation (3.14). Using raising and lowering operators of $\widehat{H}_0$ given in Equation (3.8) we can write $\hat{\phi}^4 = (\Phi_0/2\pi)^4 (2E_C/E_J) \left(\hat{a} + \hat{a}^\dagger\right)^4$. Inserting into $\widehat{V}$ and dropping all terms with uneven numbers of raising and lowering operators (first order perturbation theory) the perturbation can be written as

$$\widehat{V} = -\frac{1}{12} E_C \left(\hat{a}^\dagger + \hat{a}\right)^4 \approx -\frac{E_C}{2} \left(\hat{a}^\dagger \hat{a}^\dagger \hat{a}\hat{a} + 2\hat{a}^\dagger \hat{a}\right). \tag{3.17}$$

In first order perturbation theory this leads to a correction of the energy of state $|1\rangle$ so that $E_1 - E_0 = E_{10} = \sqrt{8E_J E_C} - E_C$. For the second excited state $|2\rangle$ the correction is $-3E_C$ leading to an energy difference between first and second excited states given by $E_{12} = \sqrt{8E_J E_C} - 2E_C$. These energy corrections originates from the non-linearity of the cosine potential of a Josephson junction. The amount of non-linearity is quantified by the anharmonicity α defined by

$$\alpha = E_{21} - E_{10} \approx -E_C. \tag{3.18}$$

Remarkably, even the simplest circuit with a Josephson junction leads to artificial atoms with distinct energy spectra depending on the ratio of E_J/E_C. Experimentally, the transmon limit turned out to have longer coherence times due to the supression of charge noise [68]. However, this comes at the cost of lower anharmonicity, which limits the speed of operations [69], but with optimization of room temperature control equipment [70, 71] this is a much easier problem to work with than inherent charge noise.

3.3 Semiconductor Based Josephson Junctions

Above we described an artificial atom made of a single Josephson junction in the weak coupling regime. Such Josephson junctions are commonly realized by an $Al/Al_2O_3/Al$ sandwich with an aluminum oxide thickness of a few nanometers. When fabricated it has fixed characteristics allowing no direct control of the Josephson energy. To gain control of the effective Josephson energy one can place two junctions in parallel to form a SQUID, which has an effective Josephson energy tunable by a magnetic flux. A different approach has become possible as developments in semiconductor growth technology have produced new materials bringing field effect tunability of semiconductors into superconducting circuits [31, 72].

A schematic of a superconductor-semiconductor-superconductor (SSmS) Josephson junction is shown in Figure 3.6. The carrier density of the semiconductor is tunable using a nearby gate which in turn tunes the critical current of the junction. By exchanging the SIS Josephson junction in the transmon circuit with an SSmS junction the transmon

Figure 3.6: **A** Two superconducting electrodes (blue) sandwiching a semiconductor (green) form a Josephson junction. The semiconductor is tuned by a nearby gate electrode making the Josephson junction gate tunable. **B** Circuit symbol of a gate tunable Josephson junction.

becomes gate tunable [73–77]. The energy of the gate-tunable transmon ("gatemon") is tuned through the critical current $E_{01}(V_G) \propto \sqrt{E_J(V_G)} \propto \sqrt{I_c(V_G)}$.

Experiments have shown that it is possible to make high quality semiconductor nanowire proximitised by a superconductor [31, 78]. P. Krogstrup et al. have grown superconducting nanowires with a semiconducting InAs core and an epitaxial aluminum shell, see Figure 3.7**A**. The perfect crystalline interface between the semiconductor and superconductor makes these nanowires ideal for development of semiconductor based superconducting qubits.[5] A weak link in the superconducting nanowire is created by chemically etching a small segment of the aluminium shell as shown in Figure 3.7**A**. The exposed semiconducting InAs core allows electric fields from a nearby gate electrode with voltage V_G to tune the conductance of the core which influences the critical current of the junction. Experimental measurements in Figure 3.7**B** reveal that the critical current is indeed gate tunable. The critical current is measured as the highest dissipationless current trough the junction. The electron mean free path of InAs nanowires has been found to be l = 100-150 nm [78, 79]. As the junction length is longer than the mean free path, mesoscopic conductance fluctuations due to scattering across the junction show up as a non-monotonic critical current as a function of gate voltage.

A gate-tunable superconducting artificial atom formed by a nanowire Josephson junction will have different characteristics than that of a conventional transmon [80]. Nanowire based Josephson junctions have a few highly transmitting channels while the current-phase relation in Equation (3.10) describes the case of many low-transmitting channels. It can be shown theoretically that the potential energy of a ballistic junction with coherence length much longer than the junction width is given by [81]:

$$E = -\Delta \sum_i \sqrt{1 - \tau_i \sin^2(\varphi/2)}, \tag{3.19}$$

where τ_i is the transmission of the i'th channel and Δ is the superconducting gap. The effective coherence length in an InAs nanowire Josephson junction can be estimated from the superconducting coherence length $\xi_0 \sim 1100$ nm [80] and the mean free path in InAs as $\xi = \sqrt{\xi_0 l} = 300$-400 nm. A typical junction width of ∼200 nm is not much shorter than the coherence length leading to more complicated energy-phase relations [82]. However, experiments have found good agreement with theory for the short junction limit [83–85]

[5] A weak coupling might create many quasiparticles in the superconductor, which would be detrimental for superconducting qubits.

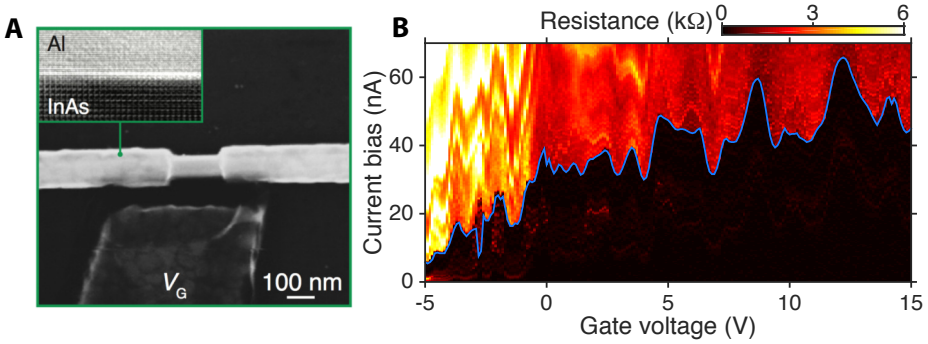

Figure 3.7: **A** The nanowire Josephson junction is formed by etching a small segment of the aluminum shell away. A nearby gate electrode tune the conductance of the semiconducting core. Inset shows the perfect crystalline interface between the InAs core and aluminum shell. **B** 4-probe resistance measurements of a nanowire based Josephson junction as a function of gate voltage and current bias. The critical current, I_c, of the junction is the lowest current value with non-zero resistance. The extracted critical current is indicated by a blue line.

so this assumption will be taken throughout the thesis.

In the extreme case of unity transmission across the junction the charge dispersion will completely vanish [86]. While this effect is small away from unity transmission the shape of the potential energy of the Josephson junction additionally modifies the anharmonicity of the gatemon. Following the same procedure as before, but with the energy-phase relation given by Equation (3.19), we can Taylor expand the potential and find the anharmonicity of the artificial atom. To fourth order in ϕ the potential is given by [80]

$$E \approx -E_J \left(\frac{2\pi}{\Phi_0}\right)^2 \frac{\hat{\phi}^2}{2} - E_J \left(1 - \frac{3\sum \tau_i^2}{4\sum \tau_i}\right) \left(\frac{2\pi}{\Phi_0}\right)^4 \frac{\hat{\phi}^4}{24}, \tag{3.20}$$

where $E_J = \Delta \sum \tau_i / 4$. Here E_J is defined such that the quadratic part has the same form as the transmon leading a harmonic energy spectrum with $\hbar\omega = \sqrt{8E_J E_C}$. The fourth order term can again be written using raising and lowering operators of the unperturbed system:

$$\begin{aligned} \widehat{V} &= -E_J \left(1 - \frac{3\sum \tau_i^2}{4\sum \tau_i}\right) \left(\frac{2\pi}{\Phi_0}\right)^4 \frac{\hat{\phi}^4}{24} \\ &= -\frac{E_C}{12} \left(1 - \frac{3\sum \tau_i^2}{4\sum \tau_i}\right) \left(\hat{a}^\dagger + \hat{a}\right)^4 \\ &\approx -\frac{E_C}{2} \left(1 - \frac{3\sum \tau_i^2}{4\sum \tau_i}\right) \left(\hat{a}^\dagger \hat{a}^\dagger \hat{a}\hat{a} + 2\hat{a}^\dagger \hat{a}\right). \end{aligned} \tag{3.21}$$

Calculating the first order energy corrections to the eigenstates yields an anharmonicity given by

$$\alpha = -E_C \left(1 - \frac{3\sum \tau_i^2}{4\sum \tau_i}\right). \tag{3.22}$$

High transmission junction lowers the anharmonicity by a factor in between 1 and 1/4. Figure 3.8 shows the potentials generated by low transmission junction, a junction with

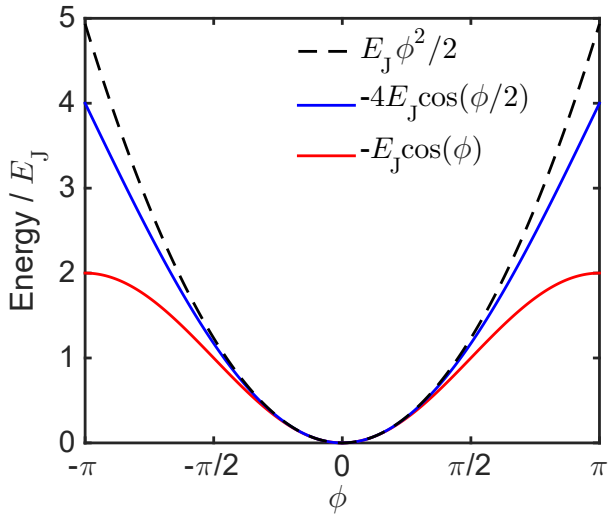

Figure 3.8: Josephson junction potentials for a tunnel junction, a junction with unity transmission, and their harmonic approximation in red, blue, and black respectively. The two cosine potentials are offset to match the harmonic potential at $\phi = 0$.

unity transmission, and a harmonic potential all with the same harmonic approximation. Indeed we see that the unity-transmission potential more closely resembles the harmonic potential leading to a lower anharmonicity.

3.4 Coupled Artificial Atoms and Harmonic Oscillators

With superconducting circuits acting as qubit we need a way to readout the state of the qubit without introducing noise. This can be done by coupling a qubit to a harmonic oscillator, which acts as a filter protecting the qubit from the environment while allowing state readout [57, 87, 88]. An artificial atoms and harmonic oscillators can be coupled through a capacitor C_g as shown in Figure 3.9. Here the resonator is modelled as a lumped element LC circuit but the theory also applies to resonators formed in distributed elements as shown in Figure 3.2. The qubit will have a separate coupling to each mode of the distributed cavity, however in practice only one of the modes has a significant coupling due to the energy separation.

The coupled circuit in Figure 3.9 has three flux nodes: ϕ_A, ϕ_r, and ground. Following the same procedure as in section 3.1 the Lagrangian is found as

$$\mathcal{L} = E(\phi_A) - \frac{C\dot{\phi}_A^2}{2} + \frac{\phi_r^2}{2L_r} - \frac{C_r\dot{\phi}_r^2}{2} - \frac{C_g(\dot{\phi}_r - \dot{\phi}_A)^2}{2}, \tag{3.23}$$

where $E(\phi_A)$ is the potential energy of the Josephson junction. Assuming $C_g \ll C_r, C$

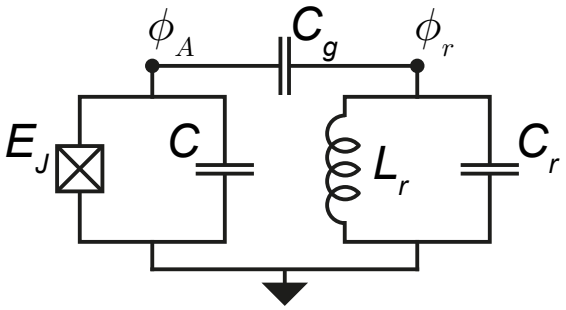

Figure 3.9: Schematic of an artificial atom coupled capacitively to a harmonic oscillator.

the conjugate momenta of each coordinate can be written as[6]

$$Q_A = \frac{\partial \mathcal{L}}{\partial \dot{\phi}_A} \approx C\dot{\phi}_A, \tag{3.24}$$

$$Q_r = \frac{\partial \mathcal{L}}{\partial \dot{\phi}_r} \approx C_r\dot{\phi}_r. \tag{3.25}$$

Performing a Legendre transformation and promoting the coordinates and their conjugate momenta to quantum operators yields the Hamiltonian of the system

$$\begin{aligned}\widehat{H} &= \frac{1}{2C}\widehat{Q}_A^2 + E(\hat{\phi}_A) + \frac{1}{2C_r}\widehat{Q}_r^2 + \frac{1}{2L}\hat{\phi}_r^2 + \frac{C_g}{CC_r}\widehat{Q}_r\widehat{Q}_A \\ &= \widehat{H}_A + \widehat{H}_r + \widehat{H}_g \end{aligned} \tag{3.26}$$

where $\widehat{H}_A$ and $\widehat{H}_r$ are the Hamiltonians for the isolated atom and resonator circuits respectively and $\widehat{H}_g$ is the coupling term. It is convenient to describe the system using eigenstates of the Hamiltonian with $\widehat{H}_g = 0$. In this case the eigenstates are simply product states of the uncoupled qubit and resonator which can be described by raising and lowering operators.

Focusing on the low-energy part of the atom spectrum we treat it as two-level, qubit system. Using raising and lowering operators and Pauli operators for isolated resonator and qubit respectively the Hamiltonian becomes[7]

$$\widehat{H} = \hbar\omega_r\hat{a}^\dagger\hat{a} + \hbar\frac{\omega_q}{2}\hat{\sigma}_z + \frac{2eC_g}{C}\langle 1|\hat{n}|0\rangle V_{\mathrm{ZPF}}(\hat{a} + \hat{a}^\dagger)(\hat{\sigma}_+ + \hat{\sigma}_-), \tag{3.27}$$

where $V_{\mathrm{ZPF}} = Q_{\mathrm{ZPF}}/C_r = \sqrt{\hbar\omega_r/2C_r}$ are the voltage zero-point fluctuations of the resonator[8], $\hat{n} = \widehat{Q}_A/2e$ is the number of Cooper pairs on the qubit capacitor C, and $|i\rangle$ are qubit states. Ignoring non-energy conserving terms in the coupling and collecting

[6] One finds a small modification to the effective capacitances of the resonator and artificial atom without this approximation as calculated in appendix of [58].

[7] We have changed the phase of the resonators raising and lowering operators $\hat{a}$ and $\hat{a}^\dagger$ as is conventional [58].

[8] For resonators formed in distributed elements V_{ZPF} is position dependent along the resonator and one needs to calculate $V_{\mathrm{ZPF}}(x)$ at the qubit position x.

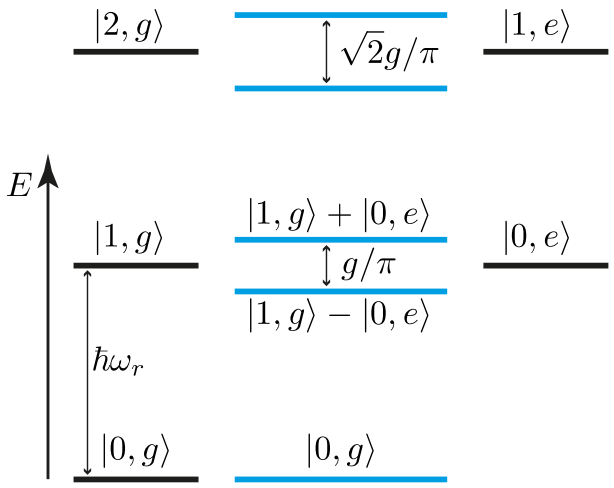

Figure 3.10: The energy spectrum of the Jaynes-Cummings Hamiltonian in the resonant regime with $\omega_r = \omega_q$. Left are the states $|n, g\rangle$ where n is the number of photons in the resonator and $|g\rangle$ is the ground state of the qubit. Adding a photon to the resonator states increases the energy by $\hbar\omega_r$. Right are states $|n, e\rangle$ where $|e\rangle$ is the excited state of the qubit raising the energy by $\hbar\omega_q$. In blue are the eigenstates of the coupled system described by Equation (3.28).

factors as $\hbar g = \frac{2eC_g}{C}\langle 1|\hat{n}|0\rangle V_{\text{ZPF}}$ we arrive at the Jaynes-Cummings Hamiltonian:

$$\widehat{H} = \hbar\omega_r \hat{a}^\dagger \hat{a} + \hbar\frac{\omega_q}{2}\hat{\sigma}_z + \hbar g(\hat{a}\hat{\sigma}_+ + \hat{a}^\dagger\hat{\sigma}_-). \tag{3.28}$$

There are two distinct regimes for the Jaynes-Cummings Hamiltonian. The resonant regime when $\omega_r = \omega_q$ and the dispersive regime with $|\omega_q - \omega_r| \gg g$. In the resonant regime the qubit and resonator states hybridize as shown in Figure 3.10. In the one excitation manifold the eigenstates are superpositions of a photon in the resonator and an excitation in the qubit. The splitting of the resonator state is known as the vacuum-Rabi splitting as a qubit excitation does Rabi oscillations with the vacuum state of the resonator. To observe the splitting we need g/π to be larger than the linewidth of both the qubit and resonator. Observing vacuum-Rabi splitting demonstrates strong and coherent qubit-resonator coupling but the regime is not suitable for quantum processing.

For quantum processing we want to be in the dispersive regime where the qubit frequency is far detuned from the resonator frequency. This regime allows us to simplify the Jaynes-Cummings Hamiltonian in Equation (3.28) by expanding to second order in the small parameter g/Δ, where $\Delta = \omega_q - \omega_r$ is the detuning. One has to be careful when doing the expansion as higher energy levels of the artificial atom are important. Therefore the expansion is done on the full multilevel system and then truncated to a two level system afterwards [67]. The total system of a multilevel artificial atom coupled

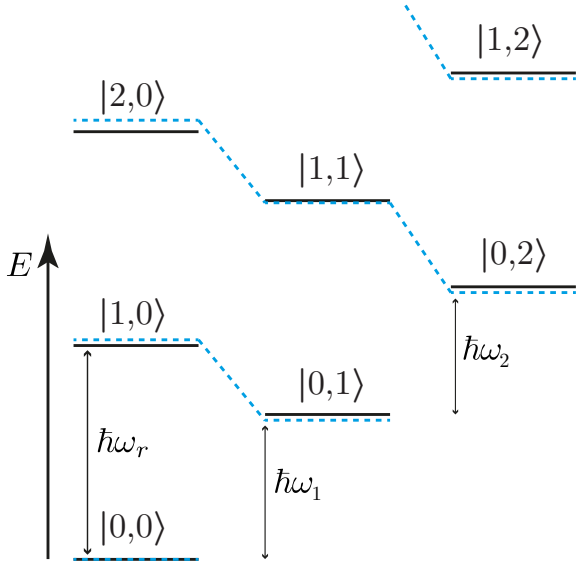

Figure 3.11: Energy spectrum of the Jaynes-Cummings Hamiltonian in the dispersive regime shown in Equation (3.30). Energy states $|n, j\rangle$, where n is number of photons in the resonator and j is the number of excitations on the transmon, depicted as black for coupling off and dashed blue for coupling on. State $|1, 1\rangle$ couples to both states $|0, 2\rangle$ and $|2, 0\rangle$ which gives a dispersive shift in opposite directions.

to a harmonic oscillator is described by the generalized Jaynes-Cummings Hamiltonian:

$$\begin{aligned} \widehat{H} &= \widehat{H}_0 + \widehat{V}, \\ \widehat{H}_0 &= \hbar\omega_r \hat{a}^\dagger \hat{a} + \hbar \sum_i \omega_i |i\rangle\langle i|, \\ \widehat{V} &= \hbar \sum_i g_{i,i+1}(\hat{a}|i+1\rangle\langle i| + \hat{a}^\dagger |i\rangle\langle i+1|). \end{aligned} \tag{3.29}$$

The coupling strength is given by $g_{ij} = \frac{2eC_g}{\hbar C}\langle i|\hat{n}|j\rangle V_{\text{ZPF}}$. Here we assume that the artificial atom is a transmon with $E_J \gg E_C$ which leads to $g_{ij} = 0$ for $i \neq i \pm 1$. For other artificial atoms the matrix elements $\langle i|\hat{n}|j\rangle$ can have very different selection rules. The Hamiltonian can be simplified using second order perturbation theory treating the interaction term $\widehat{V}$ as a perturbation. Eigenstates for H_0 are readily found as $|n, j\rangle$ where n is the resonator photon number and j is the excitation level of the artificial atom. An explicit calculation can be found in Appendix A leading to the Hamiltonian:

$$\widehat{H} = \hbar\left(\omega_r - \frac{\chi_{12}}{2}\right)\hat{a}^\dagger\hat{a} + \hbar\frac{1}{2}(\omega_q + \chi_{01})\hat{\sigma}_z + \hbar\chi\hat{a}^\dagger\hat{a}\hat{\sigma}_z \tag{3.30}$$

where $\chi_{ij} = g_{ij}^2/(\omega_{ij} - \omega_r)$ and $\chi = \chi_{01} - \chi_{12}/2$.[9] Figure 3.11 depicts the lowest energy levels of the Jaynes-Cummings Hamiltonian in the dispersive regime.

There are three terms in the Hamiltonian originating from the coupling. The first two terms are called *Lamb shifts* giving a correction to the qubit and resonator frequencies.

[9] If the system is truncated before the approximation all terms with χ_{12} vanish as state $|2\rangle$ is absent.

The last term can be interpreted in two ways. It can be viewed as a correction to the qubit frequency dependent on the number of photons in the resonator [89]. This is known as the Stark shift of the qubit and can be exploited to measure photon number states in the resonator [60, 90]. Equally valid it can be interpreted as a qubit dependent dispersive shift of the resonator:

$$\widehat{H} = \hbar\left(\omega_r' + \chi\sigma_z\right)\hat{a}^\dagger\hat{a} + \hbar\frac{1}{2}\omega_q'\hat{\sigma}_z, \tag{3.31}$$

where $\omega_q' = \omega_q + \chi_{01}$ and $\omega_r' = \omega_r - \chi_{12}$. Written in this form the Hamiltonian explicitly shows a qubit state dependent shift on resonance frequency of the resonator. The dispersive shift in the transmon limit is given by $\chi = \alpha g^2/\Delta(\Delta+\alpha)$, where α is the anharmonicity of the qubit. By probing the frequency of the resonator with a classical microwave tone we can infer the qubit state. Furthermore, this is a quantum non-demolition (QND) readout scheme as the qubit state is an eigenstate of the Hamiltonian, which means that the qubit is left in the measured state after readout [57]. This can be exploited to perform qubit state preparation with fast measurement feedback [91, 92].

The resonator is coupled to the measurement apparatus leading to a photon decay rate, κ, or the resonator. As the qubit is coupled to the resonator the photon decay will induce a qubit decay known as the Purcell effect [93]. For large detuning the induced qubit decay is given by $\gamma \approx (g/\Delta)^2\kappa$ [88]. The speed of qubit readout is limited by κ, the rate of photons leaking out to instruments, while qubit lifetime is limited by $1/\kappa$. Depending on the scope of the experiment one might need to suppress the Purcell effect to allow for fast measurements without compromising qubit lifetimes [94–97].

3.5 Single Qubit Control

For qubit control we return to the simple transmon circuit capacitively coupled to a voltage source [Figure 3.4] whose Hamiltonian is

$$\widehat{H} = 4E_C\hat{n}^2 - E_J\cos\left(\hat{\varphi}\right) + \frac{2eC_g}{C}V_g(t)\hat{n}, \tag{3.32}$$

where $V_g(t)$ is separated as an individual term. Qubit operations are achieved by applying an ac voltage $V_g(t) = v_R\cos(\omega t) + v_I\sin(\omega t)$ where v_R and v_I are the in phase and out of phase components of the voltage respectively. Writing the Hamiltonian in eigenstates of the undriven artificial atom we have

$$\widehat{H} = \sum_i \hbar\omega_i|i\rangle\langle i| + \sum_{i,j} 2e\beta\langle i|\hat{n}|j\rangle\left[v_R\cos(\omega t) + v_I\sin(\omega t)\right]\left(|j\rangle\langle i| + |i\rangle\langle j|\right), \tag{3.33}$$

where $\beta = C_g/C$. Focusing on a two-level subspace spanned by states $|0\rangle$ and $|i\rangle$ the Hamiltonian can be written with Pauli operators:

$$\widehat{H} = \frac{\hbar\omega_i}{2}\hat{\sigma}_{z,i} + 2e\beta\langle 0|\hat{n}|i\rangle\left[v_R\cos(\omega t) + v_I\sin(\omega t)\right]\left(\hat{\sigma}_{+,i} + \hat{\sigma}_{-,i}\right), \tag{3.34}$$

where $\hat{\sigma}_{z,i} = |i\rangle\langle i| - |0\rangle\langle 0|$, $\hat{\sigma}_{+,i} = |i\rangle\langle 0|$, and $\hat{\sigma}_{-,i} = |0\rangle\langle i|$. In a rotating frame of the drive and invoking the rotating wave approximation the Hamiltonian reduces to

$$\begin{aligned}\widehat{H}_R &= e^{i\omega t\hat{\sigma}_{z,i}/2}\widehat{H}e^{-i\omega t\hat{\sigma}_{z,i}/2} - \frac{\hbar\omega}{2}\hat{\sigma}_{z,i} \\ &= \frac{\hbar(\omega_i - \omega)}{2}\hat{\sigma}_{z,i} + \frac{\hbar}{2}[\Omega_{R,i}\hat{\sigma}_{x,i} - \Omega_{I,i}\hat{\sigma}_{y,i}],\end{aligned} \tag{3.35}$$

where $\Omega_{j,i} = \frac{2e}{\hbar}\beta\langle 0|\hat{n}|i\rangle v_j$ are Rabi frequencies. A classical microwave signal $V(t)$ on an electrode capacitively coupled to the artificial atom can drive the system from $|0\rangle$ to $|i\rangle$ and back with a frequency given by $\Omega_{j,i}$. With independent control of $\Omega_{R,i}$ and $\Omega_{I,i}$ we can drive the two-level system around an arbitrary axis in the XY plane of the Bloch sphere. For transmons with $E_J \gg E_C$ the only non-zero matrix elements are $\langle i|\hat{n}|i+1\rangle$ allowing us to focus on just the 0-1 transition. However, as we will see in Chapter 6, more exotic circuits can have tunable matrix elements leading to some transitions appearing and disappearing as they are tuned.

For tunable transmons, e.g. gatemons, one can tune the qubit frequency. Limiting the Hamiltonian to a truncated qubit subspace with resonance frequency ω_q the Hamiltonian of a gatemon can, in the rotating frame of the drive, be written as

$$\widehat{H}_R = \frac{\hbar}{2}[\delta_q(V_c)\hat{\sigma}_z + \Omega_R\hat{\sigma}_x - \Omega_I\hat{\sigma}_y], \tag{3.36}$$

where $\delta_q(V_c) = \omega_q(V_c) - \omega$ is the qubit-drive detuning and V_c is the control voltage tuning E_J of the Josephson junction. With independent and fast control of all parameters δ_q, Ω_R, and Ω_I we have complete control of the qubit system.

Here we considered a drive signal, $V_g(t)$, applied to a nearby electrode capacitively coupled to the artificial atom. Alternatively one might apply the drive signal through a readout cavity coupled to the artificial atom. In this case the cavity will act as a filter on the drive signal reducing the effective Rabi frequencies dependent on the cavity-qubit coupling and detuning: $\Omega_j = \frac{g}{\Delta}\left[\frac{2e}{\hbar}\beta\langle 0|\hat{n}|i\rangle v_j\right]$, but otherwise behaves the same as a direct capacitive coupling [58].

3.6 Two-Qubit Operations

For universal quantum processing we also need to engineer qubit-qubit interactions. Fortunately, it is sufficient to have just one entangling two-qubit gate. For transmon qubits there are several ways to implement two-qubit gates [98–101]. Here we will focus on one of the most widely used two-qubit gates: the controlled phase gate (CZ gate) [102, 103]. The CZ gate performs a Z gate on a target qubit dependent on the state of a control qubit. Implementations of two-qubit gates relies both on an engineered coupling and control pulses used to perform the gate.

There are a multiple ways to engineer a qubit-qubit couplings for transmons. One is a direct capacitive coupling that is very similar to the qubit resonator coupling [104] while another is a coupling mediated by a resonator [105], which was used for the first

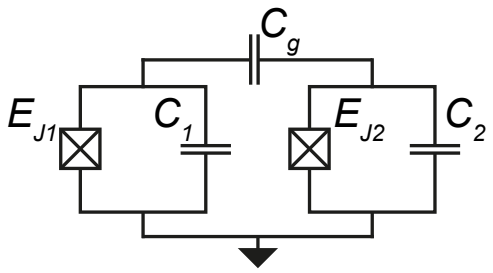

Figure 3.12: Two transmon qubits coupled capacitively.

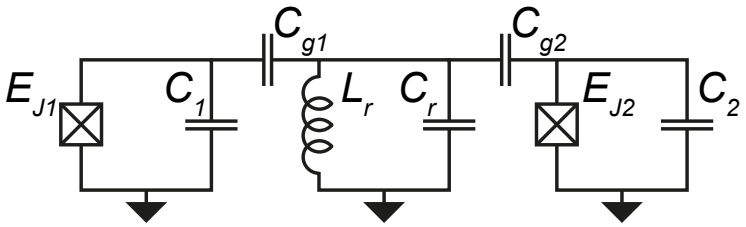

Figure 3.13: Two transmon qubits coupled via a resonator.

demonstration of two-qubit operations in transmon qubits.

Two transmons can be coupled as shown schematically in Figure 3.12. Notice the similarity of the circuit to that of a transmon coupled to a harmonic oscillator in Figure 3.9. Following the same procedure leading to the Jaynes-Cummings Hamiltonian in Equation (3.28) but truncating both transmons to two-level systems it is straightforward to find the Hamiltonian as

$$\widehat{H} = \hbar\frac{\omega_1}{2}\hat{\sigma}_{z,1} + \hbar\frac{\omega_2}{2}\hat{\sigma}_{z,1} + \hbar J(\hat{\sigma}_{-,1}\hat{\sigma}_{+,2} + \hat{\sigma}_{+,1}\hat{\sigma}_{-,2}), \tag{3.37}$$

where ω_1 and ω_2 are the resonance frequencies of qubit 1 and 2 respectively and $J = \frac{(2e)^2 C_g}{C_1 C_2}\langle 0|_1 \hat{n}_1 |1\rangle_1 \langle 1|_2 \hat{n}_2 |0\rangle_2$ is the qubit-qubit coupling strength. In the transmon limit we can write the coupling term as $J = \frac{C_g\sqrt{\omega_1\omega_2}}{2\sqrt{C_1 C_2}}$. If the qubits are far detuned in frequency the coupling term becomes negligible due to energy conservation. By pulsing the qubits into resonance, for instance by changing the gate voltage on a nanowire Josephson junction, one can turn on the coupling for a short time to perform a gate.

A somewhat more involved system is the qubit-resonator-qubit circuit shown in Figure 3.13. The Hamiltonian in the rotating wave approximation takes the form of a Jaynes-Cummings Hamiltonian with qubit-resonator couplings for each qubit

$$\widehat{H} = \hbar\omega_r \hat{a}^\dagger \hat{a} + \hbar\sum_i \frac{\omega_i}{2}\hat{\sigma}_{z,i} + \sum_i \hbar g_i(\hat{a}\hat{\sigma}_{+,i} + \hat{a}^\dagger\hat{\sigma}_{-,i}). \tag{3.38}$$

This Hamiltonian is known as the Tavis-Cummings Hamiltonian and describes the coupling of multiple qubits to a single harmonic mode. As for readout we want to be in the dispersive limit where both qubits are far detuned from the resonator. In the dispersive

limit where $g_1, g_2 \ll \Delta_1, \Delta_2$ the Hamiltonian can be written as [106]

$$\widehat{H} = \hbar\left(\omega_r' + \chi_1\hat{\sigma}_{z,1} + \chi_2\hat{\sigma}_{z,2}\right)\hat{a}^\dagger\hat{a} + \sum_{i=1}^{2}\frac{\hbar\omega_i'}{2}\hat{\sigma}_{z,i} + \hbar g_1 g_2\frac{\Delta_1+\Delta_2}{2\Delta_1\Delta_2}(\hat{\sigma}_{+,1}\hat{\sigma}_{-,2} + \hat{\sigma}_{-,1}\hat{\sigma}_{+,2}), \tag{3.39}$$

where $g_i = \frac{2eC_{gi}}{C_i}\langle 1|_i\hat{n}_i|0\rangle_i V_{\mathrm{ZPF}}$ and $\Delta_i = \omega_i - \omega_r$. The coupling term is the same as for the direct coupling with a strength determined by the qubits' coupling to the resonator and how far detuned they are. When the two qubits are on resonance the coupling strength is g_1g_2/Δ.

Both implementations of qubit-qubit coupling lead to the same effective Hamiltonian. Experimentally there are pros and cons of both layouts and the choice of coupling depends on the specific experiments needs. A distributed coupling cavity allows extra space as the qubits can be coupled over long distances. This suppresses any unwanted crosstalk between qubits for single qubit gates as well as allowing extra space for control wirering such as readout resonators and gate lines. On the other hand adding a cavity to mediate the coupling also adds a decay channel as well as one more element that can fail during fabrication.

The coupling between qubits in this implementation is a fixed coupling strength which is dynamically turned on by pulsing the qubits into resonance. Figure 3.14 shows the level spectrum for two coupled transmons. Blue lines are the single-excitation energies, with an avoided crossing between states $|01\rangle$ and $|10\rangle$, while red shows two-excitation energies and coupling between states $|02\rangle$ and $|11\rangle$. Two types of two-qubit gates can be performed in this spectrum. One is an iSWAP gate performed by pulsing the energy of the qubit 1 diabatically into the $|10\rangle$-$|01\rangle$ anticrossing for a certain time[10]:

$$\begin{aligned} i\mathrm{SWAP}|00\rangle &= |00\rangle, \quad i\mathrm{SWAP}|11\rangle = |11\rangle, \\ i\mathrm{SWAP}|01\rangle &= -i|10\rangle, \quad i\mathrm{SWAP}|10\rangle = -i|01\rangle. \end{aligned} \tag{3.40}$$

The gate set of iSWAP and single qubit gates is in fact a universal gate set [107].

Unfortunately due to the low anharmonicity of a transmon qubit one has to consider the effect of higher energy states shown in red. The coupling term in Equation (3.37) also couples states $|02\rangle \leftrightarrow |11\rangle$ and $|20\rangle \leftrightarrow |11\rangle$. To avoid any leakage errors the pulse scheme used to implemented two-qubit gates needs to suppress any $|02\rangle$ or $|20\rangle$ population after each gate. This poses a problem for the iSWAP operation which requires a diabatic pulse to bring the two qubits on resonance. Such a pulse will have to move through the avoided crossing between states $|02\rangle$ and $|11\rangle$ (or $|20\rangle$ and $|11\rangle$), which will cause leakage errors if the pulse is not fast enough. Experimentally it turns out to be challenging to avoid any leakage leading experimenters to come up with another type of two-qubit gates in transmons.

The idea is to take advantage of the $|02\rangle \leftrightarrow |11\rangle$ anticrossing while avoiding any leakage by clever pulse shaping [102]. A diabatic pulse into the $|02\rangle \leftrightarrow |11\rangle$ anticrossing

[10]Such a pulse will also perform a single qubit phase operation which has not been included in this discussion for simplicity. One can easily correct for the phase operation e.g. with a single qubit phase operation after the two-qubit operation.

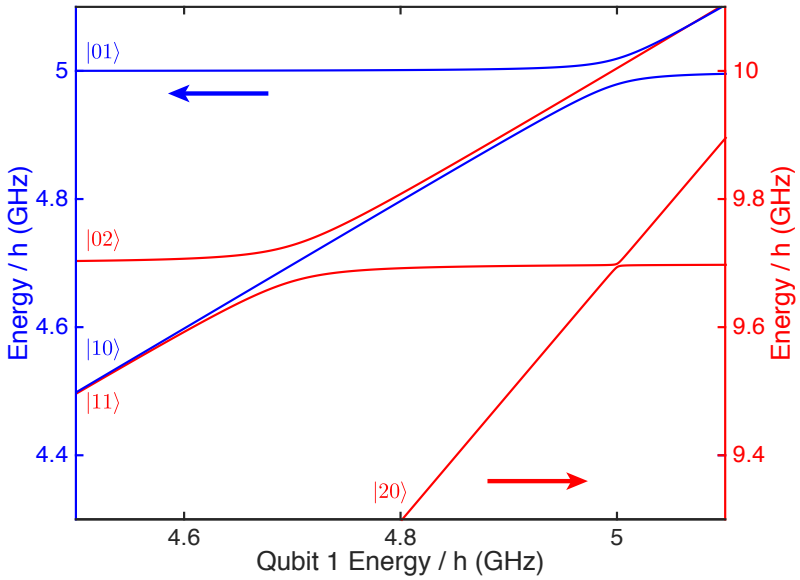

Figure 3.14: Energy spectrum of two coupled transmons as a function qubit 1 energy with fixed energy for qubit 2. Blue (red) indicates the one-excitation (two-excitation) manifold with the energy shown on the left (right) axis. Qubit 2 has energy $\omega_2/2\pi = 5$ GHz, the anharmonicity of both qubits is $\alpha/2\pi = -300$ MHz, and coupling strength $J/2\pi = 20$ MHz.

will after a time implement a controlled phase (CZ) gate due to state oscillations of $|11\rangle$ and $|02\rangle$:

$$\begin{aligned} \mathrm{CZ}|00\rangle &= |00\rangle, \quad \mathrm{CZ}|11\rangle = -|11\rangle, \\ \mathrm{CZ}|01\rangle &= |01\rangle, \quad \mathrm{CZ}|10\rangle = |10\rangle. \end{aligned} \tag{3.41}$$

The CZ gate avoids the complexity of interacting with multiple anticrossings in the same pulse. More recent implementations makes use of a fast adiabatic approach to the avoided crossing keeping the state in an eigenstate at all times [103, 108]. Such a pulse has the advantage of limiting leakage simply by making the pulse slower. Furthermore, it is experimentally much easier to implement adiabatic pulses than diabatic due the the limited bandwidth of control electronics and cabling.

Chapter 4

Fabrication and Experimental Setup

4.1 Fabrication

Device fabrication of superconducting qubits is an extended process requiring several advanced techniques. Furthermore, losses in superconducting qubits can easily be limited by loss tangent of the materials and the quality of the materials interfaces formed during fabrication [109–112]. Consequently, optimizing qubit lifetimes is a tight loop with the fabrication processes.

For nanowire-based devices the fabrication is further complicated by the somewhat random placement of the nanowire requiring manual design adjustments for each nanowire[1]. The individual steps of the process are fairly standard involving either e-beam or UV lithography followed by a lift-off or etch-back process. A detailed list of processes for each sample presented in this thesis can be found in Appendix D. The general process flow of nanowire-based superconducting circuits can be divided into two stages: before nanowire deposition and after nanowire deposition.

The first stage defines the large scale cQED circuits, e.g. resonators and qubit islands. At this level every device is identical and can beneficially be fabricated simultaneously on a single wafer. For small scale cleanrooms, such as the one used at Center for Quantum Devices, 2" wafers containing a few tens of chips is a good compromise between parallel fabrication and tool availability. As this stage is parallel fabrication of tens of devices one wants to do as much of the fabrication as possible during this stage.

Before the second stage the wafer is cut up in smaller chips containing only a few devices. Much of the work in this stage scales with the number nanowires rather than the number of chips. The nanowire placement can be done in two fashions. A random placement via a tissue transferring tens of nanowires from growth chip to device chip as described in [114]. This is a fairly fast process but is rather uncontrolled. Alternatively one can use a micromanipulator, which is a needle controlled to sub micrometer scale,

[1] This can be mitigated with image recognition software [113].

installed under a microscope to transfer individual nanowires from the growth chip to desired location and orientation on device chip. This is a very tedious and time consuming process but necessary if the placement of the nanowire is crucial, e.g. bottom gate structures.

Following placement of InAs/Al core/shell nanowires a small segment of the shell needs to be etched away to form Josephson junctions. The process resulting in best nanowire etches during my work has been a 9-12 s, 50° C Transcene D etch[2] with e-beam lithography windows defined in PMMA directly followed by thorough rinsing in DI water. While giving good results it is a very sensitive process with far from 100 % yield.

4.2 Experimental Setup

Detailed schematics of the each setup used are given in Appendix C.

Superconducting qubit devices are very sensitive to radiation both at the qubit frequency and in THz (infrared light) frequencies leading to quasiparticle excitations. It is therefore crucial to properly shield devices from any black-body radiation of higher temperature stages [115, 116]. This is commonly done by multiple closed boxes with light absorbing coatings. Any residual light entering a box should be absorbed far away from the device. For measurements in Chapters 5 and 6 we use an aluminium box inside a copper box both coated by light-absorbing paint. The box for high-field compatibility in Chapter 7 is made of CuBe and filled with light absorbing foam. Similarly any electrical connection to the device is carefully filtered or heavily attenuated.

Throughout the thesis three measurement techniques are used to probe the devices:

- **Single-tone spectroscopy:** the frequency response of the readout resonator is measured with a vector network analyser.
- **Two-tone spectroscopy:** the resonator is monitored by a 'readout' tone at a fixed frequency while a second 'drive' tone is swept. When the drive tone is on resonance with the qubit it will induce excitations leading to a peak in the transmission of the monitored readout tone.
- **Time-domain measurements:** A drive tone is turned on for a controlled time inducing rotations of the qubit state followed by a readout tone probing the resonator transmission.

Two-tone spectroscopy is a fairly time-consuming measurement both due to the amount of data taken and due to slow sweeping of drive tone frequency. Most microwave signal generators are fairly slow at changing frequency leading to a great deal of 'dead time', where no measurements are performed. For faster data acquisition we take advantage of features on a Rhode & Schwarz ZNB vector network analyser (VNA) allowing to decouple output frequency and measurement frequency. A VNA is optimized for frequency sweeping, which we utilize for the drive tone while the VNA monitors the response of the readout tone at a fixed frequency. For a VNA with 4 ports the unit can

[2]Etch time is dependent on shell thickness: 9 s for 7 nm half shell and 12 s for 30 nm thick full shell.

output two tones: one is set to a fixed readout frequency probing transmission of the resonator while the second tone is swept to probe the qubit frequency. For a VNA with 2 ports the unit can output one tone which is used to probe the qubit frequency. The readout tone is measured by the VNA but generated by a separate Rhode & Schwarz SGS100A signal generator.

For measurements affecting the resonance frequency of the readout resonator it is essential to continuously adjust the frequency of the readout tone. As both single-tone spectroscopy, probing the resonator frequency, and two-tone spectroscopy is performed by the VNA one can swap between each technique in software. This allows one to first probe the resonator and adjust the readout frequency used in two-tone spectroscopy without substantially extending the measurement time.

All time domain measurements are controlled by a Tektronix AWG 5014C. The arbitrary waveform generator (AWG) handles the envelopes of RF signals by IQ modulation of vector signal generators controlling the amplitude of the in phase and out of phase components. With the RF signal on resonance with the qubit each component corresponds to $\Omega_R(t)$ and $\Omega_I(t)$ in equation 3.36, which rotates the qubit around x and y axis of the Bloch sphere. For high fidelity gates further pulse modulation, in addition to IQ modulation, of the signal generator is used to reduce residual microwave leakage in the nominally off-state. A line from the AWG is combined with a DC voltage source via an RC bias-T either at room temperature or at base temperature for nanosecond control of the gate voltage controlling E_J. Similarly to the qubit dive the output of the readout tone is modulated by the AWG. It is measured with heterodyne demodulation by first down converting the signal to an intermediate frequency ($10 - 30$ MHz) and then measured by an AlazarTech ATS9360 waveform digitizer followed by digital demodulation [117].

Chapter 5

Semiconductor-Based Superconducting Qubits

Transmon qubits have over the last decade proven to be promising candidates for scalable quantum computing based on quantum error correction. The experimental implementation is incredible robust due to the simplicity of the qubit and control circuitry. Furthermore, transmon qubits generally either works or has a 'catastrophic' failure resulting in fast response on device quality. Within a day of measurements the main figures of merit, such as lifetime and coherence time, can be extracted leading to fast optimization loops between fabrication and measurements. In addition, as transmons commonly have one or no tuning parameter, the experimental phase space to be explored for best qubit performance is limited. These factors collected have allowed superconducting qubit performance to increase exponentially over the years leading to state-of-the-art qubits at the border of quantum error correction.

Transmon qubits are commonly based around aluminium tunnel junctions. An alternative approach is based on supersonductor-semiconductor Josephson junction taking advantage of the field effect tunability of semiconductors presented in section 3.3. This chapter presents the development of gatemon qubits. The first section introduces the gatemon qubit and has previously been published in [73]. The second part explores the gate fidelities of Clifford gates needed for quantum error correction as well as implementing two-qubit gates. Data presented in this section has previously been published in [118].

5.1 The Gatemon

This section presents data from two gatemon devices, which show similar performance. Except where noted, data are from the first device. The qubit features a single InAs Josephson junction shunted by a capacitance, C_S [17, 67, 119]. The Josephson junction is formed from a molecular beam epitaxy-grown InAs nanowire, $\sim$ 75 nm in diameter, with an *in situ* grown $\sim$ 30 nm thick Al shell. The Al shell forms an atomically matched

Al-InAs interface leading to a proximity induced gap in the InAs core with a low density of states below the superconducting gap (hard gap) [31, 78]. By wet etching away a ~ 80 nm segment of the Al shell [Figure 5.1**A**] a weak link in the superconducting shell is formed, creating the Josephson junction [see section 4.1 for details]. A supercurrent leaking through the semiconductor core links the unetched regions and determines the Josephson coupling energy, $E_{\mathrm{J}}(V_{\mathrm{G}})$, which can be tuned by changing the electron density in the semiconductor core with a nearby side gate voltage, V_{G}.

As with conventional transmons, the gatemon operates as an anharmonic LC oscillator with a nonlinear inductance provided by the Josephson junction. The total capacitance of the gatemon qubit C_{Σ} is determined by the capacitance of the T-shaped Al island to the surrounding Al ground plane, as shown in Figure 5.1**C**. The gatemon operates with $E_{\mathrm{J}} \gg E_{\mathrm{C}}$, where the charging energy, $E_{\mathrm{C}} = e^2/2C_{\Sigma}$. In this regime, decoherence due to either low frequency charge noise on the island or quasiparticle tunneling across the Josephson junction is strongly suppressed. For many conducting channels in the wire, the qubit transition frequency is given by $f_{\mathrm{Q}} = E_{01}/h \approx \sqrt{8E_{\mathrm{C}}E_{\mathrm{J}}(V_{\mathrm{G}})/h}$. The difference between E_{01} and the next successive levels, E_{12}, is the anharmonicity, $\alpha = E_{12} - E_{01} \approx -E_{\mathrm{C}}$. From electrostatic simulations we estimate a charging energy of $E_{\mathrm{C}}/h \approx 200$ MHz ($C_{\Sigma} \approx 94$ fF). With this charging energy and $E_{01}/h = 6$ GHz we get $I_c = eE_{01}^2/4E_{\mathrm{C}}\hbar = 45$ nA (with an effective junction inductance of 7.3 nH), consistent with transport measurements on the same kind of nanowires in Figure 3.7. From microwave spectroscopy of our gatemon we measure $\alpha/h \approx 100$ MHz. The discrepancy between the measured anharmonicity and $-E_{\mathrm{C}}$ is due to a nonsinusoidal current-phase relation for the nanowire Josephson junction resulting in a reduced nonlinearity in the Josephson inductance [74, 80].

The gatemon is coupled to a $\lambda/2$ superconducting transmission line cavity with a bare resonance frequency $f_{\mathrm{C}} = 5.96$ GHz and quality factor, $Q \sim 1500$. The cavity is used for dispersive readout of the qubit with homodyne detection Figure 5.1**D**. The frequencies of the microwave signals used to control and readout the qubit are indicated as f_Q and f_C respectively. Both the cavity and qubit leads are patterned by wet etching an Al film on an oxidized high-resistivity Si substrate. Nanowires are transferred from the growth substrate to the device chip using a dry deposition technique [114]. During transfer, a PMMA mask ensures nanowires are only deposited on the device inside a 85 μm $\times$ 56 μm window where the Josephson junction is fabricated. Following the nanowire shell etch, the nanowire contacts and gate are patterned from Al using a lift-off process with an ion mill step to remove the native Al_2O_3 prior to deposition. Measurements are performed with the sample inside an Al box mounted at the mixing chamber of a cryogen-free dilution refrigerator with a base temperature < 50 mK [Figure C.1].

To directly measure the qubit-cavity coupling the gatemon is tuned with the gate voltage into resonance with the lowest mode of the cavity. This is the resonant regime of the Jaynes-Cummings Hamiltonian. In Figure 5.2**A** the cavity response is shown as a function of gate voltage and cavity drive frequency for low driving power. We observe two transmission peaks in the cavity aperiodically modulated by the gate voltage on the gatemon. The aperiodicity is consistent with mesoscopic fluctuations in the conductance

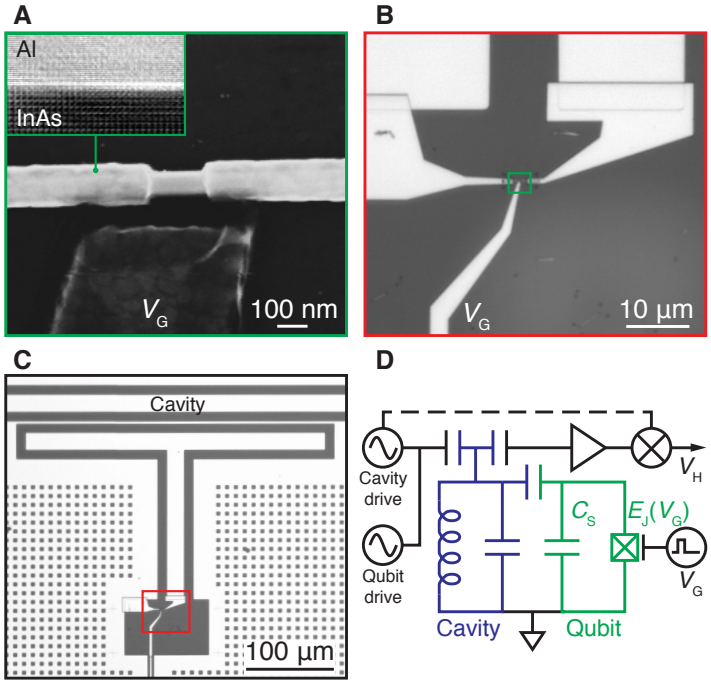

Figure 5.1: **A** The nanowire Josephson junction integrated into a transmon circuit. **B** The nanowire is contacted at each end and a nearby gate electrode can tune the Josephson energy of the junction. **C** The transmon is formed by a T-shaped island shorted to the surrounding ground plane through the nanowire Josephson junction. The transmon circuit is closed by the capacitance of the island to ground. The island is capacitively coupled to a $\lambda/2$ microwave cavity for readout. **D** Schematic of the gatemon circuit.

of the nanowire junction. The two peaks are the hybridized cavity-gatemon states [66]. Two widely split peaks, Figure 5.2**B**, indicate a cavity-gatemon in the strong coupling regime with g larger than both the decay rate of the qubit and the cavity. Off resonance the qubit-cavity states are very weakly hybridized and we only observe one peak, the cavity resonance.

To better estimate the coupling strength g we extract the peak splitting δ for each voltage value with two peaks in 5.2**A**. The hybridized states, $f_{\pm}$, can be calculated from the coupling strength g,

$$f_{\pm} = \frac{f_Q + f_C \pm \sqrt{(f_Q - f_C)^2 + 4(g/2\pi)^2}}{2}, \tag{5.1}$$

where f_C and f_Q are the frequencies of the uncoupled cavity and qubit respectively. By plotting the peak splitting $\delta = f_+ - f_- = \sqrt{(f_Q - f_C)^2 + 4(g/2\pi)^2}$ as a function of f_Q as shown in Figure 5.2**C** we extract a coupling strength $g/2\pi = 99$ MHz. Plotting the data in 5.2**A** parametrically as a function of the extracted f_Q the expected avoided crossing of a coupled two-level system is revealed in Figure 5.2**D**.

To perform coherent operation on the gatemon, we detune it away from the cavity frequency to the dispersive regime. While continuously monitoring the cavity transmission at the cavity frequency we sweep a second microwave tone to drive the qubit. When the qubit drive, the second tone, hits the resonance frequency of the qubit, the qubit is excited into an incoherent superposition of $|0\rangle$ and $|1\rangle$ which modulates the monitored cavity transmission. By sweeping the frequency of the qubit drive and the gate voltage we map out the spectrum of the gatemon in Figure 5.3. In the spectrum we directly observe the aperiodic modulation of the gatemon frequency originating from mesoscopic fluctuations in the nanowire. These fluctuations create local minima and maxima that are first-order insensitive to gate voltage (sweet spots). We also observe discontinuous jumps in the spectrum that we attribute to charge traps near the nanowire changing the charge landscape. Such jumps rarely happen when the gate voltage is restricted to a small voltage range.

Figure 5.4**A** shows a scan of the qubit spectrum around the sweet spot at 3.4 V. Here spectroscopy is performed by first applying a 2 μs long qubit drive tone and then probing the cavity response to avoid Stark shift in the data. To perform qubit operations on the gatemon we fix the gate voltage at 3.4 V indicated by B. In the top panel of Figure 5.4**B** the pulse scheme for Rabi oscillations is shown. First a qubit drive tone of length τ rotates the qubit about the X axis and then a readout tone measures the probability for the qubit to be in the $|1\rangle$ state. The lower part of the main panel shows Rabi oscillations as the qubit is rotated around the Bloch sphere. When the qubit drive is detuned from the resonance frequency the qubit does not fully reach the $|1\rangle$ state as seen in the amplitude of the oscillations. The rotation axis is the combination of the drive strength along the X axis plus a constant $\hat{\sigma}_z$ contribution due to the detuning (see equation (3.36)). This also causes a faster oscillation frequency. By sweeping the drive time and drive detuning we can see the effect as the Chevron pattern in the main panel.

While drive pulses around an axis in the XY plane are enough to perform all single

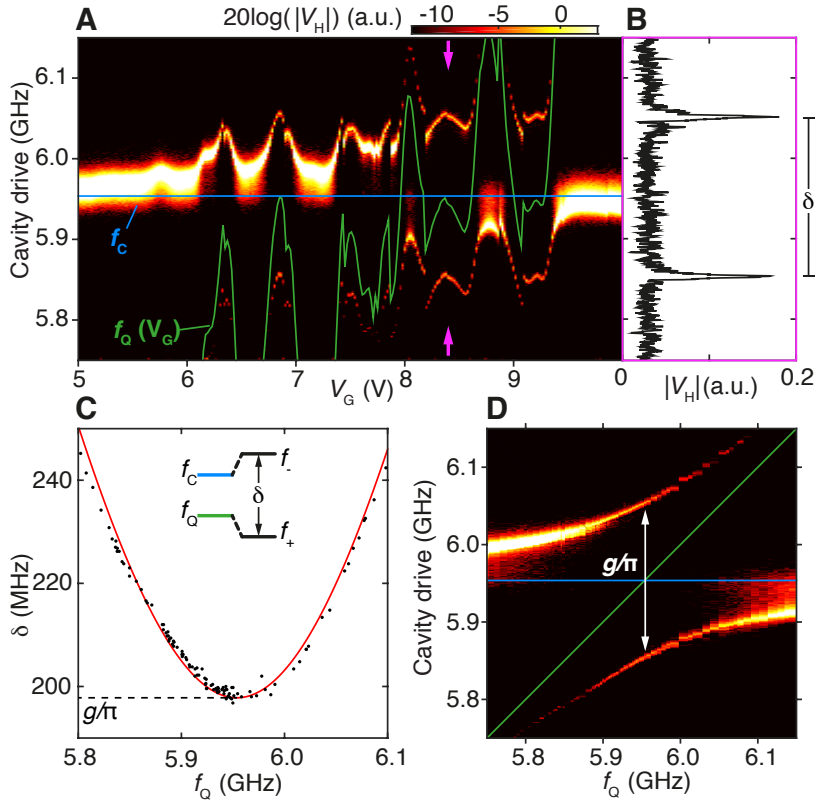

Figure 5.2: **A** Hybridization of the microwave cavity and gatemon qubit. Extracted qubit frequency and cavity frequency shown as green and blue lines respectively. **B** Line cut of A indicated by purple arrows. Clearly separated peaks in the transmission. **C** The vacuum Rabi splitting as a function of extracted qubit frequency. **D** Parametric plot of the vacuum Rabi splitting as a function of extracted qubit frequency reveals the expected anticrossing of two hybridized states.

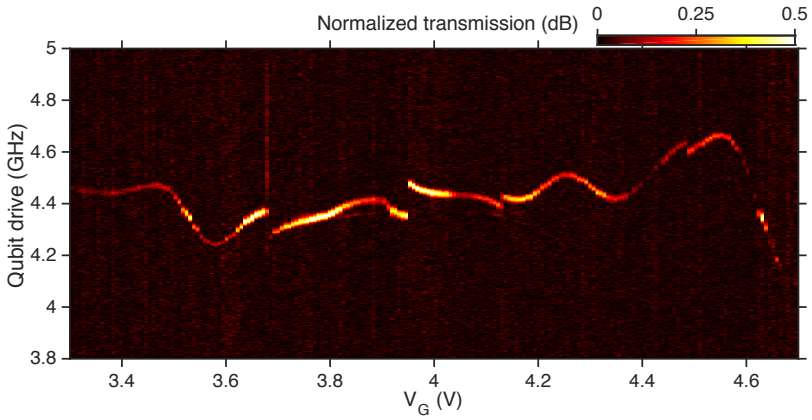

Figure 5.3: Spectroscopy measurements of the qubit frequency as a function of gate voltage. Each column is normalized by the value at 3.8 GHz.

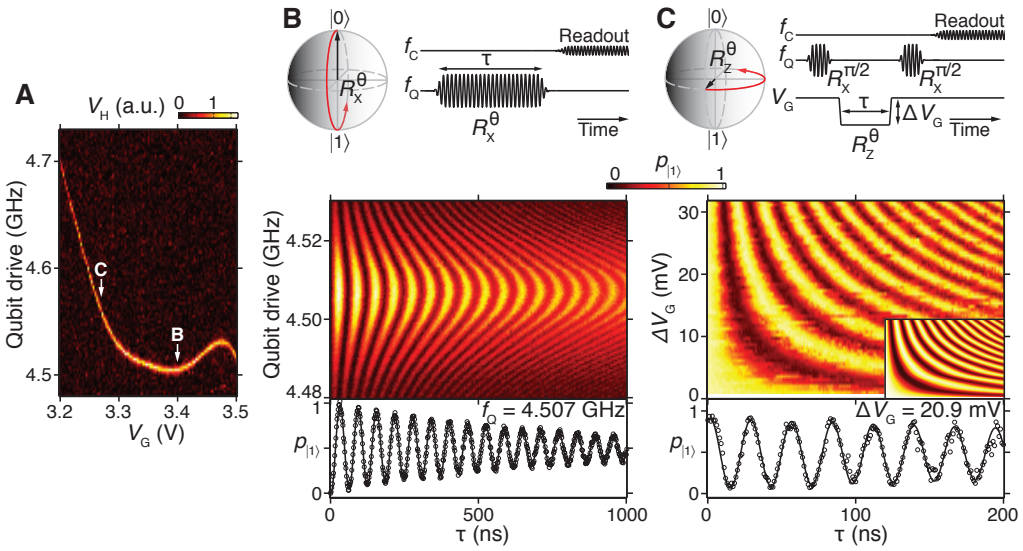

Figure 5.4: **A** Spectroscopy of the gatemon. **B** Upper panel shows the pulse sequence for qubit rotations around the X axis on the Bloch sphere. Main panel shows Rabi oscillations as a function of drive time τ and qubit drive frequency. Lower panel is a line cut at the qubit frequency. **C** The pulse sequence for Z rotations is shown in the upper panel. Main panel shows rotations as a function of drive time τ and gate pulse amplitude. Lower panel is a line cut at pulse amplitude $\Delta V_{\mathrm{G}} = 20.9$ mV. Normalized state probability, $p_{|1\rangle}$, is calculated from the demodulated cavity response, V_H, by fitting Rabi oscillations to an exponentially damped sinusoid of the form $V_H^0 + \Delta V_H \exp(-\tau/T_{\mathrm{Rabi}}) \sin(\omega\tau + \phi)$ to give $p_{|1\rangle} = (V_H - V_H^0)/2\Delta V_H + 1/2$. The solid curves in lower panels of A and B are exponentially damped sinusoids.

qubit operations it is convenient to have fast control of the qubit frequency to perform two-qubit operations. To show that the gatemon allows fast adiabatic pulses of the qubit frequency we measure the effect on a single qubit. Changing the qubit frequency effectively induces Z rotations on the Bloch sphere. The qubit response is simplified by placing the gate voltage at 3.27 V (indicated by C in Figure 5.4**A**) where the qubit frequency depends linearly on the gate voltage. This ensures that the rotations induced by the change in frequency depend linearly on the gate voltage. To observe rotations about the Z axis, we first rotate the qubit by $\pi/2$ to the equator of the Bloch sphere as shown in the upper panel of Figure 5.4**C**. Then a gate pulse of length τ induces a rotation around the Z axis with a frequency proportional to the pulse amplitude (due to the linear energy spectrum). A final $\pi/2$-pulse allows effective readout along the Y axis of the Bloch sphere. In the main panel we see the rotations that depend on the length of the pulse and the amplitude of the voltage pulse on the gate demonstrating coherent voltage-pulse operations. Furthermore, these operations demonstrate the stability of the gatemon as the data in the main panel of Figure 5.4**B** were collected over several hours.

In Figure 5.5 coherence measurements of two gatemon qubits are shown. The pulse schemes for measuring the lifetime T_1 and dephasing time T_2^* are shown in black and blue respectively. Lifetime is measured by varying the delay time between a π pulse, which rotates the qubit to the $|1\rangle$ state, and readout. The expected exponential decay with a characteristic time T_1 of the $|1\rangle$ state probability is observed. We extract lifetimes 0.56 μs and 0.83 μs for sample 1 and 2 respectively.

The dephasing time is measured by placing the qubit on the equator with a slightly detuned $\pi/2$ pulse so that the qubit state precesses around the equator. Readout is done after a delay time τ and a second $\pi/2$ pulse to rotate the Y axis onto the Z axis for readout. We observe the precession of the qubit as the oscillation while the exponential decay with a characteristic time scale T_2^* is due to decoherence. Lifetime enforces an upper limit on the decoherence time of $T_2^* \leq 2T_1$ as the qubit can decay from the superposition state on the equator. For Sample 1 we find $T_2^* = 0.97$ μs very close to the lifetime limit. Sample 2 performs slightly worse with $T_2^* = 0.71$ μs. For drifts in the qubit frequency that are constant within the time of the pulse sequence one can cancel the effect by performing an echo pulse as indicated in red. The pulse effectively reverses the sign on the noise such that noise picked up before the echo pulses is cancelled by noise after the pulse. High frequency noise switching faster than the sequence length will not get cancelled by an echo pulse. More elaborate pulse schemes can be used to avoid specific parts of the noise spectrum in the system [120]. We can increase the decoherence time of qubit 2 to $T_{\text{Echo}} = 0.95$ μs with an echo pulse. The fact that we do not reach the lifetime limit indicates that qubit 2 suffers from some high frequency noise.

Lifetime and coherence times in this first generation of devices is primarily limited by materials loss in the capacitors. Especially a $\sim$ 87 nm thick thermal oxide layer on the silicon substrate leads to losses in capacitors. The oxide layer is initially included to ensure electrical separation between the gate electrodes and the surrounding ground plane. Subsequent studies reveal that a certain distance between contacts and gate electrodes sufficiently insulates the electrodes (for ~ 1 μm substrate leakage happens at

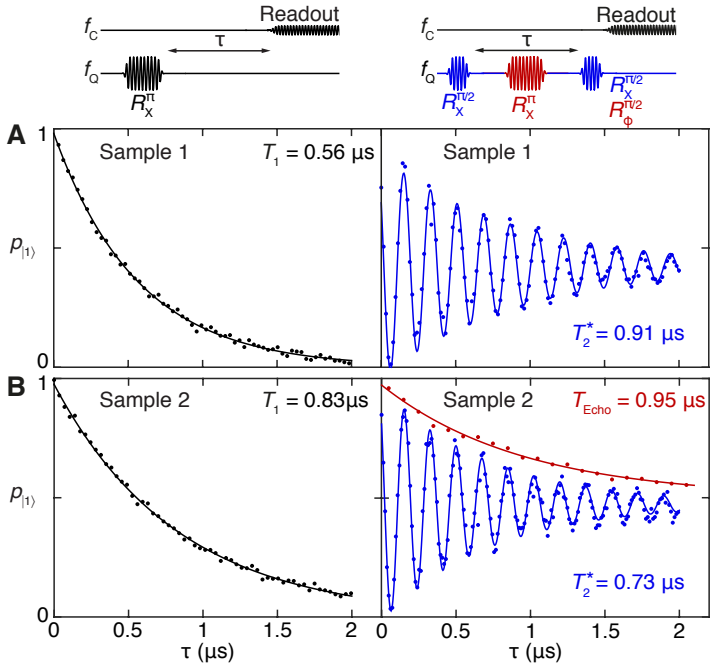

Figure 5.5: **A** Left shows lifetime measurement of sample 1 at point B in Figure 5.4**A** ($V_G = 3.4$ V). Left side in upper panel shows the pulse scheme for lifetime measurements. A 30 ns π pulse rotates the qubit to the $|1\rangle$ state and a wait time τ before readout is varied. Solid curve is an exponential fit. Right side shows a Ramsey experiment performed by varying a wait time τ between two slightly detuned 15 ns $\pi/2$ pulses. Solid curve is an exponentially damped sinusoid from which we determine T_2^*. **B** Lifetime and Ramsey experiments are repeated for sample 2 which has $f_Q = 4.426$ GHz ($V_G = -11.3$ V). Furthermore we perform a Hahn echo experiment in red with a π pulse inserted between two $\pi/2$ pulses with a varying wait time τ. The phase of the second $\pi/2$ pulse is varied to fit an exponential decay to the extracted amplitude.

$\sim \pm 10$ V on gates) allowing for removal of the global thermal oxide. This combined with careful optimization of capacitor loss in resonator Q-factor measurements lead to almost tenfold increase in lifetime for second generation [118] of gatemons. Recent studies has shown coherence times of gatemons approaching that of state-of-the-art transmon qubits [113] demonstrating the feasibility for quantum-error correction with gatemon qubits.

5.2 Gatemon Benchmarking and Two-Qubit Operations

For quantum computations based on gatemons we want to quantify the fidelity of qubit gates including two-qubit gates. To demonstrate two-qubit gates the second generation is designed with two capacitively coupled gatemons [32]. Additionally, several improvements are made in the design layout [Figure 5.6] and fabrication. Separate qubit drive lines labelled 'XY control' for individual qubit control, separate $\lambda/4$ readout cavities with resonance frequencies $f_{C1} = 7.81$ GHz and $f_{C2} = 7.73$ GHz coupled to the same feedline for frequency-multiplexed readout, low loss substrate for reduced capacitor loss, and control circuitry with added crossovers to reduce spurious modes in the ground plane [110]. The qubit parameters differ only slightly from the first generation of gatemons with simulated values of charging energy $E_C/h = 230$ MHz and qubit-cavity coupling $g/2\pi \approx 100$ MHz. Electrostatic simulations predict a qubit-qubit coupling strength $J \sim 20$ MHz.

With the improvements we measure almost tenfold improvements for qubit lifetimes up to $T_1 \sim 5$ μs and decoherence times $T_2^* \sim 4$ μs, which can with a single refocusing pulse be increased to $T_{\text{Echo}} \sim 9.5$ μs almost at the limit of $2T_1$. Next we quantify the fidelity of qubit operations with randomized benchmarking. We expect microwave induced gates to have the same performance as other transmons as the capacitive coupling to the system is independent of the Josephson junction. However, Z and $Z/2$ gates can be induced by baseband pulsing of the junction gate changing $E_{\text{J}}(V_G)$. We want to verify high fidelity of microwave induced gates and test the fidelity of qubit gates induced by voltage pulses.

Complete information of a qubit operation can be measured with quantum process tomography [121], which describes how any input qubit state is processed by the qubit operation to a qubit output state. However, each process matrix for just a single qubit operation requires measuring 12 independent numbers with high precission[1] [122]! Evidently it is not practical to fully characterize a set of quantum operations due to time-constraints. Rather we need a procedure that faithfully estimates the fidelity of gates in an efficient manner.

For this purpose randomized benchmarking [123] has been adopted as a standard for quantifying error rates of Clifford gates. Randomized benchmarking is done by measuring the fidelity of a sequence of m random Clifford gates composing the identity operation. From the decay of the fidelity of random sequences composing the identity operation as

[1] It is especially difficult to separate the qubit operation fidelity from errors in initialization and measurements.

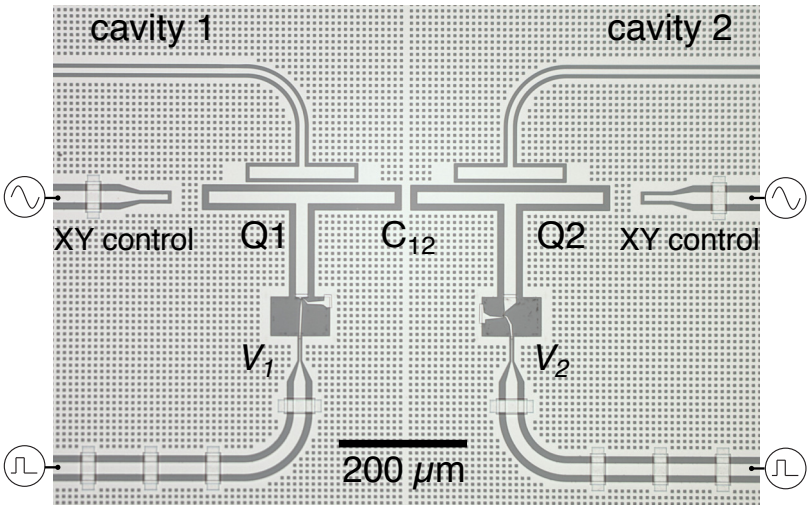

Figure 5.6: Optical image of a two qubit gatemon device. The two qubits are coupled to individual $\lambda/4$ cavities. Coherent operations are performed by drive lines coupled capacitively to the gatemons.

a function of m one can extract an average error rate of all Clifford gates. Furthermore, interleaved randomized benchmarking, which interleaves a specific Clifford gate between each random gate of a sequence, allows measurement of error probability of individual gates. Random Clifford gates will randomize the qubit state throughout the sequence effectively mapping any noise onto the depolarization channel. The depolarization channel is fully described by a single probability, $1-p$, that the qubit state is replaced with fully mixed state [39]. The decay rate of fidelity is given by p^m (the probability that the qubit has not been replaced by a mixed state after m operations) and the average gate error is $r = (1-p)/2$.[2] Importantly as the measurement relies of the decay rate of fidelity it becomes independent of errors in state preparation and measurement (SPAM errors).

Figure 5.7 shows data from interleaved randomized benchmarking on Q2. First a reference of non-interleaved randomized benchmarking is performed using only microwave induced pulses. Black diamonds is the fidelity of pulse sequences comprising m random Clifford gates, C, followed by a recovery pulse, C_R, such that $C_R(C)^m = I$. As the full sequence composes the identity the fidelity can be measured as the $|0\rangle$-state population. Each Clifford gate is generated by one or more Gaussian shaped microwave pulses with standard deviation $\sigma = 7$ ns and truncated to a full gate time of $t_g = 28$ ns. These pulses were optimized using AllXY pulse sequences [106] and randomized benchmarking sequences [108]. The fidelity decays is fitted to $Ap_{\text{ref}}^m + B$ with $A = 0.53$ and $B = 0.42$ accounting for SPAM errors. From $p_{\text{ref}} = 0.981$ we extract an average single-qubit error rate of $r_{\text{ref}} = (1-p_{\text{ref}})/(2 \times 1.875) = 0.5 \pm 0.07$ %, where the factor 1.875 is the average number of single qubit gates per Clifford gate.

For interleaved randomized benchmarking of gate G we measure the fidelity of pulse

[2]The factor 2 originates from the fact that a fully mixed state can only be in two states when measured: one where an error occurred and one where no error occurred. So half the time no error happened even if the qubit was replaced by a mixed state.

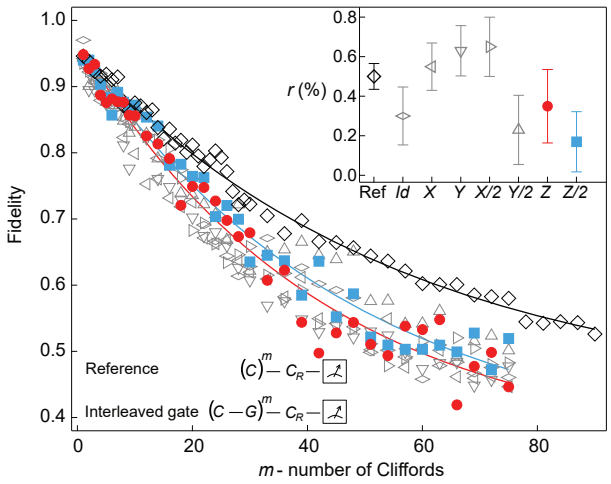

Figure 5.7: Randomized benchmarking of single-qubit Clifford gates on Q2. Black shows reference of randomized benchmarking of Clifford gates yielding an error rate of $r = 0.5 \pm 0.07$ %. Interleaved randomized benchmarking of individual gates reveals no discrepancy between microwave induced gates (gray) and baseband pulsing of gate voltage V_{G2} (blue and red). Inset shows extracted error rates from each interleaved gate.

sequences comprising of $C_R(GC)^m = I$, where C again is random Clifford gates and C_R is the recovery pulse such that the total sequence composes identity. Measuring the decay of fidelity as a function of m we again fit the decay to $Ap_G^m + B$ and extract p_G for each gate tested. From p_g and p_{ref} the average gate error for gate G is given by $r_g = (1 - p_G/p_{\text{ref}})/2$. Inset in Figure 5.7 displays the error rates of individual gates. Qubit gates induced by voltage pulses, Z and $Z/2$, are performed by a 28 ns square pulse and reaches error rates of $r_Z = 0.35 \pm 0.19\%$ and $r_{Z/2} = 0.18 \pm 0.15\%$ consistent with the lifetime limit on gate error: $r_{\text{limit}} = t_g/3T_1 = 0.3\%$ [124], where $T_1 = 3.1$ μs at the measurement point. This clearly demonstrates that high fidelity gates can be performed with gate voltage pulses in gatemon qubits.

Next we investigate coherent two-qubit operations. The qubit-qubit coupling is observed in two-spectroscopy as an avoided crossing as the Q1 is swept through resonance with Q2 [Figure 5.8**A**]. To demonstrate that we have coherent control of the two-qubit system we perform iSWAP operations. The applied pulse sequence is shown in 5.8**B**. With the qubits initially off-resonance a single π pulse excites Q2 to the $|1\rangle$ state while Q1 is left in the ground state. A gate voltage pulse with amplitude ΔV_2 on Q2 brings the qubits diabatically into resonance for a time τ before bringing the system back for readout. The excitation initially on Q2 begins to oscillate between the hybridized qubits with a frequency J/π. The $|1\rangle$ state probability in Q1 after an iSWAP operation is mapped out as a function of waiting time τ and pulse amplitude ΔV_2 in Figure 5.8**C**. A chevron pattern is observed as the excitation coherently swaps between Q1 and Q2. A similar plot is obtained for measurements of the $|1\rangle$ state probability of Q2 which is inverted compared to 5.8**C**. In 5.8**D** a line trace of both measurements is shown demonstrating the excitation swapping between the two qubits. From the oscillations we extract a coupling

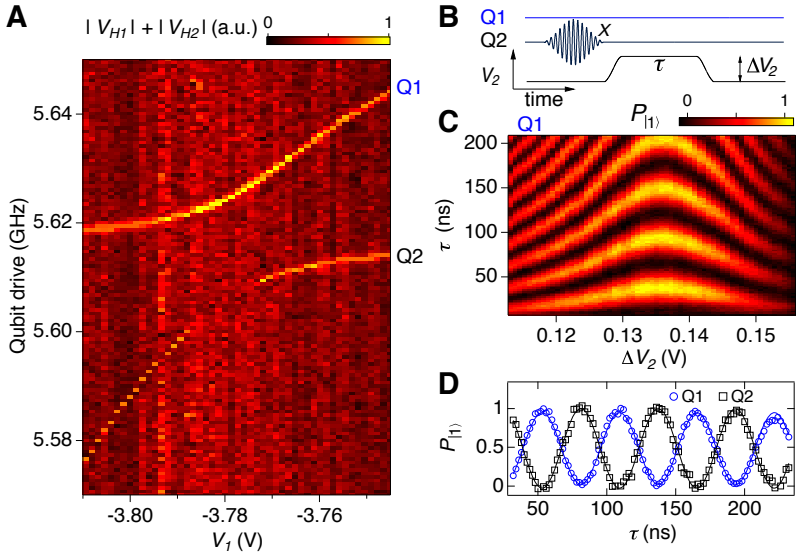

Figure 5.8: **A** An avoided crossing is observed in spectroscopy measurements as the frequency of Q1 is being swept through the frequency of Q2. **B** Pulse sequence for mapping the qubit-qubit coupling in time domain. Q2 is excited by a π pulse followed by a gate pulse with amplitude ΔV_2 and width τ. **C** Swap oscillations as a function of ΔV_2 and width τ. **D** Line cut of **C** with the gate pulse bringing the qubits into resonance for time τ.

strength of 17.8 MHz.

The preferred two-qubit gate for quantum algorithms is a controlled phase gate c_Z^π gate presented in section 3.5. To demonstrate the effect of the gate Q1 is used as control qubit in either state $|0\rangle$ or $|1\rangle$ shown in blue and red respectively in Figure 5.9**A**. First Q2 is placed on the equator of the Bloch sphere by a $X/2$ pulse to detect rotations around the Z axis. Then a voltage pulse on Q2 brings the system close to the $|20\rangle - |11\rangle$ anticrossing acquiring a phase shift conditional on the state of Q1. Lastly, the acquired phase is measured by varying the angle of a $\pi/2$ pulse before readout. The pulse sequence is adjusted such that the dynamical phase acquired by Q2 due to the change in frequency is a multiple of 2π. Performing the sequence with the control qubit in $|0\rangle$ and $|1\rangle$ we find the conditional phase difference. Figure 5.9**B** shows the π phase dependence of the control qubit as desired for the c_Z^π gate.

To estimate the gate fidelity we perform interleaved single-qubit randomized benchmarking treating the c_Z^π gate as a single qubit Z gate as shown in 5.9**C**. The resulting gate fidelity of c_Z^π with the state of the control qubit randomized between $|0\rangle$ and $|1\rangle$ is $r = 9 \pm 2$ % [Figure 5.9**D**]. Fixing the state of the control qubit leads to similar gate fidelities as shown in the figure inset. We estimate a 4 % error rate due to qubit relaxation and attribute the remaining 5 percentage points to leakage into state $|20\rangle$.

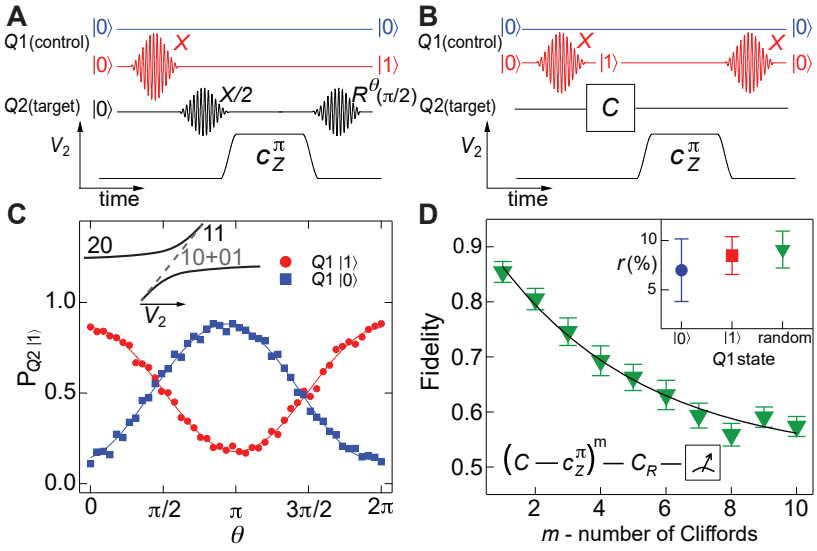

Figure 5.9: **A** Pulse sequence to probe phase shift of controlled phase gate c_Z^{π}. Control qubit is placed in either state $|0\rangle$ or $|1\rangle$ shown in blue and red respectively. To observe a phase shift on target qubit Q2 it is placed on the equator by a $X/2$ pulse before the c_Z^{π} gate is performed. Lastly a $\pi/2$ gate along an axis whose phase θ is varied. **B** Probability of Q2 in state $|1\rangle$ as a function of θ. **C** Pulse scheme for interleaved randomized benchmarking of the controlled phase gate c_Z^{π}. **D** Fidelity of interleaved, single-qubit randomized benchmarking. Inset shows extract gate errors dependent on the state of the control qubit.

5.3 Conclusion

In conclusion we have demonstrated a novel semiconductor-based superconducting qubit based on a field effect tunable Josephson junction. Universal single-qubit control is achieved with all-microwave control and with randomized benchmarking we measure 99.5 % average fidelity for Clifford gates limited by qubit coherence times. Crucially, nanosecond voltage pulses on the field effect tunable Josephson junction induces qubit frequency modulation without degradation in qubit coherence. This allows implementation of controlled-phase, two-qubit operations forming a sufficient gate set for quantum error correction.

Gatemon qubits offer an alternative all-electrical approach to tunable superconducting qubits alleviating the need for milliampere currents required for conventional flux controlled superconducting qubits. Recent work has demonstrated the feasibility of top-down wafer-scale fabrication of gatemon qubits based on proximitized two-dimensional electron gas paving the way for readily scalable gatemon circuits [76]. Furthermore, state-of-the-art gatemon qubits have demonstrated coherence times approaching that of conventional $Al/AlO_x/Al$ tunnel junctions [113] putting gatemon qubits in the range of quantum error correcting. Additionally, field effect tunable Josephson junction presents a new circuit element that might enable novel circuits such as tunable couplers [38, 125].

Chapter 6

A Superconducting 0-π Qubit Based on High Transmission Josephson Junctions

Topological protection can be engineered at the device level by designing a Hamiltonian performing passive quantum error correction. Such a Hamiltonian is described by multiqubit terms given by the stabilizers of the error correcting code being implemented. In this Chapter we experimentally investigate a 0-π qubit, which is a fundamental building block for topologically protected qubit [29, 126] with protected quantum operations [127]. The basis of the 0-π qubit are two degenerate ground states required to have no error-prone single-qubit terms in the designed Hamiltonian. It can be realized utilizing a superconducting circuit element with a π-periodic double-well potential in the superconducting phase difference, φ.

Recent experimental studies have realized circuit elements generating $\cos(2\varphi)$ potentials [35, 36] in rhombi structures through interference effects between four equally sized aluminium tunnel junctions [128]. However, fabrication variations in the size AlOx-based Josephson junction elements lift the degeneracy of the lowest two states, limiting the qubit protection in this circuit. We present a simplified design for this fundamental $\cos(2\varphi)$ building block using hybrid, high transmission superconductor-semiconductor Josephson junctions. Our approach takes advantage of the non-cosine energy-phase relation and *in situ* voltage tunability to precisely define a 0-π qubit circuit.

The circuit for the semiconductor-based 0-π qubit is shown in Figure 6.1(a). The transmonlike geometry consists of a superconducting island with charging energy, E_C, that is connected to ground through two high transmission Josephson junctions arranged in a superconducting quantum interference device (SQUID) configuration. Each junction is controlled using the gate voltage V_k ($k \in \{1, 2\}$). We model the Josephson junctions using short junction theory where the Josephson effect is characterized by a set of transmission coefficients of transport channels in the normal section, $\mathcal{T}^{(k)} = \{\tau_i^{(k)}\}$ [129].

The energy-phase relation of the junction is then given by summing over the energies

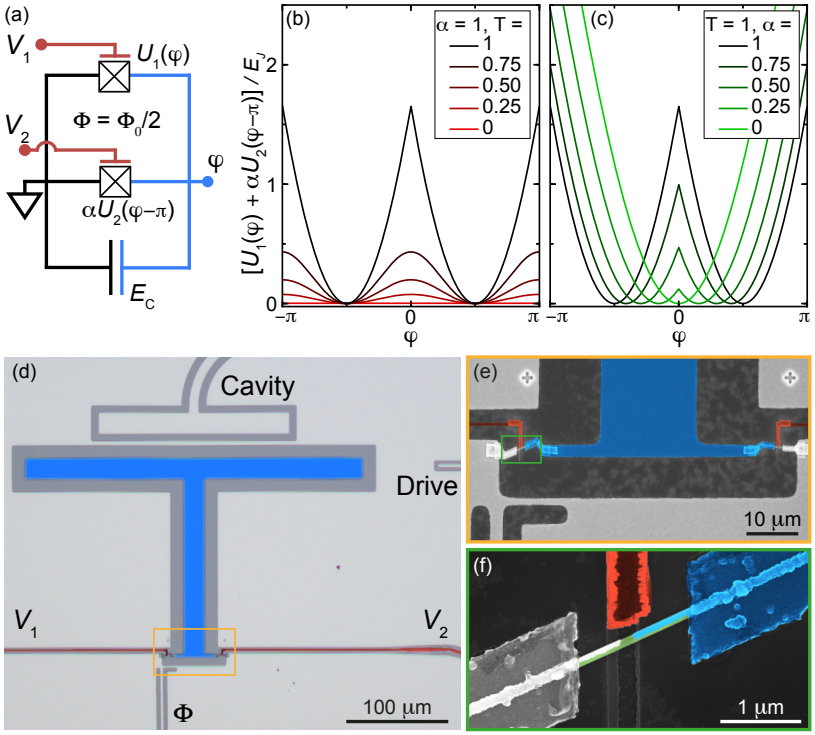

Figure 6.1: The 0-π qubit. (a) Circuit schematic of the 0-π qubit formed by high transparency, semiconductor Josephson junctions in a SQUID shunted by a large capacitor. (b-c) Energy-phase relation of the SQUID for different transmission coefficients (b) and different loop asymmetries (c). (d) False color optical image of the large island (blue) forming one side of the shunting capacitor. (e-f) False color scanning electron micrographs. (f) A small segment of the Al shell on a InAs nanowire is etched away to form a semiconductor Josephson junction. A nearby electrostatic gate (red) allows tuning of the electron density in the junction.

of each channel,

$$U_k(\varphi_k) = -\Delta \sum_{\tau \in \mathcal{T}^{(k)}} \sqrt{1 - \tau \sin^2(\varphi_k/2)}, \tag{6.1}$$

where Δ is the superconducting gap and φ_k is the superconducting phase difference across the JJ. The total system Hamiltonian is given by,

$$H = 4E_C\hat{n}^2 - U_1(\hat{\varphi}) - U_2(\hat{\varphi} - 2\pi\Phi/\Phi_0), \tag{6.2}$$

where Φ is the applied flux through the SQUID loop and $\Phi_0 = h/2e$ is the superconducting flux quantum. For identical junctions at one-half flux quantum, $\Phi = \Phi_0/2$, odd harmonics in the Hamiltonian potential, $-U_1(\hat{\varphi}) - U_2(\hat{\varphi} - 2\pi\Phi/\Phi_0)$, are suppressed, leaving even harmonics of the potential. Figure 6.1(b) shows the even harmonics of the potential, present in high transmission junction with a dominant $\cos(2\hat{\varphi})$ term, forming the characteristic π-periodic potential of a 0-π qubit with degenerate ground states. In charge basis the degeneracy originates from the Josephson current across the SQUID occurring only in units of $4e$ charge, that is, pairs of Cooper pairs. The suppression of single Cooper pair transport results in the qubit having doubly degenerate ground states that differ by the parity of Cooper pairs on the island. The height of the potential barriers separating the two wells scales with the symmetry, α, of the SQUID loop as it originates from an interference between the two junctions. Breaking the symmetry by reducing the transmission through one of the junctions, shown in Figure 6.1(c), will lower one barrier and raise the other, recovering the single-well potential of a transmon in the limit $\alpha \to 0$. In the intermediate regime the potential resembles that of a flux qubit. Related work with nanowire SQUID transmons have shown double well potentials [74].

The measured device is shown in Figure 6.1(d-f). A large T-shaped island (blue) embedded in a 100 nm thin aluminium ground plane forms the shunting capacitor of the superconducting circuit. The sample is fabricated on a high-resistive silicon substrate. From simulations we estimate the charging energy of the capacitor to be $E_C \sim 235$ MHz. Two InAs nanowires grown by molecular beam epitaxy with a ~ 10 nm thick epitaxial aluminium shell on two facets are placed in between the island and the ground plane and contacted using a light argon mill. Semiconductor Josephson junctions are formed by etching away a small segment of the aluminium shell on the nanowire. Nearby electrostatic gates (red) tune the electron density and hence the transmission of conduction channels in the Josephson junctions. By applying a current to a transmission line shorted to the ground plane near the SQUID a small magnetic field is generated allowing control of the flux, Φ, penetrating the loop. The island is capacitively coupled to a $\lambda/4$ cavity with coupling strength $g/2\pi \sim 80$ MHz in the transmon regime. The system is driven with microwave excitations applied to a nearby open transmission line. The sample is loaded in an Al box placed inside a magnetic shield and measured in a dilution refrigerator at < 50 mK [Details in C.3].

In Figure 6.2(a) we first probe the resonance frequency of the $\lambda/4$ cavity as a function of flux, Φ, through the SQUID. Near half a flux quantum a vacuum-Rabi splitting is visible as the cavity state hybridize with a qubit state (red line). Several additional

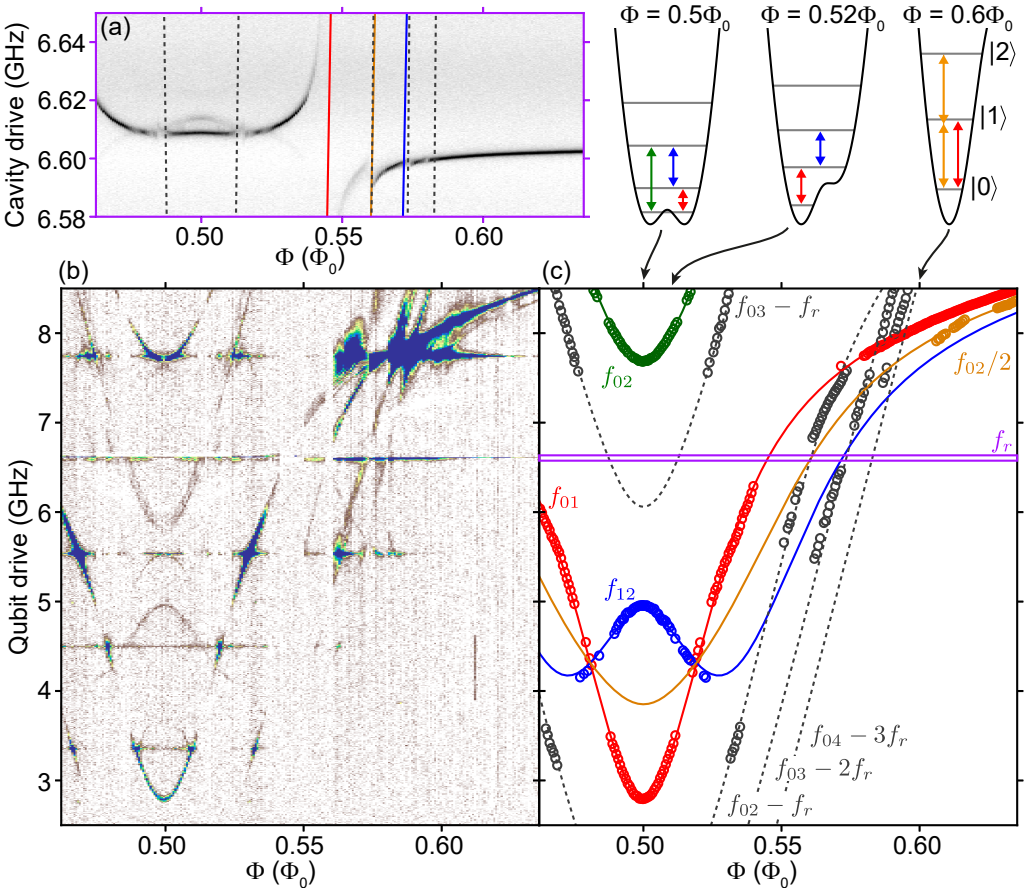

Figure 6.2: Qubit spectroscopy as a function of flux, Φ, at voltages $V_1 = 1.4$ V and $V_2 = -0.445$ V. (a) Resonance frequency of the readout cavity as the qubit energy is modified by flux. Solid and dotted lines are from fit to data in (c). (b) Two-tone spectroscopy of the qubit transition frequencies. An average of each collumn has been subtracted. (c) Extracted transition frequencies from (b) with solid lines the results of a fit to Eqn. (6.2). Cartoons above shows the fitted potential at different values of Φ. Gray dotted lines are multi-photon transitions due to simultaneous readout and drive tones.

qubit states weakly couple to the cavity giving rise to smaller anticrossings. Utilizing two-tone spectroscopy in Figure 6.2(b) we can directly probe the transition frequencies of the qubit system. A readout tone, adjusted at each point in flux to the cavity frequency extracted from Figure 6.2(a), is monitored while a second drive tone is swept in frequency to excite energy states.

At $\Phi = 0.63\ \Phi_0$, away from half a flux quantum, we observe two transition frequencies near 8.4 GHz closely resembling the spectrum of a transmon qubit with the higher frequency transition being f_{01} (red) and the lower a 2-photon excitation $f_{02}/2$ (blue). As the flux is tuned closer to half a flux quantum the frequency of f_{01} sharply drops, diverging from a transmon system with the anharmonicity changing from negative to positive. Several horizontal lines are observed in the spectrum, which we interpret as on-chip resonances, amplifying the readout response as a transition frequency crosses.

To understand the spectrum we extract excitation frequencies of f_{01}, f_{02}, $f_{02}/2$, and f_{12} shown as circles in Figure 6.2(c). The extracted resonance frequencies are fitted by nummerically calculating energy eigenstates of Eqn. (6.2) with $\Delta/h = 45$ GHz [78] (details given in Section 6.1). The results are plotted as solid lines in Figure 6.2(c). From the fit we extract charging energy $E_C = 280$ MHz and sets of transmission coefficients for each junction $\mathcal{T}^{(1)} = \{1, 1, 0.553, 0\}$ and $\mathcal{T}^{(2)} = \{0.945, 0.14, 0.14\}$. Cartoons above Figure 6.2(c) plot the Josephson potential of the SQUID at different values of Φ. At $\Phi = 0.5\ \Phi_0$ the potential is a symmetric double well potential due to the high transmission of the nanowire Josephson junction. Moving away from $\Phi = 0.5\ \Phi_0$ the potential is tilted causing f_{01} to sharply rise in energy. Further tilting the potential results in a single well and the transmon spectrum of a weakly anharmonic oscillator is recovered.

We can match other transitions (gray lines) to multi-photon excitations due to simultaneous readout and drive tones. These transition frequencies are calculated by subtracting an integer number of the cavity resonance frequency, f_r, from the fitted spectrum. Small differences between model and data might be explained by small modifications to the measured resonance frequency due to the AC Stark shift of transition frequencies.

Next we study the effect of tuning the gate voltages for each nanowire Josephson junction. As highlighted in Figure 6.1(c), the relative size of the two Josephson junctions can strongly modify the qubit potential. First we tune the gate voltages so that the two junctions are of similar coupling strength to form a double-well potential [Figure 6.3(a)]. A single transition frequency is present in the spectrum with two smaller anticrossings at $\Phi \sim 0.48\ \Phi_0$ and $0.52\ \Phi_0$. At these points in flux the potential is tilted such that the lowest energy state of one well is on resonance with the first excited state of the other well causing an anticrossing between f_{01} and f_{02}. At flux points closer to $\Phi = \Phi_0/2$ the visible transition near 8 GHz is a single excitation within the same well exciting the $|2\rangle$-state of the full system. Microwave-induced transitions between wells are suppressed due to missing overlap of eigenstates in separate wells. The spectrum of the 0-π qubit is reminiscent to that of a recently studied heavy fluxonium [130, 131].

Using the measured transition frequencies, $E_C = 295$ MHz, and $\Delta = 45$ GHz we extract the transmission coefficients $\mathcal{T}^{(1)} = \{1, 1, 0.605, 0\}$ and $\mathcal{T}^{(2)} = \{0.991, 0.758, 0.574, 0.011\}$. At $\Phi = \Phi_0/2$ the potential forms a double well potential with minima at $\pm\pi/2$ with two

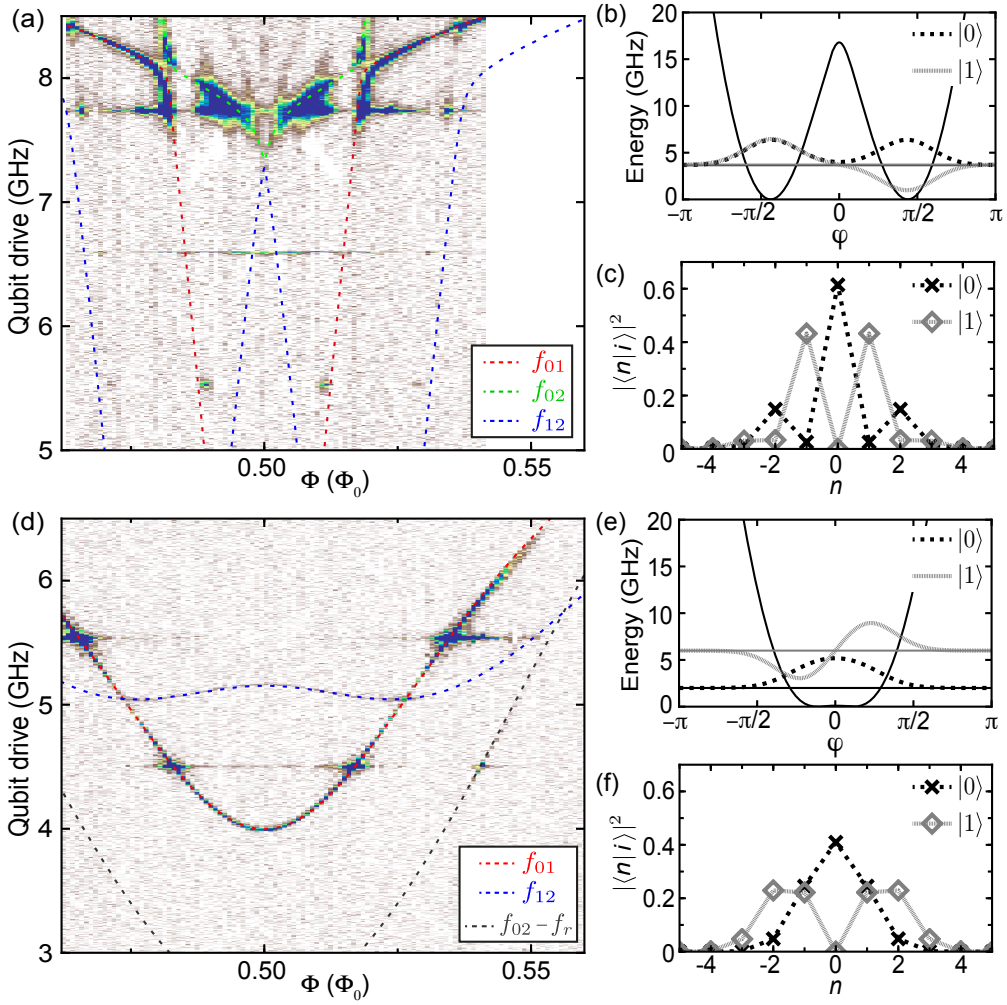

Figure 6.3: Voltage control of middle barrier. (a) Gate voltages tuned towards a balanced regime with the two junction of similar coupling strength, $V_1 = 1.2$ V and $V_2 = -0.12$ V. (b) Qubit potential and wave functions two lowest energy states extracted from fit to data in (a) at $\Phi = \Phi_0/2$. (c) The charge distribution of the two lowest energy states. (d) Gate voltages tuned towards an unbalanced regime with one junction much smaller than the other, $V_1 = 1.241$ V and $V_2 = -0.386$ V. (e,f) Potential and wavefunctions of two lowest energy states extracted from fits to (d).

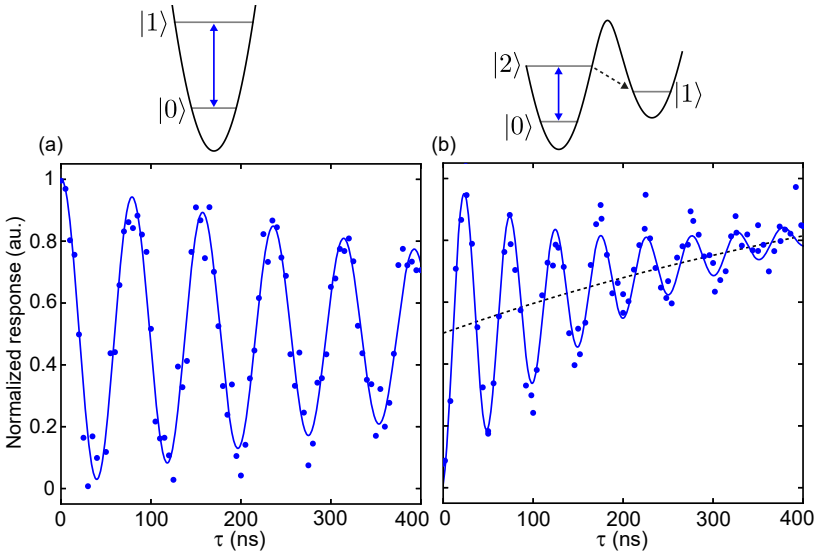

Figure 6.4: Coherent control. Rabi oscillations in (a) the transmon regime with $\Phi = 0$ and $f_{\text{Drive}} = 7.911$ GHz and (b) a tilted 0-π qubit regime with $\Phi = 0.512\ \Phi_0$ and $f_{\text{Drive}} = 5.725$ GHz. Cartoons show the qubit potentials with lowest energy states with voltages fixed at $V_1 = -1.25$ V and $V_2 = -0.445$ V. Solid line in (a) is a fit to an exponentially decaying sinusoidal function. In (b) the fit function has an additional exponentially decaying offset (dashed line).

nearly degenerate ground states given by the bonding and anti-bonding eigenstates of the potential [Figure 6.3(b)]. In Figure 6.3(c) the two ground states are plotted in charge basis clearly visualizing the two states as even or odd numbers of Cooper pairs.

We now tune the gate voltage such that one junction much smaller than the other. Figure 6.3(d) shows the qubit spectrum as a function of Φ. Again we fit the energy spectrum to Eqn. (6.2) and find $\mathcal{T}^{(1)} = \{1, 1, 0.308, 0308\}$ and $\mathcal{T}^{(2)} = \{0.891, 0.112, 0.112\}$. Modeling the potential and two lowest energy states [Figure 6.3(e,f)] we find a harmonic oscillator with a small perturbation giving a positive anharmonicity similar to the flux qubit [15]. We hence demonstrate by means of voltage and flux *in situ* tunability between widely different qubit regimes: A transmon, 0-π qubit, and a flux qubit.

The simulations find good agreement with data by varying only the transmission coefficients in each junction giving confidence that the model closely resembles the system. However, we find a discrepancy between the charging energy simulated from electrostatics and from fitting the data given by 235 MHz and 280 MHz respectively. This could be due to the assumption of fixed gap energy, Δ, for all channels in both junctions or other simplifications in the model such as not accounting for charge renormalisation at transmissions near unity [86].

In Figure 6.4 we perform time-domain measurements of the qubit in two different regimes at fixed gate voltages. First we set $\Phi = 0$ such that the qubit is in the transmon regime with a single well potential. Applying a drive tone at the qubit resonance frequency for a time τ we observe Rabi oscillation as expected for a transmon qubit. Next we tune the flux to $\Phi = 0.512\ \Phi_0$ where the qubit potential forms a tilted double

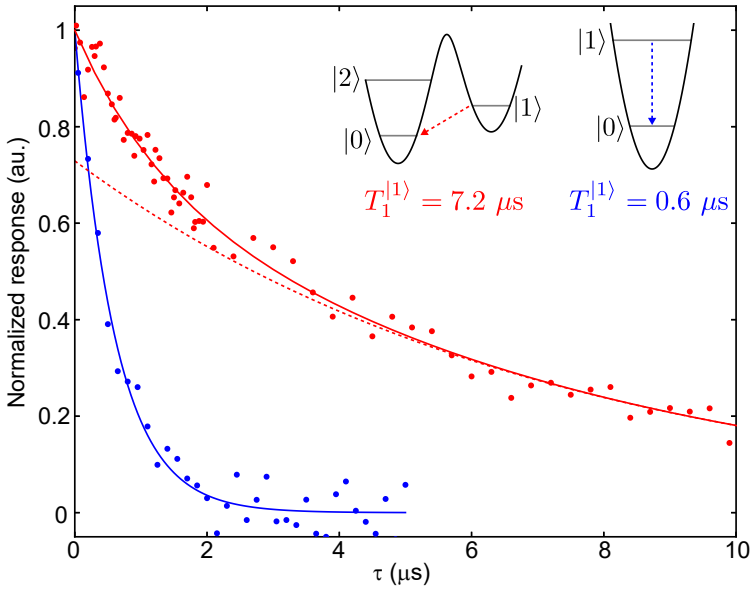

Figure 6.5: Lifetime measurements in a transmon regime with $\Phi = 0$ and $f_{\text{Drive}} = 7.911$ GHz (blue) and a tilted 0-π qubit regime with $\Phi = 0.512\ \Phi_0$ and $f_{\text{Drive}} = 5.725$ GHz (red). Blue solid line is an exponential fit. While red solid is fit to a double exponential $A_1 e^{-\tau/T_1^{|1\rangle}} + A_2 e^{-\tau/T_1^{|2\rangle}}$ with the dashed line showing $A_1 e^{-\tau/T_1^{|1\rangle}}$. Data is normalized to fit parameters.

well shown in Figure 6.4(b). A very weak matrix element between $|0\rangle$ and $|1\rangle$ forbids direct Rabi oscillations to the $|1\rangle$ state. Instead we apply a microwave drive at the $|0\rangle$-$|2\rangle$ resonance frequency. Figure 6.4(b) shows microwave-induced Rabi oscillations between $|0\rangle$ and $|2\rangle$ state. The oscillations appear around an exponentially decaying offset (black dashed line) which we interpret as decay from the $|2\rangle$ state to the $|1\rangle$ state, trapping the population in $|1\rangle$ at long drive times.

To probe the protection offered by the double-well potential we measure the lifetime of the qubit in each regime [Figure 6.5]. In the transmon regime (blue) we measure lifetime by measuring the qubit state after a π-pulse and a wait time τ. We then fit the data to an exponential decay and extract lifetime $T_1 = 0.6\ \mu$s. In the double well regime we cannot perform a direct π-pulse as the $|0\rangle - |1\rangle$ transition is forbidden. Instead we drive $|0\rangle - |2\rangle$ for 3 μs to initialize the state in $|1\rangle$ followed by a measurement delayed by a wait time τ. Due to a small part of the qubit state left in $|2\rangle$ we observe two superimposed exponential decays from which we extract lifetimes $T_1^{|1\rangle} = 7.2\ \mu$s and $T_1^{|2\rangle} = 1.2\ \mu$s.

Enhanced lifetimes in the double-well regime are predicted due to a suppressed charge matrix element $\langle 0|\hat{n}|1\rangle$ [see section 6.1]. From the model we calculate a ratio of 18 between the charge matrix elements in the two regimes. We speculate that lifetime improvement is limited due to other decay channels such as quasipaticles or residual subgap resistance in the nanowire Josephson junctions. In tunnel probe spectroscopy it has been shown that subgap states can be tuned by the electron density of the nanowire [132, 133]. A low electron density might be reached with larger gates tuning the full length of the nanowire

as well as shorter etched Josephson junctions.

Further work on 0-π qubits based on high-transmission nanowire Josephson junctions is needed to develop a robust readout scheme. The present readout scheme based on capacitively coupled resonators cannot distinguish the two ground states in the symmetric double-well regime as each well gives an identical push on the resonator. This can possibly be overcome by parametrically driven readout [134] or by dynamically detuning from the protected regime for readout. Future experiments on 0-π qubits could include coupling to an LC resonator with a superinductance to perform protected qubit rotation [127].

In summary, we have studied a novel superconducting-circuit architecture based on highly transmissive semiconductor-superconductor Josephson junctions allowing *in situ* tunability between widely different qubit regimes. From fits to the qubit spectra we conclude that the semiconductor-nanowire Josephson junctions are dominated by a few conduction channels with transmission coefficients close to unity consistent with recent studies [80]. Our results show that we have engineered a 0-π qubit and in a double-well regime we measure enhanced lifetimes indicating a protected qubit.

6.1 Supplementary Information

Numerical simulation of eigenstates and fitting of energy spectra

This section discusses the numerical simulation of energystates and how the fit is performed.

The model of the system is given by the Hamiltonian:

$$H = 4E_C\hat{n}^2 - \sum_{\tau\in\mathcal{T}^{(1)}} \Delta\sqrt{1-\tau\sin^2(\hat{\varphi}/2)} - \sum_{\tau\in\mathcal{T}^{(2)}} \Delta\sqrt{1-\tau\sin^2[(\hat{\varphi}-\phi)/2]}, \tag{6.3}$$

where $\phi = 2\pi\Phi/\Phi_0$. For numerical simulations of the eigenenergies we first rewrite the Hamiltonian in charge basis by performing a discreet Fourier transform of the energy-phase relation.

$$-\Delta\sum_{i=1}^{N}\sqrt{1-\tau_i\sin^2[(\hat{\varphi}-\phi)/2]} = -\sum_{i=1}^{k} E_k\cos[k(\hat{\varphi}-\phi)] \tag{6.4}$$

$$= -\sum_{i=1}^{k} E_k\frac{e^{ik(\hat{\varphi}-\phi)}+e^{-ik(\hat{\varphi}-\phi)}}{2} \tag{6.5}$$

$$= -\sum_{i=1}^{k} E_k\frac{e^{-ik\phi}|n\rangle\langle n+k| + e^{ik\phi}|n+k\rangle\langle n|}{2}. \tag{6.6}$$

In charge basis the Hamiltonian can be presented as a matrix:

$$H = \begin{bmatrix} \ddots & \vdots & \vdots & \vdots & \vdots & \iddots \\ \cdots & 16E_C & \frac{-E_1^{(1)}-e^{i\phi}E_1^{(2)}}{2} & \frac{-E_2^{(1)}-e^{i2\phi}E_2^{(2)}}{2} & \frac{-E_3^{(1)}-e^{i3\phi}E_3^{(2)}}{2} & \cdots \\ \cdots & \frac{-E_1^{(1)}-e^{-i\phi}E_1^{(2)}}{2} & 4E_C & \frac{-E_1^{(1)}-e^{i\phi}E_1^{(2)}}{2} & \frac{-E_2^{(1)}-e^{i2\phi}E_2^{(2)}}{2} & \cdots \\ \cdots & \frac{-E_2^{(1)}-e^{-i2\phi}E_2^{(2)}}{2} & \frac{-E_1^{(1)}-e^{-i\phi}E_1^{(2)}}{2} & 0 & \frac{-E_1^{(1)}-e^{i\phi}E_1^{(2)}}{2} & \cdots \\ \cdots & \frac{-E_3^{(1)}-e^{-i3\phi}E_3^{(2)}}{2} & \frac{-E_2^{(1)}-e^{-i2\phi}E_2^{(2)}}{2} & \frac{-E_1^{(1)}-e^{-i\phi}E_1^{(2)}}{2} & 4E_C & \cdots \\ \iddots & \vdots & \vdots & \vdots & \vdots & \ddots \end{bmatrix}. \tag{6.7}$$

For numerical simulations we truncate the matrix at $n = \pm 20$ and set off-diagonal entries to zero for $E_k < 1$ MHz. Eigenenergies are found numerically with `numpy.linalg.eig()` for each value of ϕ and transition frequencies are readily calculated as the differences of the sorted set of eigenenergies. Eigenvectors of the matrix are wavefunction of quantum states in charge basis presented in Figure 6.3 of the main text. The wavefunctions in phase basis are calculated from the relation $\psi(\varphi) = \sum_n e^{in\varphi}\psi(n)$.

To fit the data we use `scipy.optimize.least_squares()` to find the sets of transmissions $\mathcal{T}_i^{(1)}$ and $\mathcal{T}_i^{(2)}$ that minimizes the differences between calculated transition frequencies and measured transition frequencies for all measured values of ϕ.

Energy spectrum and matrix elements for Figures 6.4 and 6.5

Figure 6.6 shows spectroscopy data used to extract potentials plotted in Figures 6.4 and 6.5. Figure 6.7 shows calculated charge matrix elements for the fitted model.

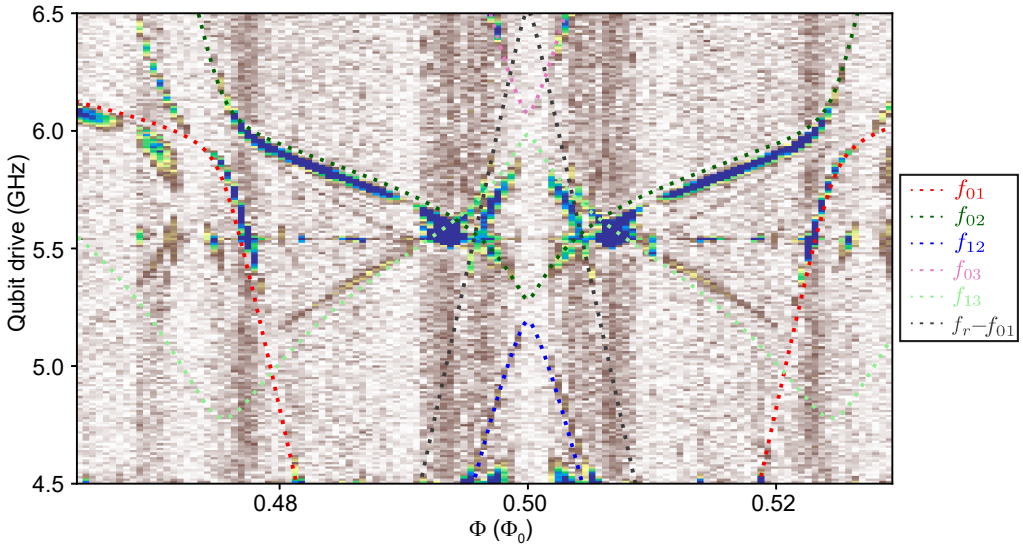

Figure 6.6: Energy spectrum for gate voltages at $V_1 = -1.25$ V and $V_2 = -0.445$ V.

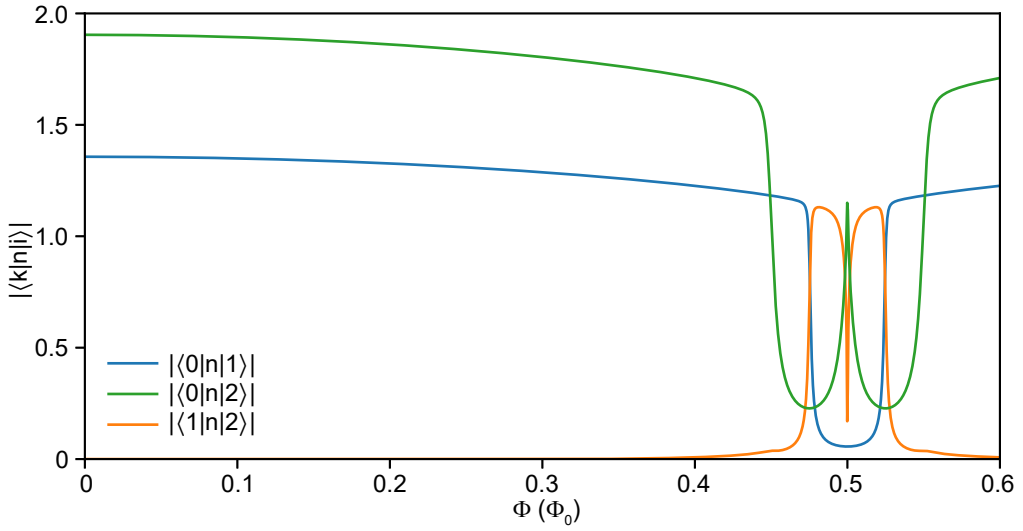

Figure 6.7: Charge matrix elements for gate voltages at $V_1 = -1.25$ V and $V_2 = -0.445$ V.

Chapter 7

High field compatible transmon circuit

Topological materials present an exciting direction to a scalable, topological quantum computer [135, 136]. Recent studies have provided compelling evidence of Majorana fermions in proximitized semiconducting nanowires with strong spin-orbit coupling [21, 22, 137, 138]. A controlled coupling of Majorana fermions, projecting the protected qubit state into a measurable fermion parity, is a corner stone in several Majorana-based qubits [136, 139]. A direct coupling of Majorana fermions on separate superconductors gives rise to a fractional Josephson effect. The fractional Josphson coupling might be detected by embedding it into a well-known transmon circuit [140, 141], which provides well-established measurement techniques. In this Chapter we present a high-field compatible transmon circuit, necessary to enter the topological phase, based on a single superconductor-semiconductor nanowire capable of hosting Majorana fermions. We show that the coherence of the transmon circuit is insensitive to low magnetic fields and survives up to $B = 1$ T sufficient for Majorana fermions.

Transmon qubits exhibits harmonic oscillations in the superconducting phase difference between two superconductors with metastable, uncoupled parity states. Adding the fractional Josephson effect of coupled Majorana fermions to the transmon allows dissipationless, coherent transfer of single electrons coupling the odd and even parity sectors of the transmon. The Hamiltonian of a transmon qubit with a Majorana coupling, a Majorana transmon, is given by [140]:

$$\widehat{H} = 4E_C(\hat{n} - n_g)^2 - E_J \cos(\hat{\varphi}) + 2E_M i\hat{\gamma}_2\hat{\gamma}_3 \cos(\hat{\varphi}/2), \tag{7.1}$$

where E_M is the coupling strength between Majorana fermions $\hat{\gamma}_2$ and $\hat{\gamma}_3$ with a superconducting phase difference φ. The product $\mathcal{P} = i\gamma_2\gamma_3 = \pm 1$ is the fermion parity. Figure 7.1**A** shows the 4π-periodic potential of the Majorana transmon with $E_J > E_M$ and its lowest energy states (not to scale for clarity). Inter-well transitions denoted A and C separates by $\pm 2E_M$ from intra-well transitions denoted B due to the coupling of parity sectors in the transmon circuit. For $E_J \gg E_C$ the dispersion flattens out and E_M is visible as a

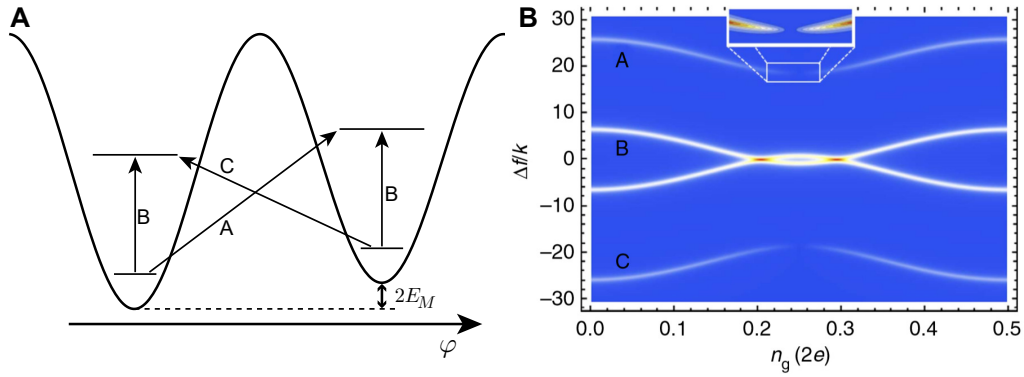

Figure 7.1: **A** Potential of the Majorana transmon with $E_J > E_M$. Lowest energy states (not to scale) are shown with the possible single-photon transitions. **B** Charge dispersion of transitions shown in **A** for $E_C/h = 400$ MHz, $E_J/E_C = 27$, $E_M/h = 0.5$ MHz, and linewidth $k = 50$ kHz. In the transmon limit $E_J/E_C \gg 1$ the dispersion flattens out and E_M introduces a splitting between intra-well transitions B. **B** is adapted from [140].

splitting of intra-well transitions B due to a modification to the harmonic approximation of each well from the fractional Josephson coupling: $E_J \cos(\varphi) \pm E_M \cos(\varphi/2)$. In this regime inter-well transitions A and C are suppressed due to non-overlapping wavefunctions.

A topological nanowire with a small break in the aluminium shell as shown in Figure 7.2**A** is expected to host four Majorana fermions: one at each end and two on each side of the junction. Large plunger electrodes, V_{lplg} and V_{rplg}, are used to tune the chemical potential of the nanowire into a topological regime. With a third electrode, V_{cut}, at the junction one can open or close the coupling between Majorana fermions $\hat{\gamma}_2$ and $\hat{\gamma}_3$. In addition, as observed for gatemons, the junction will form a highly coherent Josephson coupling allowing a single multichannel nanowire to mediate both the trivial Josephson coupling as well as the topological Majorana coupling present in Equation (7.1). To turn on the fractional Josephson effect we need to bring the system into a topological phase by tuning chemical potential and magnetic field.

Figure 7.2**B** shows an InAs nanowire with diameter of ~ 100 nm with one side covered by a 7 nm thick aluminium shell. It is placed on NbTiN bottom gates using a micro manipulator. A small part of the aluminium shell is etched away using a wet etch to form a Josephson junction. The nanowire is connected to a T-shaped qubit island, with simulated charging energy $E_C = 230$ MHz, and the surrounding ground plane [Figure 7.2**C**]. A light RF mill is used to remove the native oxide of InAs before sputtering of NbTiN contacts. The qubit island is capacitively coupled to $\lambda/2$ cavity with resonance frequency ~ 4.95 GHz for readout and microwave control. The cavity, qubit island, and bottoms gates are fabricated for low loss and high-field compatibility in 20 nm NbTiN [77, 142] using e-beam lithography and chlorine-based dry etch. A high density of flux trapping holes is used to trap any flux vortices penetrating the thin NbTiN film. NbTiN crossovers ties ground planes to avoid parasitic modes on the chip[1]. Local 5 nm HfO_2

[1]It is crucial to not use aluminium on-chip bond wires to connect ground planes as these cause large

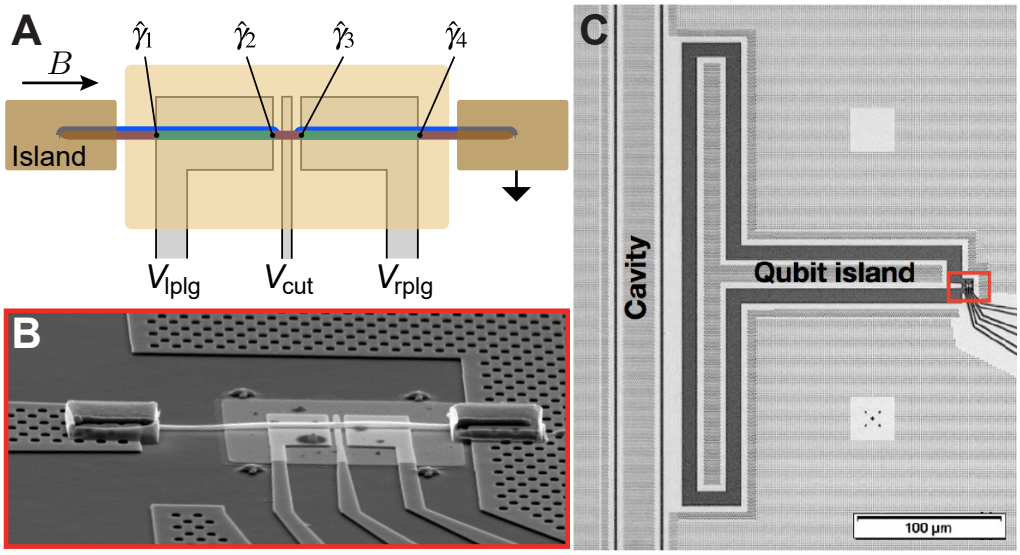

Figure 7.2: **A** Device schematic. An InAs nanowire with one side covered in aluminium (blue) is placed on top of plunger gates which tunes the chemical potential of the nanowire forming topological segments (green). A Majorana fermion forms at each end the topological segments with an electrode V_{cut} controlling the coupling of $\hat{\gamma}_2$ and $\hat{\gamma}_3$ as well as a trivial Josephson coupling $E_J(V_{\text{cut}})$. Schematic adapted from [144]. **B** Scanning electron micrograph of nanowire and bottom gates. **C** Micrograph of the transmon island capacitively coupled to a $\lambda/2$ cavity for readout and microwave control.

deposited with ALD before the NbTiN deposition ensures no leakage between closely spaced gates through the silicon substrate[2]. A second HfO_2 layer 15 nm thick on top of bottom gates acts as gate dielectric between bottom gates and nanowire. On chip LC-filters (not shown) on each gate electrode suppress microwave dissipation through the capacitively coupled gates [143]. A second qubit with no plunger gates is coupled to the same resonator (not shown) but all data presented is from qubit shown. The sample is placed inside a CuBe box filled with microwave absorbing Eccosorb foam to reduce microwave and infrared radiation. The box is mounted in a dilution refrigerator with base temperature < 50 mK (see Figure C.4 for schematic of setup).

7.1 Coherent Control up to 1 T

First we investigate the qubit behaviour in magnetic field parallel to the nanowire with two-tone spectroscopy. During two-tone spectroscopy the cavity resonance is first measured for each magnetic field value to account for changes in the cavity resonance [See Appendix Figure B.1]. Any out-of-plane magnetic field on order of 10 μT will modify the resonance frequency of the cavity but we observe no degradation of resonator Q factor or qubit lifetimes. Figure 7.3 shows the qubit frequency as a function of magnetic field up to 1 T. The qubit frequency exhibits a lobe structure with minima at

amount of dissipation above the critical field of aluminium.

[2]Electrodes spaced $\sim$ 1 μm apart on bare, high-resistive silicon will leak at $\sim \pm 10$ V at base temperature.

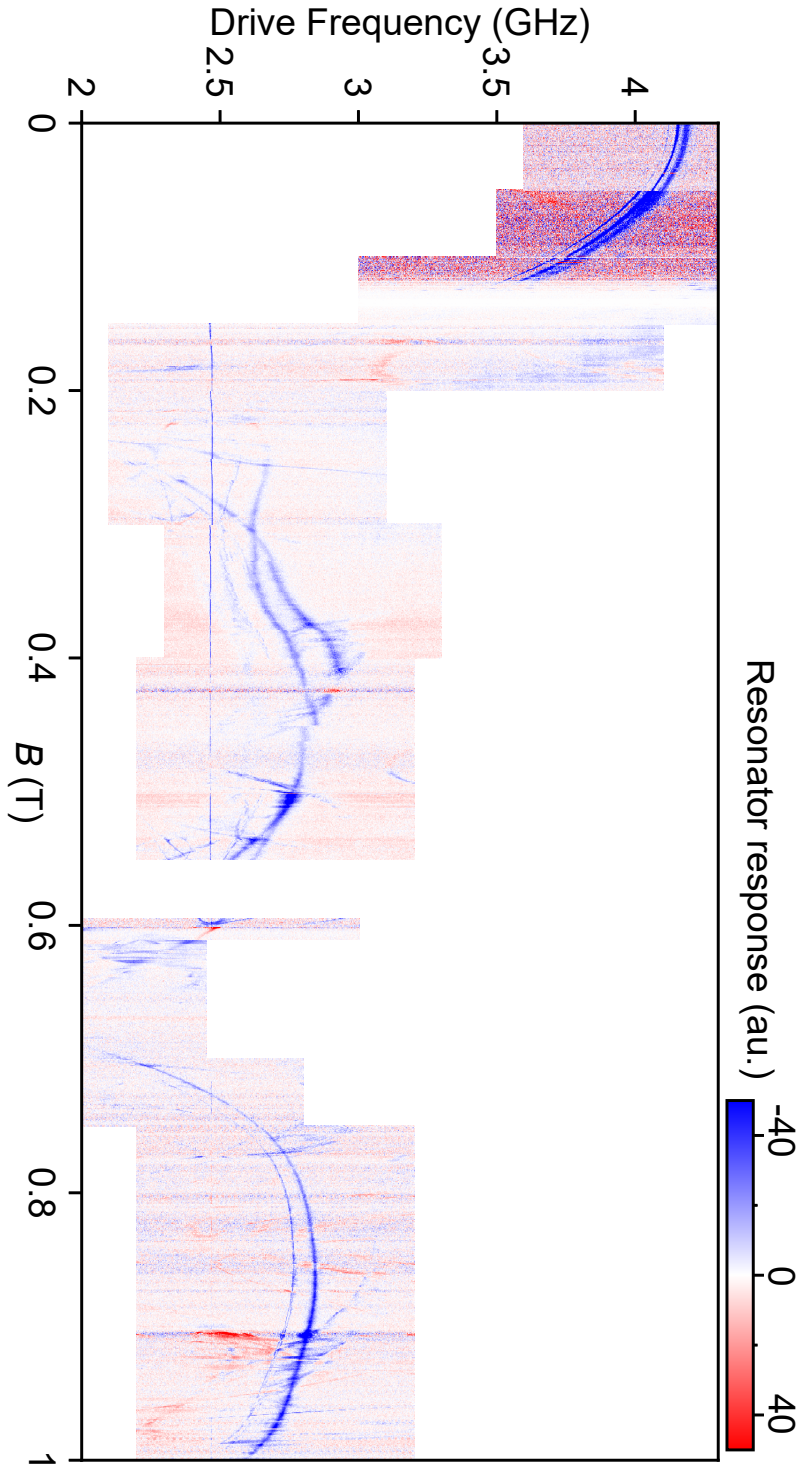

Figure 7.3: Two-tone spectroscopy as a function of magnetic field. Changes in background signal are due to adjustments to qubit drive power to account for varying lifetime and detuning from resonator. Data around 0.58 T omitted due to a mistake in setup during data acquisition. An average is subtracted from data at each magnetic field value.

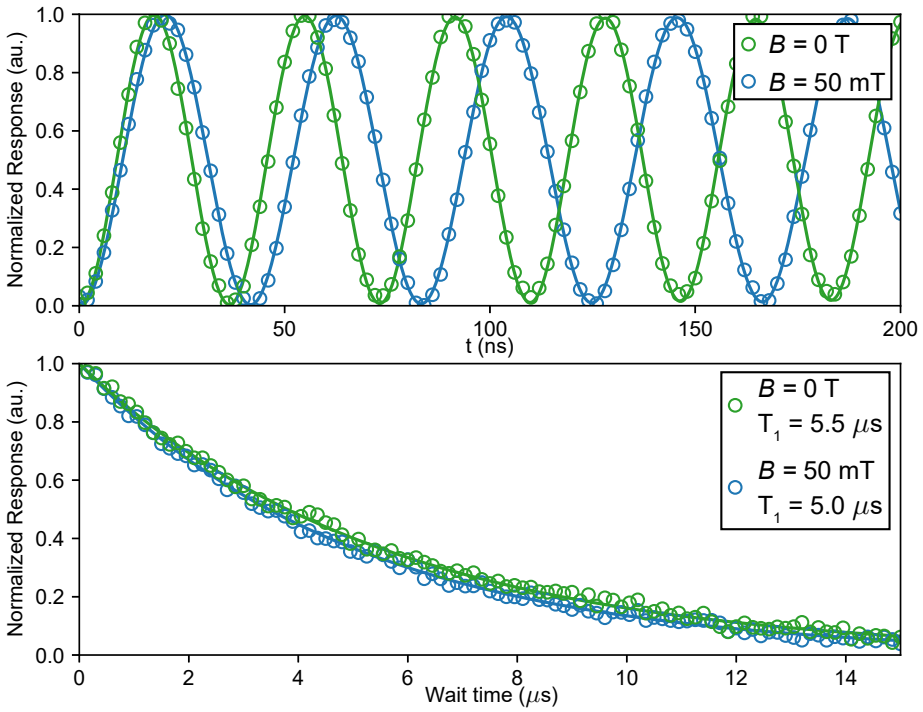

Figure 7.4: Upper (lower) panel shows Rabi oscillations (lifetime decay) of Majorana transmon at 0 and 50 mT. The similarity in qubit performance highlights the Majorana transmon's resilience to magnetic fields. Data is normalized to extracted it parameters.

$B \sim 0.225$ T and $B \sim 0.675$ T. We interpret this as a suppression of the induced gap in the semiconductor due to interference effects in the cross-section of the nanowire. The current density in the semiconductor is mostly confined to the surface of the nanowire forming a cylinder penetrated by a magnetic flux. At half-integer flux quanta through the cylinder the superconductivity is suppressed due to destructive interference. This agrees with resent simulations of the same nanowires [145]. We calculate the effective diameter of the interference loop, assuming half a flux quantum at $B = 0.225$ T, to be $d_{\text{eff}} = \sqrt{2\Phi_0/\pi B} = 76$ nm. As the current density resides inside the nanowire one expects a slightly smaller effective diameter of the electron density than the ~ 100 nm diameter of the nanowire. Similar interference effects have recently been observed in full-shell nanowire devices [146, 147].

The qubit behaviour can be split in the three lobes separated by the destructive regimes. In the zeroth lobe measured from $B \sim 0$ to ~ 150 mT the device behaves indistinguishably from a standard gatemon device. Due to the high drive power multiphoton transitions are present displaying the higher energy states of the qubit. Around 150 mT the system becomes unmeasurable due to the second qubit on the chip anticrossing with the resonator [Figure B.1]. Figure 7.4 shows Rabi oscillations and lifetime decay at $B = 0$ and $B = 50$ mT. At $B = 0$ we observe lifetimes of ~ 5.5 μs similar to previous gatemon devices verifying that additional plunger gates and dielectrics has not compromised qubit performance. The measurements show almost no difference between $B = 0$ and

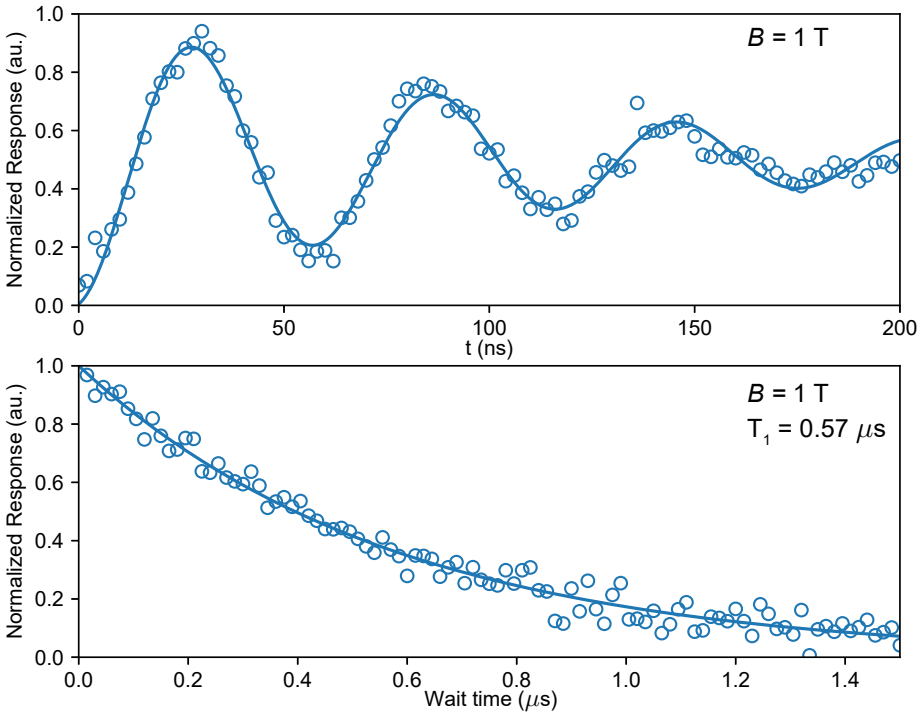

Figure 7.5: Upper (lower) panel shows Rabi osicllations (lifetime decay) of Majorana transmon at $B = 1$ T.

$B = 50$ mT demonstrating excellent parallel magnetic field resilience consistent with recent studies of gatemon qubits [113]. Furthermore, as the field is not finely aligned it verifies that small out-of-plane magnetic fields do not degrade qubit quality. This might eliminate the need for extensive magnetic shielding required in superconducting qubits.

Moving to higher fields in first lobe between ~ 250 mT and ~ 650 mT two main resonances appear. Both states behaves as anharmonic oscillator modes with a broad single-photon transition frequency and a sharper two-photon transition separated by ~ 100 MHz. While the presence of two anharmonic states is consistent with a large E_M term in the Hamiltonian it is unlikely that the splitting is due to Majorana physics as one expects higher magnetic fields to enter the topological phase. Rather the splitting might be connected to low lying energy states coupling to the qubit mode. Indeed several states dispersing strongly with magnetic fields are visible throughout the first lobe. It was not possible to probe the qubit states in time domain due to very low lifetimes.

In the last lobe above $B \sim 650$ mT a single qubit resonance revives with a clear two-photon transition all the way up to $B = 1$ T. Figure 7.5 shows coherent Rabi oscillation of a superconducting transmon qubit at $B = 1$ T with lifetime $T_1 = 0.57$ μs strongly encouraging the feasibility of the experimental setup for hosting Majorana fermions in a coherent transmon. As in the first lobe other resonances strongly dispersing in magnetic field are visible.

7.2 Coupled Qubit and Junction states

To further investigate the anomalous qubit-resonance splitting we tune gate electrodes in the first lobe into a regime with sharp transitions exhibiting qubit line splitting shown in Figure 7.6. A clear, uninterrupted qubit transition frequency indicated by white dashed line is slowly suppressed as the magnetic field is turned up. Additionally around the qubit transition several new resonances appear above $B = 350$ mT oscillating as a function of magnetic field. We speculate that these resonances might be explained by an Andreev bound state indicated by the dashed purple line and a second state only weakly dependent on magnetic field around energy $f_0 \sim 6$ GHz as indicated by the energy diagram inset [Figure 7.6]. The blue and gray dashed lines are transitions from initially excited states with frequencies $f_0 - f_A$ and $f_0 - f_{\text{qubit}}$ respectively. Purple and blue transitions appear mirrored around $f_0/2$ as their frequencies are given by $f_\pm = f_0/2 \pm \delta$ where $\delta = f_A - f_0/2$ (same for white and gray transitions).

At ~ 360 mT an anticrossing appear between the qubit transition and the Andreev transition $f_0 - f_A$ (white and blue lines) indicating a strong coupling. Additionally, the qubit resonance is also observed completely uncoupled from the Andreev transition. The coexistence of the coupled and uncoupled spectra might be explained by the odd and even parity of the Andreev state. In the even parity an Andreev state couples to microwave excitation, such as the qubit resonance, while in the odd parity it is uncoupled [148–150]. As the parity of the Andreev state is switching faster than the measurement is performed we observed the average of the two cases: The odd case with a single qubit resonance (white dashed line) uncoupled from the Andreev state, and the even case with two transition frequencies from the avoided crossing of the qubit and Andreev transitions. Combining the two cases we observe three resonances in the spectrum. Similarly when the direct Andreev transition (purple line) is on resonance with the qubit near $B \sim 390$ mT three pronounced resonances are observed around the bare qubit frequency.

To further probe the spectrum in Figure 7.7 we sweep the gate voltage V_{cut} at fixed magnetic fields. The strong dispersion of the Andreev state is a signature of a local junction state strongly dependent on the electrostatics around the junction. Guides to the eye indicate the same resonances as in Figure 7.6. As a function of gate voltage clear anticrossings between the qubit resonance and both Andreev transitions are observed. Also in gate voltage we observe a clear connection between the Andreev transitions given by $f_\pm = f_0/2 \pm \delta$ further evidence of the simple phenomenological model. At higher fields more resonances appear complicating a full analysis of the spectrum. Further studies and analysis are necessary to completely describe the multitude of transitions.

7.3 Conclusion

In conclusion we have presented simple gatemon circuit with excellent coherence times of 5 μs at 50 mT. The qubit retains coherence up to magnetic fields of 1 T with lifetime $T_1 \sim 0.6$ μs demonstrating the feasibility of the circuit to coherently probe Majorana fermions. At high magnetic fields we observe several additional resonances in

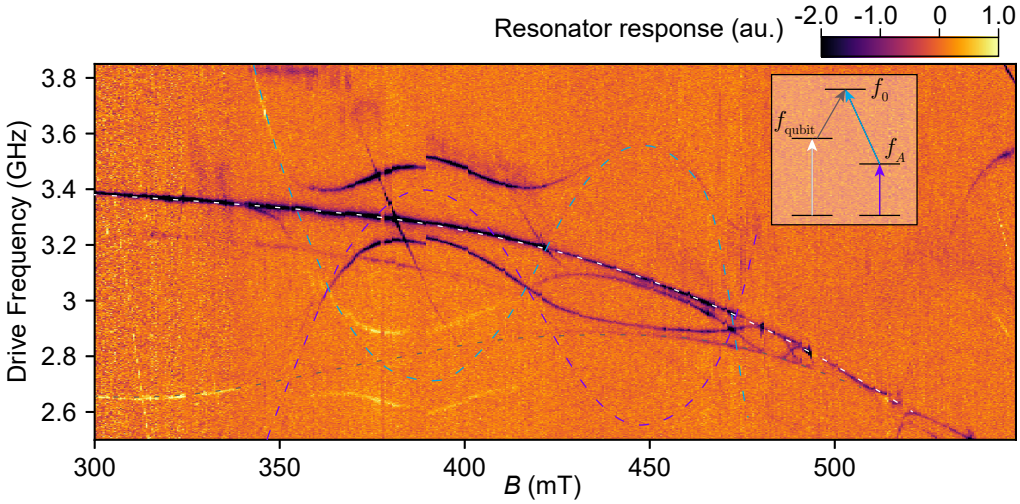

Figure 7.6: Spectroscopy reveals oscillating behaviour of junctions states at gate voltage $V_{\text{cut}} = -1.805$ V and $V_{\text{lplg}} = V_{\text{rplg}} = -1.983$ V. Dashed lines are guides to the eye. Inset shows energy diagram of a phenomenological model consisting of a single strongly dispersing Andreev state f_A and a non-dispersing state f_0. An average is subtracted from each column.

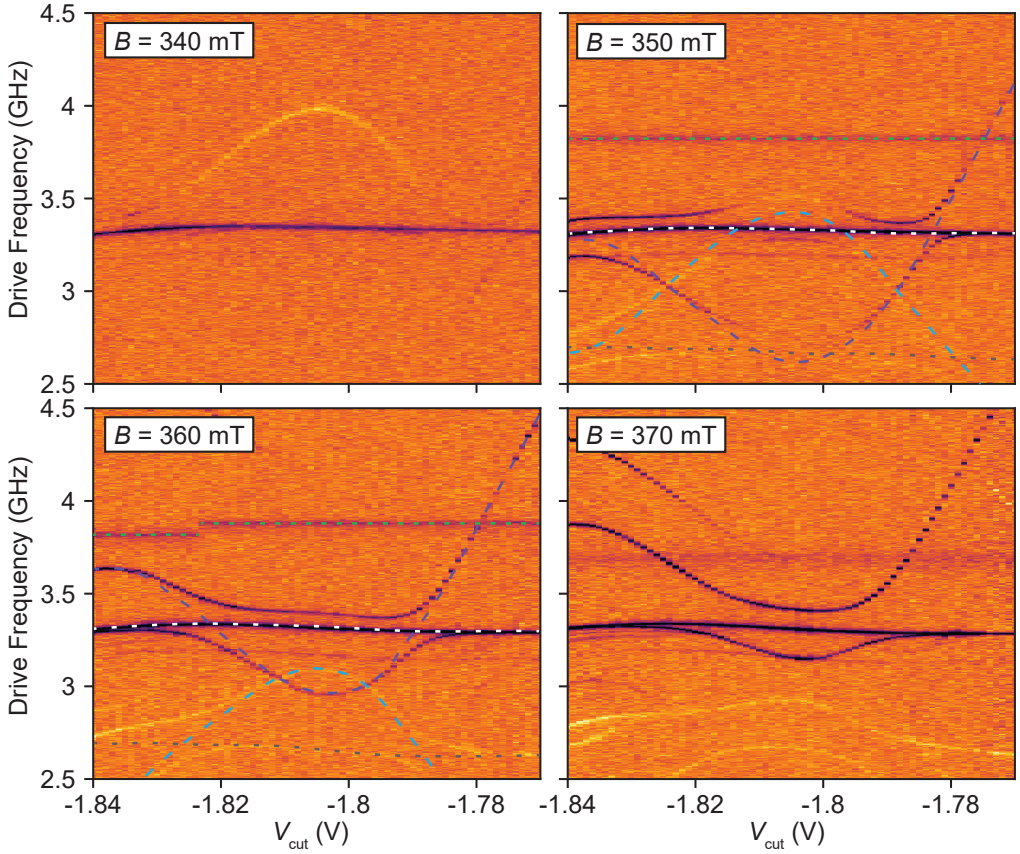

Figure 7.7: Two-tone spectroscopy as a function of gate voltage V_{cut} for different magnetic fields. Dashed lines are guides to the eye. Green dashed line is the resonance of the second qubit coupled to same resonator. An average is subtracted from each column.

two-tone spectroscopy. We speculate that oscillating transitions present in the spectrum are described by simple phenomenological model based on Andreev bound states in the nanowire Josephson junction. Further studies with SQUID-type structures, allowing control of the superconducting phase across the Josephson junction, might help elucidating the origin of these transitions by measuring their energy-phase relations. Alternatively moving to systems with larger E_C would allow distinguishing trivial junction states from anharmonic oscillator modes by measuring charge dispersions, which carries the signature of coupled Majorana fermions as shown in Figure 7.1. Additionally, high-field compatible transmon qubits might open possibilities for hybrid systems such as spin ensemble-based quantum memories in superconducting circuits [151].

Chapter 8

Outlook

It is an exciting time to work in experimental quantum computing research. During the last decade both existing and emerging technologies for quantum bits have taken tremendous steps towards true scalable quantum computing. The improvements are powered by new architectures, scalable 2D ion-traps, new ideas, elimination of charge noise in transmon qubits, and new materials, epitaxial semiconductor-superconductor interfaces. The generally agreed upon strategy is to encode qubits in non-local, topological degrees of freedom decoupled from the environment. In this thesis we have investigated three different approaches towards protected qubits all based on hybrid semiconductor-superconductor nanowires. However, from the studies presented here, or in fact throughout the field of experimental quantum computing, it is impossible to predict which platform will succeed.

In recent years most focus has been on superconducting qubits and quantum error correction. These systems has the advantage of being able to optimize and benchmark single qubits leading to amazing progress. We will likely see the first demonstration of a small scale surface code outperforming its individual parts in the next few years. However, going from small scale surface code to full fledged quantum computing is a monumental task. Just the sheer number of qubits required is daunting. On top of that comes a huge amount of classical computing power needed for error correction and signal processing. Fortunately, no single challenge seems unsolvable and the rest might "just" be engineering. One remaining essential question to be answered in quantum error correction is: Are qubit errors truly local on large scale?

Topological materials or passive quantum error correction promise a different route to quantum computing based on inherent protection. These platforms will also need a form of active error correction to remove errors but the expected number of qubits is much lower greatly reducing the challenge of scalability. The trade off is a complicated materials or design problem to create a topological phase. As the topology is created by the system itself it is very hard to prove that the system behaves as it should - any local measurement cannot probe the topological degree of freedom we are interested in. The main challenge is building the first qubit with control and readout both hard to achieve due to the protected nature. Additionally the same question needs to be answered as for quantum error correction: Are system errors truly topologically separated from the

protected qubit?

Another tantalizing approach to scalable quantum computing are hybrid systems containing both topological qubits and superconducting qubits. Each type of protection might exhibit different advantages and disadvantages which can be utilized for different parts of a quantum computer. For example superconducting qubits might be ideal for magic state factories, which needs good initial T-gates, the T-gates performed without protection, as well as fast gate operations for purification. However, as magic state distillation is an inherent random procedure we want to store T-gates in quantum memory until required for computation. Quantum memory requires long-lived qubits ideally with low-overhead of classical computing power - maybe best implemented in low-overhead topological materials. In this thesis we have demonstrated that the same architecture might host different protected qubit. As topological qubits becomes a reality a research direction lies in transferring quantum information from one type of protected qubit to another to take full advantage each platform.

As mentioned it is an incredible exciting field to part of and I look forward to learn about new ideas, inventions, and possibilities along the path to a quantum computer.

Appendices

Appendix A

Second order perturbation theory

In this section we explicitly calculate the energy correction to second order in g/Δ for the coupled circuit of transmon and resonator described in section 3.4. The generalized Jaynes-Cummings Hamiltonian written with product eigenstates $|n, j\rangle$ of $\widehat{H}_0$, where n is the resonator excitation and j the atom excitation, is given by:

$$\begin{aligned} \widehat{H} &= \widehat{H}_0 + \widehat{V}, \\ \widehat{H}_0 &= \hbar\omega_r \hat{a}^\dagger \hat{a} + \hbar \sum_i \omega_i |i\rangle\langle i|, \\ \widehat{V} &= \hbar \sum_i g_{i,i+1}(\hat{a}|i+1\rangle\langle i| + \hat{a}^\dagger |i\rangle\langle i+1|). \end{aligned} \tag{A.1}$$

The correction to the eigenenergies can be found assuming $g_{ij} = 0$ for $j \neq i \pm 1$. First order correction is

$$E^1_{|n,j\rangle} = \langle n, j|\widehat{V}|n, j\rangle = 0.$$

And second order:

$$
\begin{aligned}
E^2_{|n,j\rangle} \overset{n,j>0}{=} & \sum_{(m,i)\neq(n,j)} \frac{\left|\langle m,i|\widehat{V}|n,j\rangle\right|^2}{E^0_{|n,j\rangle} - E^0_{|m,i\rangle}} \\
= & \frac{\left|\langle n+1,j-1|\widehat{V}|n,j\rangle\right|^2}{E^0_{|n,j\rangle} - E^0_{|n+1,j-1\rangle}} + \frac{\left|\langle n-1,j+1|\widehat{V}|n,j\rangle\right|^2}{E^0_{|n,j\rangle} - E^0_{|n-1,j+1\rangle}} \\
= & \frac{g^2_{j-1,j}(n+1)}{\hbar\omega_j - \hbar\omega_r} + \frac{g^2_{j,j+1}n}{\hbar\omega_r - \hbar\omega_{j+1}} \\
= & \hbar\chi_{j-1,j}(n+1) - \hbar\chi_{j,j+1}n \\
E^2_{|0,j\rangle} \overset{j\geq 0}{=} & \frac{\left|\langle 1,j-1|\widehat{V}|0,j\rangle\right|^2}{E^0_{|0,j\rangle} - E^0_{|1,j-1\rangle}} = \hbar\chi_{j-1,j} \\
E^2_{|n,0\rangle} \overset{n\geq 0}{=} & \frac{\left|\langle n-1,1|\widehat{V}|n,0\rangle\right|^2}{E^0_{|n,0\rangle} - E^0_{|n-1,1\rangle}} = -\hbar\chi_{01}n \\
E^2_{|0,0\rangle} = & 0
\end{aligned}
$$

where $\chi_{ij} = g^2_{ij}/\omega_{ij} - \omega_r$. Collecting the terms the effective Hamiltonian becomes

$$
\begin{aligned}
\widehat{H}_{\text{eff}} = & \sum_{n,i} E_{|n,i\rangle}|n,i\rangle\langle n,i| \\
= & \hbar\omega_r\hat{a}^\dagger\hat{a} + \hbar\sum_i \omega_i|i\rangle\langle i| + \hbar\sum_i \chi_{i,i+1}|i+1\rangle\langle i+1| \\
& - \hbar\chi_{01}\hat{a}^\dagger\hat{a}|0\rangle\langle 0| + \hbar\sum_{i=1}\left(\chi_{i-1,i} - \chi_{i,i+1}\right)\hat{a}^\dagger\hat{a}|i\rangle\langle i|,
\end{aligned}
$$

where the resonator states have been written with raising and lowering operators. Lastly we truncate the transmon to a two-level system:

$$
\begin{aligned}
H_{\text{eff}} = & \hbar\omega_r\hat{a}^\dagger\hat{a} + \hbar\omega_1|1\rangle\langle 1| + \hbar\chi_{01}|1\rangle\langle 1| \\
& - \hbar\chi_{01}\hat{a}^\dagger\hat{a}|0\rangle\langle 0| + \hbar\left(\chi_{01} - \chi_{12}\right)\hat{a}^\dagger\hat{a}|1\rangle\langle 1| \\
= & \hbar(\omega_r - \chi_{01}|0\rangle\langle 0| + (\chi_{01} - \chi_{12})|1\rangle\langle 1|)\hat{a}^\dagger\hat{a} + \hbar(\omega_1 + \chi_{01})|1\rangle\langle 1| \\
= & \hbar\left(\omega_r - \frac{\chi_{12}}{2}\right)\hat{a}^\dagger\hat{a} + \hbar\frac{1}{2}(\omega_1 + \chi_{01})\hat{\sigma}_z + \hbar\chi\hat{a}^\dagger\hat{a}\hat{\sigma}_z,
\end{aligned}
$$

with $\chi = \chi_{01} - \chi_{12}/2$ and $\sigma_z = |1\rangle\langle 1| - |0\rangle\langle 0|$.

Appendix B

Magnetic field response of NbTiN resonator

Figure B.1 shows resonator response measured interleaved with data in Figure 7.3 for readout frequency adjustments.

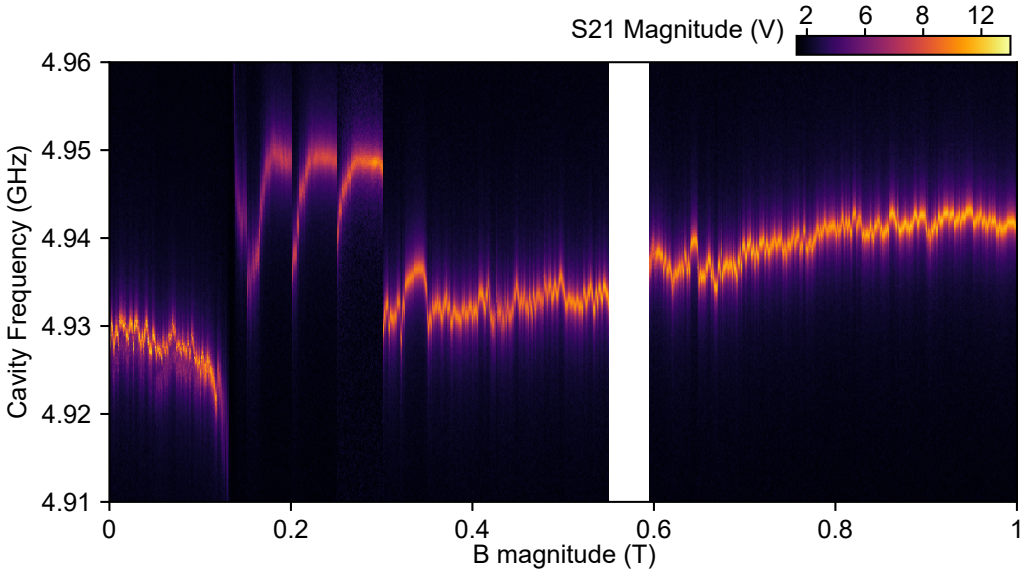

Figure B.1: Modulation of resonance frequency of the NbTiN, $\lambda/2$ cavity used for readout in Chapter 7. Due to the large fluctuation the readout frequency is adjusted each time the magnetic field is move. Large jumps around 0.2 T are due to corrections of the out-of-plane magnetic field on order of ~ 0.1 mT (not shown).

Appendix C

Schematics of Experimental Setups

Schematics of each setup used for measurements presented in this thesis.

Aluminium box with indium seal used in setups presented in Figures C.1, C.2, and C.3 is installed inside a copper box to reduce infrared radiation. The insides of both boxes are covered in black absorptive paint (Aeroglaze Z306) to increase infrared absorption. For setups C.2 and C.3 a long cylindrical cryoperm magnetic shield is installed.

The CuBe box in Figure C.4 is filled with non-magnetic Eccosorb foam (Eccosorb LS-26) for dielectric absorption of radiation. As Aeroglaze Z306 is magnetically activated it is unclear if it is effective at high magnetic fields required for the experiment.

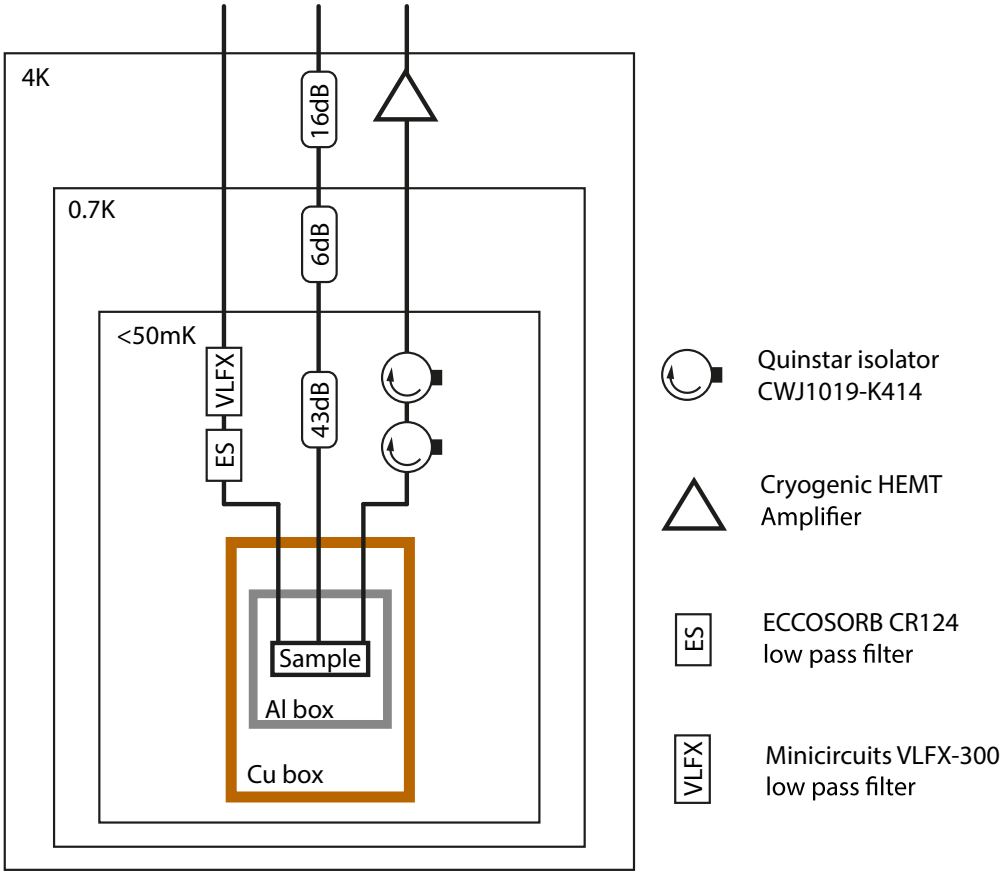

Figure C.1: Schematic of setup for single qubit devices in Chapter 5. The data in Figure 5.2 were acquired using a vector network analyzer. For the Sample 1 data in Figures 5.3, 5.4, and 5.5 we mix down to dc and sample the homodyne response, V_H. For the Sample 2 data in Figure 5.5 we mix down to an intermediate frequency before sampling and then perform digital homodyne to extract the cavity phase response.

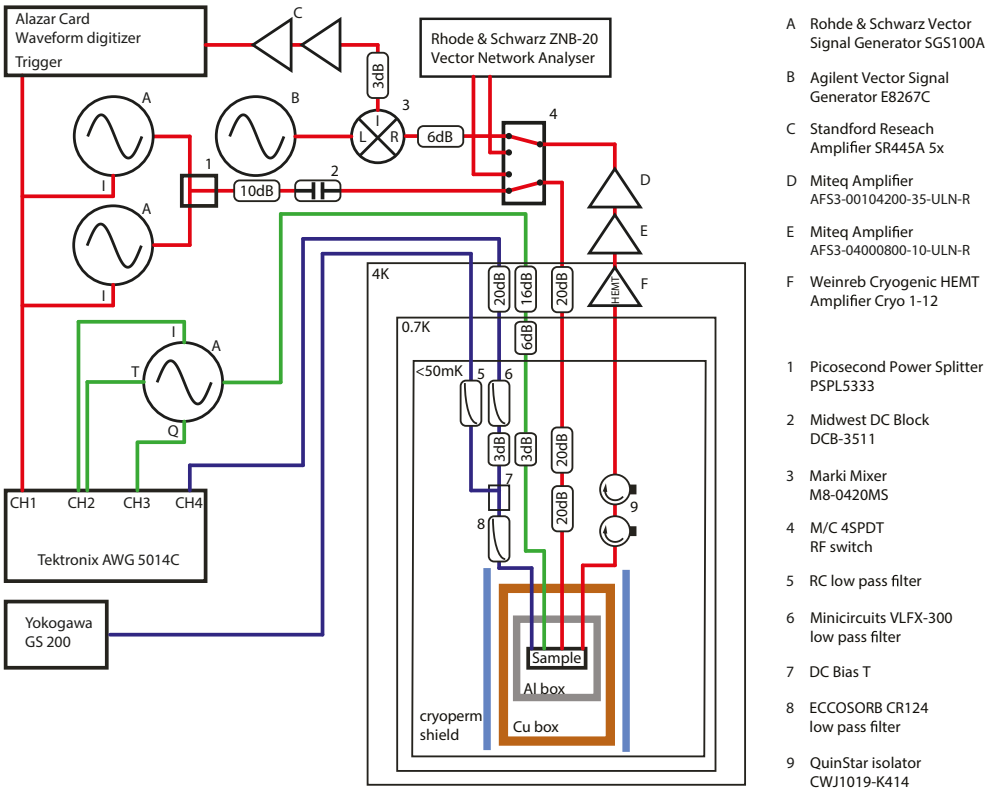

Figure C.2: Schematic of experimental setup for two qubit device in Chapter 5.

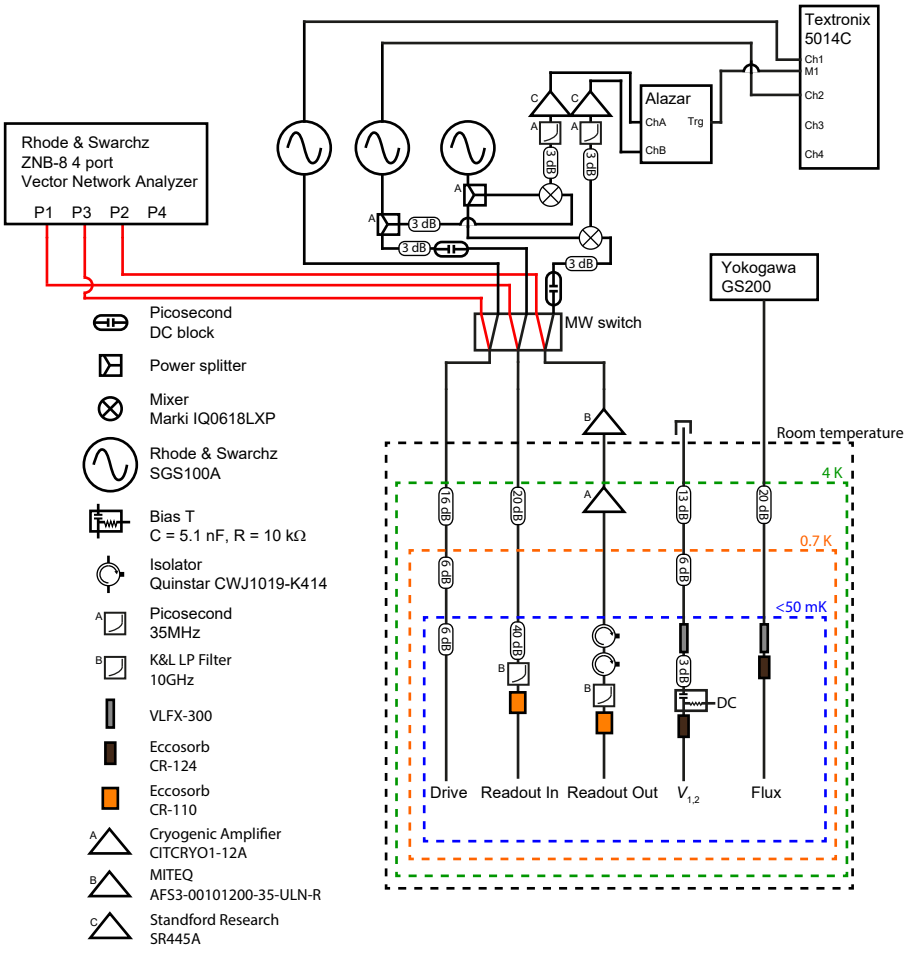

Figure C.3: Schematic of experimental setup device in Chapter 6.

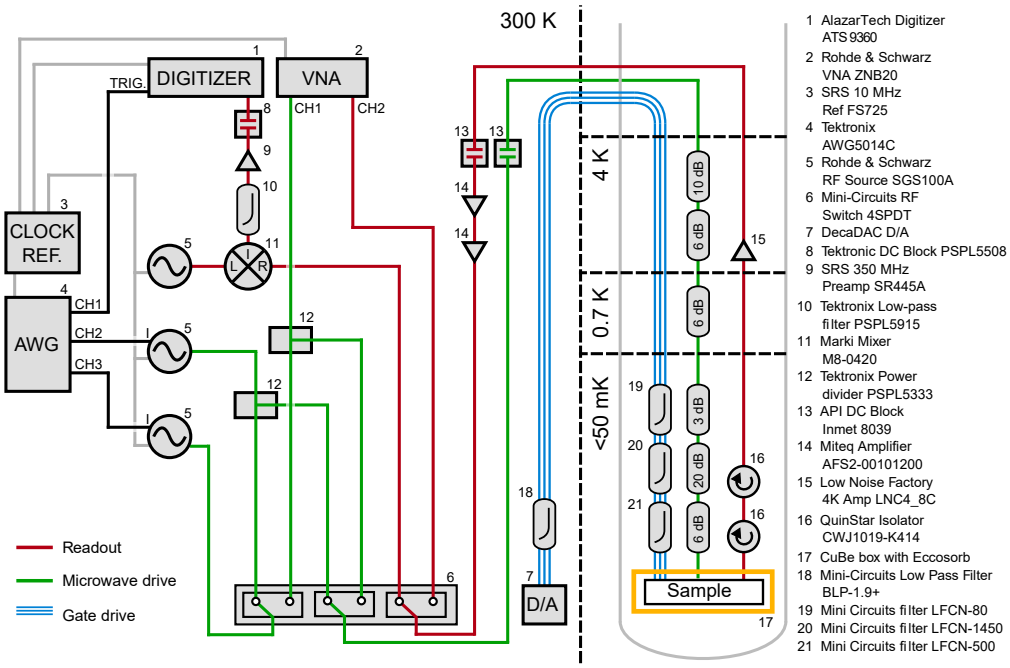

Figure C.4: Schematic of experimental setup for device in Chapter 7. Figure adapted from [144]

Appendix D

Fabrication Recipes

Fabrication recipes for samples presented in this thesis. Metal evaporation and *in situ* argon milling were done in an AJA International metal evaporation system. E-beam lithography were performed in a 100 kV Elionix electron beam lithography system.

D.1 Single qubit devices presented in Chapter 5

Al film deposition

- Silicon substrate with thermal oxide cleaned in acetone and IPA
- Metal deposition: 1 min Ar mill, 75 nm Al

Gold alignment marks

- Resist spin: A4, 4000 rpm, 45 s, bake at 185°C for 4 min
- E-beam exposure: dose 1200 μC/cm^2
- Development: 60 s MIBK:IPA 1:3, 10 s IPA, O_2 plasma ash
- Metal deposition: 10 nm Ti, 40 nm Au
- Lift off: Acetone

Al film wet etching

- Resist spin: A4, 4000 rpm, 45 s, bake at 185°C for 4 min
- E-beam exposure: dose 1200 μC/cm^2
- Development: 60 s MIBK:IPA 1:3, 10 s IPA, O_2 plasma ash
- Etch: 25 s Transene Type D at 54°C, 30 s DI water, 10 s IPA
- Resist strip: Acetone

Nanowire deposition

- Resist spin: A4, 4000 rpm, 45 s, bake at 185°C for 4 min
- E-beam exposure: dose 1200 μC/cm^2
- Development: 60 s MIBK:IPA 1:3, 10 s IPA, O_2 plasma ash
- Nanowire dry deposition
- Resist strip: Acetone

Gold alignment marks for nanowire

- Resist spin: A4, 4000 rpm, 45 s, bake at 185°C for 4 min
- E-beam exposure: dose 1200 μC/cm^2
- Development: 60 s MIBK:IPA 1:3, 10 s IPA, O_2 plasma ash
- Metal deposition: 5 nm Ti, 35 nm Au
- Lift off: Acetone

Nanowire wet etch

- Resist spin: A4, 4000 rpm, 45 s, bake at 185°C for 4 min
- E-beam exposure: dose 1200 μC/cm^2
- Development: 60 s MIBK:IPA 1:3, 10 s IPA, O_2 plasma ash
- Etch: 12 s Transene Type D at 50°C, 30 s DI water, 10 s IPA
- Resist strip: Acetone

Nanowire contacts and side gate

- Resist spin: EL9, 4000 rpm, 45 s, bake at 185°C for 1 min
- Resist spin: A4, 4000 rpm, 45 s, bake at 185°C for 4 min
- E-beam exposure: dose 1200 μC/cm^2
- Development: 60 s MIBK:IPA 1:3, 10 s IPA, O_2 plasma ash
- Metal deposition: 3 min Ar mill, 1 nm Ti, 150 nm Al
- Resist strip: Acetone

D.2 Two-qubit device presented in Chapter 5

Al film deposition

- Silicon substrate with no thermal oxide cleaned in acetone and IPA
- Metal deposition: 1 min Ar mill, 75 nm Al

Gold alignment marks

- Resist spin: A4, 4000 rpm, 45 s, bake at 185°C for 3 min
- E-beam exposure: dose 1200 μC/cm^2
- Development: 60 s MIBK:IPA 1:3, 10 s IPA, O_2 plasma ash
- Metal deposition: 5 nm Ti, 45 nm Au
- Lift off: Acetone

Al film wet etching

- Resist spin: EL9, 4000 rpm, 45 s, bake at 185°C for 3 min
- Resist spin: CSAR4, 4000 rpm, 45 s, bake at 185°C for 3 min
- E-beam exposure: dose 450 μC/cm^2
- Development: 60 s O-xylene, 120 s MIBK:IPA 1:3, 15 s IPA, O_2 plasma ash
- Etch: 50 s Transene Type D at 53°C, 30 s DI water, 15 s IPA (longer etch time due to contaminated/old etch bottle)
- Resist strip: Acetone

Crossover oxide

- Resist spin: EL13, 4000 rpm, 45 s, bake at 185°C for 3 min
- Resist spin: CSAR4, 4000 rpm, 45 s, bake at 185°C for 3 min
- E-beam exposure: dose 450 μC/cm^2
- Development: 60 s O-xylene, 120 s MIBK:IPA 1:3, 15 s IPA, O_2 plasma ash
- Oxide deposition: 250 nm SiO_2
- Lift off: Acetone

Crossover metal

- Resist spin: EL13, 4000 rpm, 45 s, bake at 185°C for 3 min
- Resist spin: CSAR4, 4000 rpm, 45 s, bake at 185°C for 3 min
- E-beam exposure: dose 450 μC/cm^2
- Development: 60 s O-xylene, 120 s MIBK:IPA 1:3, 15 s IPA, O_2 plasma ash
- Metal deposition: 3 min Ar mill, 300 nm Al
- Lift off: Acetone

Nanowire deposition

- Resist spin: EL9, 4000 rpm, 45 s, bake at 185°C for 3 min
- E-beam exposure: dose 450 μC/cm^2
- Development: 60 s MIBK:IPA 1:3, 10 s IPA, O_2 plasma ash
- Nanowire dry deposition
- Resist strip: Acetone

Nanowire wet etch

- Resist spin: A4, 4000 rpm, 45 s, bake at 185°C for 4 min
- E-beam exposure: dose 1200 μC/cm^2
- Development: 60 s MIBK:IPA 1:3, 10 s IPA, O_2 plasma ash
- Etch: 12 s Transene Type D at 50°C, 30 s DI water, 10 s IPA
- Resist strip: Acetone

Gold alignment marks for nanowire

- Resist spin: A4, 4000 rpm, 45 s, bake at 185°C for 3 min
- E-beam exposure: dose 1200 μC/cm^2
- Development: 60 s MIBK:IPA 1:3, 10 s IPA, O_2 plasma ash
- Metal deposition: 5 nm Ti, 45 nm Au
- Lift off: Acetone

Nanowire contacts and side gate

- Resist spin: EL9, 4000 rpm, 45 s, bake at 185°C for 1 min
- Resist spin: A4, 4000 rpm, 45 s, bake at 185°C for 4 min
- E-beam exposure: dose 1200 μC/cm^2
- Development: 60 s MIBK:IPA 1:3, 10 s IPA, O_2 plasma ash
- Metal deposition: 5.5 min Ar mill, 1 nm Ti, 150 nm Al
- Resist strip: Acetone

Al film wet etching

- Resist spin: EL9, 4000 rpm, 45 s, bake at 185°C for 3 min
- Resist spin: CSAR4, 4000 rpm, 45 s, bake at 185°C for 3 min
- E-beam exposure: dose 450 μC/cm^2
- Development: 60 s O-xylene, 120 s MIBK:IPA 1:3, 15 s IPA, O_2 plasma ash
- Etch: 20 s Transene Type D at 53°C, 30 s DI water, 15 s IPA
- Resist strip: Acetone

D.3 Device presented in Chapter 6

Deep etch silicon marks

- Resist spin: EL9, 4000 rpm, 45 s, bake at 185°C for 1 min
- Resist spin: CSAR9, 4000 rpm, 45 s, bake at 185°C for 1 min
- E-beam exposure: dose 400 μC/cm^2
- Development: 60 s O-xylene, 75 s MIBK:IPA 1:3, 15 s IPA, O_2 plasma ash
- RIE deep etch: Gas cycles C_4F_8:SF_6 1:1 / C_4F_8
- Resist strip: O_2 plasma

Al film and control etch

- Metal deposition: 1 min Ar mill, 100 nm Al
- Resist spin: AZ1505, 4000 rpm, 45 s, bake at 115°C for 2 min
- UV exposure in a Heidelberg μPG101 LED writer: dose 20 ms
- Development: 60 s AZdev:MQ 1:1, 30 s DI water, 30 s DI water, O_2 plasma ash
- Reactive Ion Etch: ICP 20 s Cl_2, 15 s HBr:Cl_2 3:5.
- Resist strip: Acetone

SiO_x crossover insulator

- Resist spin: LOR3B, 4000 rpm, 45 s, bake at 185°C for 5 min
- Resist spin: LOR3B, 4000 rpm, 45 s, bake at 185°C for 5 min
- Resist spin: AZ1505, 4000 rpm, 45 s, bake at 115°C for 2 min
- UV exposure in a Heidelberg μPG101 LED writer: dose 20 ms
- Development: 60 s AZdev:MQ 1:1, 30 s DI water, 30 s DI water, O_2 plasma ash
- Oxide deposition: 200 nm SiO_2
- Resist strip: NMP

Bottom gates, these got damaged later due to fabrication mistake.

- Resist spin: EL9, 4000 rpm, 45 s, bake at 185°C for 1 min
- Resist spin: A4, 4000 rpm, 45 s, bake at 185°C for 2 min
- E-beam exposure: dose 1100 μC/cm^2
- Development: 60 s MIBK:IPA 1:3, 10 s IPA, O_2 plasma ash
- Metal deposition: 30 nm Al
- Resist strip: Acetone

Nanowire wet etch, bottom resist layers before nanowire placement meant to protect Al bottomgates from nanowire etch step. This failed leading to an etched bottom gate likely due to a wrong dose in the e-beam exposure. Side gates were added to the design to compensate for the etched bottom gate.

- Resist spin: A4, 4000 rpm, 45 s, bake at 185°C for 2 min
- Resist spin: A4, 4000 rpm, 45 s, bake at 185°C for 2 min
- Nanowire placement with micromanipulator.
- Resist spin: EL6:A4 2:3, 4000 rpm, 45 s, bake at 185°C for 4 min
- E-beam exposure: dose 500 μC/cm^2
- Development: 60 s MIBK:IPA 1:3, 10 s IPA, O_2 plasma ash
- Etch: 9 s Transene Type D at 50°C, 30 s DI water, 10 s IPA
- Resist not stripped.

Nanowire contacts

- Resist spin: A4, 4000 rpm, 45 s, bake at 115°C for 2 min
- Resist spin: A4, 4000 rpm, 45 s, bake at 115°C for 2 min
- E-beam exposure: dose 1200 μC/cm^2
- Development: 60 s MIBK:IPA 1:3, 10 s IPA, O_2 plasma ash
- Metal deposition: 5 min Ar mill, 1 nm Ti, 175 nm Al
- Resist strip: Acetone

Nanowire sidegates

- Resist spin: A6, 4000 rpm, 45 s, bake at 115°C for 2 min
- Resist spin: A6, 4000 rpm, 45 s, bake at 115°C for 2 min
- E-beam exposure: dose 1200 μC/cm^2
- Development: 60 s MIBK:IPA 1:3, 10 s IPA, O_2 plasma ash
- Metal deposition: 5 min Ar mill, 1 nm Ti, 175 nm Al
- Resist strip: Acetone

D.4 Device presented in Chapter 7

Tungsten alignment marks

- Resist spin: LOR3B, 4000 rpm, 45 s, bake at 185°C for 5 min
- Resist spin: CSAR4, 4000 rpm, 45 s, bake at 115°C for 2 min
- E-beam exposure: dose 400 μC/cm^2
- Development: 30 s ZED50, 20 s IPA, DI water rinse
- Development: 5 s MF321, DI water rinse, O_2 plasma ash
- Metal deposition: 5 nm Ti, sputter ~90 nm W
- Lift off: NMP

Bottom ALD

- Resist spin: EL13, 4000 rpm, 45 s, bake at 185°C for 1 min
- Resist spin: A4, 4000 rpm, 45 s, bake at 185°C for 1 min
- E-beam exposure: dose 900 μC/cm^2
- Development: 60 s MIBK:IPA 1:3, 15 s IPA, O_2 plasma ash
- ALD deposition: 5 nm HfO_x at 90°C
- Lift off: NMP

NbTiN deposition and patterning

- Metal deposition: Sputter NbTi in N atmosphere 20 nm
- Resist spin: CSAR9, 4000 rpm, 45 s, bake at 185°C for 2 min
- E-beam exposure: dose 400 μC/cm^2
- Development: 60 s O-xylene, 15 s IPA, O_2 plasma ash
- Reactive Ion Etch: PRO ICP etcher with Cl_2 gas
- Resist strip: 1,3-dioxolane

Top ALD

- Resist spin: EL13, 4000 rpm, 45 s, bake at 185°C for 1 min
- Resist spin: A4, 4000 rpm, 45 s, bake at 185°C for 1 min
- E-beam exposure: dose 900 μC/cm^2
- Development: 60 s MIBK:IPA 1:3, 15 s IPA, O_2 plasma ash
- ALD deposition: 15 nm HfO_x at 90°C
- Lift off: NMP

Nanowire shell etch and NbTiN crossover insulator

- Resist spin: A4, 4000 rpm with slow acceleration, 45 s, bake at 115°C for 2 min
- E-beam exposure: dose 900 μC/cm^2 for nanowire shell etch
- E-beam exposure: dose 60 mC/cm^2 for crosslinked PMMA insulator under NbTiN crossovers
- Development: 60 s MIBK:IPA 1:3, 15 s IPA, O_2 plasma ash
- Etch: 9 s Transene Type D at 50°C, 15 s DI water at 50°C, 60 s DI water
- Resist strip: Acetone

Nanowire contacts and NbTiN crossovers

- Resist spin: A4, 4000 rpm, 45 s, bake at 115°C for 2 min
- Resist spin: A4, 4000 rpm, 45 s, bake at 115°C for 2 min
- Resist spin: A4, 4000 rpm, 45 s, bake at 115°C for 2 min
- E-beam exposure: dose 900 μC/cm^2 for nanowire shell etch
- E-beam exposure: dose 60 mC/cm^2 for crosslinked PMMA insulator under NbTiN crossovers
- Development: 60 s MIBK:IPA 1:3, 10 s IPA, O_2 plasma ash
- Metal deposition: 5 min Ar mill, Sputter NbTi in N atmosphere 180 nm
- Resist strip: 1,3-Dioxolane

Bibliography

[1] J. Bardeen & W.H.Brattain. "The transistor, a semiconductor triode". *Phys. Rev.* **74.2**, 230 (1948).

[2] W. Shockley. "Transistor technology evokes new physics". *Nobel lecture* 344 (1956).

[3] J. S. Kilby. "Miniaturized electronic circuits". *US Patent* 3,138,743 (1964).

[4] G. E. Moore. "Cramming more components onto integrated circuits". Electronics (1965).

[5] R. P. Feynman. "Simulating physics with computers". *International Journal of Theoretical Physics* **21**, 467–488 (1982).

[6] S. Lloyd. "Universal Quantum Simulators". *Science* **273**, 1073–1078 (1996).

[7] D. S. Abrams & S. Lloyd. "Quantum Algorithm Providing Exponential Speed Increase for Finding Eigenvalues and Eigenvectors". *Phys. Rev. Lett.* **83**, 5162–5165 (1999).

[8] M. Schuld, I. Sinayskiy & F. Petruccione. "An introduction to quantum machine learning". *Contemporary Physics* **56**, 172–185 (2015).

[9] L. K. Grover. "A fast quantum mechanical algorithm for database search". In *the twenty-eighth annual ACM symposium*, 212–219 (ACM Press, New York, New York, USA, 1996).

[10] P. W. Shor. "Algorithms for Quantum Computation: Discrete Logarithms and Factoring ". In *Proceedings 35th Annual Symposium on Foundations of Computer Science*, 124–134 (IEEE, 1994).

[11] T. P. Harty, D. T. C. Allcock, C. J. Ballance, L. Guidoni, H. A. Janacek, N. M. Linke, D. N. Stacey & D. M. Lucas. "High-Fidelity Preparation, Gates, Memory, and Readout of a Trapped-Ion Quantum Bit". *Phys. Rev. Lett.* **113**, 220501 (2014).

[12] T. Monz, D. Nigg, E. A. Martinez, M. F. Brandl, P. Schindler, R. Rines, S. X. Wang, I. L. Chuang & R. Blatt. "Realization of a scalable Shor algorithm". *Science* **351**, 1068–1070 (2016).

[13] C. Figgatt, D. Maslov, K. A. Landsman, N. M. Linke, S. Debnath & C. Monroe. "Complete 3-Qubit Grover search on a programmable quantum computer". *Nature Communications* **8**, 1918 (2017).

[14] R. J. Schoelkopf & S. M. Girvin. "Wiring up quantum systems." *Nature* **451**, 664–669 (2008).

[15] F. Yan, S. Gustavsson, A. Kamal, J. Birenbaum, A. P. Sears, D. Hover, T. J. Gudmundsen, D. Rosenberg, G. Samach, S. Weber, J. L. Yoder, T. P. Orlando, J. Clarke, A. J. Kerman & W. D. Oliver. "The flux qubit revisited to enhance coherence and reproducibility". *Nature Communications* **7**, 1–9 (2016).

[16] N. Ofek, A. Petrenko, R. Heeres, P. Reinhold, Z. Leghtas, B. Vlastakis, Y. Liu, L. Frunzio, S. M. Girvin, L. Jiang, M. Mirrahimi, M. H. Devoret & R. J. Schoelkopf. "Extending the lifetime of a quantum bit with error correction in superconducting circuits". *Nature* 1–5 (2016).

[17] R. Barends, J. Kelly, A. Megrant, D. Sank, E. Jeffrey, Y. Chen, Y. Yin, B. Chiaro, J. Mutus, C. Neill, P. O'Malley, P. Roushan, J. Wenner, T. C. White, A. N. Cleland & J. M. Martinis. "Coherent Josephson qubit suitable for scalable quantum integrated circuits." *Phys. Rev. Lett.* **111**, 080502 (2013).

[18] A. D. Córcoles, E. Magesan, S. J. Srinivasan, A. W. Cross, M. Steffen, J. M. Gambetta & J. M. Chow. "Demonstration of a quantum error detection code using a square lattice of four superconducting qubits." *Nature Communications* **6**, 6979 (2015).

[19] M. Veldhorst, J. C. C. Hwang, C. H. Yang, A. W. Leenstra, B. de Ronde, J. P. Dehollain, J. T. Muhonen, F. E. Hudson, K. M. Itoh, A. Morello & A. S. Dzurak. "An addressable quantum dot qubit with fault-tolerant control-fidelity". *Nature Nanotechnology* **9**, 981 (2014).

[20] T. F. Watson, S. G. J. Philips, E. Kawakami, D. R. Ward, P. Scarlino, M. Veldhorst, D. E. Savage, M. G. Lagally, M. Friesen, S. N. Coppersmith, M. A. Eriksson & L. M. K. Vandersypen. "A programmable two-qubit quantum processor in silicon". *Nature* **555**, 633 (2018).

[21] M. T. Deng, S. Vaitiekenas, E. B. Hansen, J. Danon, M. Leijnse, K. Flensberg, J. Nygård, P. Krogstrup & C. M. Marcus. "Majorana bound state in a coupled quantum-dot hybrid-nanowire system". *Science* **354**, 1557–1562 (2016).

[22] H. Zhang, C.-X. Liu, S. Gazibegovic, D. Xu, J. A. Logan, G. Wang, N. van Loo, J. D. S. Bommer, M. W. A. de Moor, D. Car, R. L. M. Op het Veld, P. J. van Veldhoven, S. Koelling, M. A. Verheijen, M. Pendharkar, D. J. Pennachio, B. Shojaei, J. S. Lee, C. J. Palmstrøm, E. P. A. M. Bakkers, S. D. Sarma & L. P. Kouwenhoven. "Quantized Majorana conductance". *Nature* **556**, 74–79 (2018).

[23] F. Nichele, A. C. C. Drachmann, A. M. Whiticar, E. C. T. O'Farrell, H. J. Suominen, A. Fornieri, T. Wang, G. C. Gardner, C. Thomas, A. T. Hatke, P. Krogstrup, M. J. Manfra, K. Flensberg & C. M. Marcus. "Scaling of Majorana Zero-Bias Conductance Peaks". *Phys. Rev. Lett.* **119**, 136803 (2017).

[24] Q. L. He, L. Pan, A. L. Stern, E. C. Burks, X. Che, G. Yin, J. Wang, B. Lian, Q. Zhou, E. S. Choi, K. Murata, X. Kou, Z. Chen, T. Nie, Q. Shao, Y. Fan, S.-C. Zhang, K. Liu, J. Xia & K. L. Wang. "Chiral Majorana fermion modes in a quantum anomalous Hall insulator–superconductor structure". *Science* **357**, 294–299 (2017).

[25] D. Wang, L. Kong, P. Fan, H. Chen, S. Zhu, W. Liu, L. Cao, Y. Sun, S. Du, J. Schneeloch, R. Zhong, G. Gu, L. Fu, H. Ding & H.-J. Gao. "Evidence for Majorana bound states in an iron-based superconductor". *Science* (2018).

[26] K. A. Y. Bravyi S B. "Quantum codes on a lattice with boundary". *arXiv:9811052* (1998).

[27] E. Knill. "Quantum computing with realistically noisy devices." *Nature* **434**, 39–44 (2005).

[28] H. Bombin & M. A. Martin-Delgado. "Topological Quantum Distillation". *Phys. Rev. Lett.* **97**, 180501 (2006).

[29] B. Douçot & L. B. Ioffe. "Physical implementation of protected qubits". *Reports on Progress in Physics* **75**, 072001 (2012).

[30] A. Y. Kitaev. "Unpaired Majorana fermions in quantum wires". *Phys. Usp.* **44**, 131–136 (2001).

[31] P. Krogstrup, N. L. B. Ziino, W. Chang, S. M. Albrecht, M. H. Madsen, E. Johnson, J. Nygård, C. M. Marcus & T. S. Jespersen. "Epitaxy of semiconductor–superconductor nanowires". *Nature Materials* **14**, 400–406 (2015).

[32] R. Barends, J. Kelly, A. Megrant, A. Veitia, D. Sank, E. Jeffrey, T. C. White, J. Mutus, A. G. Fowler, B. Campbell, Y. Chen, Z. Chen, B. Chiaro, A. Dunsworth, C. Neill, P. O'Malley, P. Roushan, A. Vainsencher, J. Wenner, A. N. korotkov, A. N. Cleland & J. M. Martinis. "Superconducting quantum circuits at the surface code threshold for fault tolerance". *Nature* **508**, 500–503 (2014).

[33] J. Kelly, R. Barends, A. G. Fowler, A. Megrant, E. Jeffrey, T. C. White, D. Sank, J. Y. Mutus, B. Campbell, Y. Chen, Z. Chen, B. Chiaro, A. Dunsworth, I. C. Hoi, C. Neill, P. J. J. O'Malley, C. Quintana, P. Roushan, A. Vainsencher, J. Wenner, A. N. Cleland & J. M. Martinis. "State preservation by repetitive error detection in a superconducting quantum circuit". *Nature* **519**, 66–69 (2015).

[34] R. Versluis, S. Poletto, N. Khammassi, B. Tarasinski, N. Haider, D. J. Michalak, A. Bruno, K. Bertels & L. DiCarlo. "Scalable Quantum Circuit and Control for a Superconducting Surface Code". *Phys. Rev. Applied* **8**, 034021 (2017).

[35] S. Gladchenko, D. Olaya, E. Dupont-Ferrier, B. Douçot, L. B. Ioffe & M. E. Gershenson. "Superconducting nanocircuits for topologically protected qubits". *Nature Physics* **5**, 48–53 (2009).

[36] M. T. Bell, J. Paramanandam, L. B. Ioffe & M. E. Gershenson. "Protected Josephson Rhombus Chains". *Phys. Rev. Lett.* **112**, 167001 (2014).

[37] P. Groszkowski, A. D. Paolo, A. L. Grimsmo, A. Blais, D. I. Schuster, A. A. Houck & J. Koch. "Coherence properties of the 0-π qubit". *New Journal of Physics* **20**, 043053 (2018).

[38] T. W. Larsen. *Semiconductor-Nanowire-Based Superconducting Qubits and Gate-Tunable Couplings*. Master's thesis, University of Copenhagen (2016).

[39] M. A. Nielsen & I. L. Chuang. *Quantum Computation and Quantum Information*. 10th Anniversary Edition (Cambridge University Press, Cambridge, 2009).

[40] D. P. DiVincenzo. "Two-bit gates are universal for quantum computation". *Phys. Rev. A* **51**, 1015–1022 (1995).

[41] A. D. Córcoles, J. M. Gambetta, J. M. Chow, J. A. Smolin, M. Ware, J. Strand, B. L. T. Plourde & M. Steffen. "Process verification of two-qubit quantum gates by randomized benchmarking". *Phys. Rev. A* **87**, 030301 (2013).

[42] S. Pirandola, J. Eisert, C. Weedbrook, A. Furusawa & S. L. Braunstein. "Advances in quantum teleportation". *Nature Photonics* **9**, 641 (2015).

[43] B. M. Terhal. "Quantum error correction for quantum memories". *Rev. Mod. Phys.* **87**, 307–346 (2015).

[44] D. Gottesman. *Stabilizer Codes and Quantum Error Correction*. Ph.D. thesis, California Institute of Technology (1997).

[45] P. W. Shor. "Scheme for reducing decoherence in quantum computer memory". *Phys. Rev. A* **52**, R2493–R2496 (1995).

[46] A. G. Fowler, M. Mariantoni, J. M. Martinis & A. N. Cleland. "Surface codes: Towards practical large-scale quantum computation". *Phys. Rev. A* **86**, 032324 (2012).

[47] D. Poulin. "Optimal and efficient decoding of concatenated quantum block codes". *Phys. Rev. A* **74**, 052333 (2006).

[48] A. S. Darmawan & D. Poulin. "Linear-time general decoding algorithm for the surface code". *Phys. Rev. E* **97**, 051302 (2018).

[49] J. Alicea. "New directions in the pursuit of Majorana fermions in solid state systems". *Reports on Progress in Physics* **75**, 076501 (2012).

[50] R. M. Lutchyn, J. D. Sau & S. Das Sarma. "Majorana Fermions and a Topological Phase Transition in Semiconductor-Superconductor Heterostructures". *Phys. Rev. Lett.* **105**, 077001 (2010).

[51] Y. Oreg, G. Refael & F. von Oppen. "Helical Liquids and Majorana Bound States in Quantum Wires". *Phys. Rev. Lett.* **105**, 177002 (2010).

[52] S. Bravyi & A. Kitaev. "Universal quantum computation with ideal Clifford gates and noisy ancillas". *Phys. Rev. A* **71**, 022316 (2005).

[53] J. O'Gorman & E. T. Campbell. "Quantum computation with realistic magic-state factories". *Phys. Rev. A* **95**, 032338 (2017).

[54] M. Reiher, N. Wiebe, K. M. Svore, D. Wecker & M. Troyer. "Elucidating reaction mechanisms on quantum computers". *Proceedings of the National Academy of Sciences* **114**, 7555–7560 (2017).

[55] J. T. Anderson, G. Duclos-Cianci & D. Poulin. "Fault-Tolerant Conversion between the Steane and Reed-Muller Quantum Codes". *Phys. Rev. Lett.* **113**, 080501 (2014).

[56] H. Bombn. "Gauge color codes: optimal transversal gates and gauge fixing in topological stabilizer codes". *New Journal of Physics* **17**, 083002 (2015).

[57] A. Blais, R.-S. Huang, A. Wallraff, S. M. Girvin & R. J. Schoelkopf. "Cavity quantum electrodynamics for superconducting electrical circuits: An architecture for quantum computation". *Phys. Rev. A* **69**, 062320 (2004).

[58] S. M. Girvin. "Circuit QED: Superconducting Qubits Coupled to Microwave Photons". *Oxford University Press* (2011).

[59] U. Vool & M. Devoret. "Introduction to quantum electromagnetic circuits". *International Journal of Circuit Theory and Applications* **45**, 897–934 (2017).

[60] B. Vlastakis, G. Kirchmair, Z. Leghtas, S. E. Nigg, L. Frunzio, S. M. Girvin, M. Mirrahimi, M. H. Devoret & R. J. Schoelkopf. "Deterministically encoding quantum information using 100-photon Schrödinger cat states." *Science* **342**, 607–610 (2013).

[61] M. Mirrahimi, Z. Leghtas, V. V. Albert, S. Touzard, R. J. Schoelkopf, L. Jiang & M. H. Devoret. "Dynamically protected cat-qubits: a new paradigm for universal quantum computation". *New Journal of Physics* **16**, 045014 (2014).

[62] B. D. Josephson. "Possible new effects in superconductive tunnelling". *Phys. Lett.* **1**, 251–253 (1962).

[63] M. Tinkham. "Introduction to Superconductivity". Dover Publications (1996).

[64] Y. Nakamura, Y. A. Pashkin & J. S. Tsai. "Coherent control of macroscopic quantum states in a single-Cooper-pair box". *Nature* **398**, 786 (1999).

[65] D. Vion, A. Aassime, A. Cottet, P. Joyez, H. Pothier, C. Urbina, D. Esteve & M. H. Devoret. "Manipulating the Quantum State of an Electrical Circuit". *Science* **296**, 886–889 (2002).

[66] A. Wallraff, D. I. Schuster, A. Blais, L. Frunzio, R.-S. Huang, J. Majer, S. Kumar, S. M. Girvin & R. J. Schoelkopf. "Strong coupling of a single photon to a superconducting qubit using circuit quantum electrodynamics." *Nature* **431**, 162–167 (2004).

[67] J. Koch, T. Yu, J. Gambetta, A. Houck, D. Schuster, J. Majer, A. Blais, M. Devoret, S. Girvin & R. Schoelkopf. "Charge-insensitive qubit design derived from the Cooper pair box". *Phys. Rev. A* **76**, 042319 (2007).

[68] J. Schreier, A. Houck, J. Koch, D. Schuster, B. Johnson, J. Chow, J. Gambetta, J. Majer, L. Frunzio, M. Devoret, S. Girvin & R. Schoelkopf. "Suppressing charge noise decoherence in superconducting charge qubits". *Phys. Rev. B* **77**, 180502 (2008).

[69] J. M. Chow, J. M. Gambetta, L. Tornberg, J. Koch, L. S. Bishop, A. A. Houck, B. R. Johnson, L. Frunzio, S. M. Girvin & R. J. Schoelkopf. "Randomized Benchmarking and Process Tomography for Gate Errors in a Solid-State Qubit". *Phys. Rev. Lett.* **102**, 090502 (2009).

[70] F. Motzoi, J. M. Gambetta, P. Rebentrost & F. K. Wilhelm. "Simple Pulses for Elimination of Leakage in Weakly Nonlinear Qubits". *Phys. Rev. Lett.* **103**, 110501 (2009).

[71] J. M. Gambetta, F. Motzoi, S. T. Merkel & F. K. Wilhelm. "Analytic control methods for high-fidelity unitary operations in a weakly nonlinear oscillator". *Phys. Rev. A* **83**, 012308 (2011).

[72] M. Kjaergaard, F. Nichele, H. J. Suominen, M. P. Nowak, M. Wimmer, A. R. Akhmerov, J. A. Folk, K. Flensberg, J. Shabani, C. J. Palmstrm & C. M. Marcus. "Quantized conductance doubling and hard gap in a two-dimensional semiconductorsuperconductor heterostructure". *Nature Communications* **7**, 012308 (2016).

[73] T. W. Larsen, K. D. Petersson, F. Kuemmeth, T. S. Jespersen, P. Krogstrup, J. Nygård & C. M. Marcus. "Semiconductor-Nanowire-Based Superconducting Qubit". *Phys. Rev. Lett.* **115**, 127001 (2015).

[74] G. de Lange, B. van Heck, A. Bruno, D. J. van Woerkom, A. Geresdi, S. R. Plissard, E. P. A. M. Bakkers, A. R. Akhmerov & L. DiCarlo. "Realization of Microwave Quantum Circuits Using Hybrid Superconducting-Semiconducting Nanowire Josephson Elements". *Phys. Rev. Lett.* **115**, 127002 (2015).

[75] J. I.-J. Wang, D. Rodan-Legrain, L. Bretheau, D. L. Campbell, B. Kannan, D. Kim, M. Kjaergaard, P. Krantz, G. O. Samach, F. Yan, J. L. Yoder, K. Watanabe, T.

Taniguchi, T. P. Orlando, S. Gustavsson, P. Jarillo-Herrero & W. D. Oliver. "Quantum coherent control of a hybrid superconducting circuit made with graphene-based van der Waals heterostructures". *arXiv:1809.05215* (2018).

[76] L. Casparis, M. R. Connolly, M. Kjaergaard, N. J. Pearson, A. K. j, T. W. Larsen, F. Kuemmeth, T. Wang, C. Thomas, S. Gronin, G. C. Gardner, M. J. Manfra, C. M. Marcus & K. D. Petersson. "Superconducting gatemon qubit based on a proximitized two-dimensional electron gas". *Nature Nanotechnology* **13**, 915 (2018).

[77] J. G. Kroll, W. Uilhoorn, K. L. van der Enden, D. de Jong, K. Watanabe, T. Taniguchi, S. Goswami, M. C. Cassidy & L. P. Kouwenhoven. "A graphene transmon operating at 1 T". *arXiv:1806.10534* (2018).

[78] W. Chang, S. M. Albrecht, T. S. Jespersen, F. Kuemmeth, P. Krogstrup, J. Nygård & C. M. Marcus. "Hard gap in epitaxial semiconductor–superconductor nanowires". *Nature Nanotechnology* **10**, 232–236 (2015).

[79] S. Chuang, Q. Gao, R. Kapadia, A. C. Ford, J. Guo & A. Javey. "Ballistic InAs Nanowire Transistors". *Nano Letters* **13**, 555–558 (2013).

[80] A. Kringhøj, L. Casparis, M. Hell, T. W. Larsen, F. Kuemmeth, M. Leijnse, K. Flensberg, P. Krogstrup, J. Nygård, K. D. Petersson & C. M. Marcus. "Anharmonicity of a superconducting qubit with a few-mode Josephson junction". *Phys. Rev. B* **97**, 060508 (2018).

[81] C. W. J. Beenakker. "Universal limit of critical-current fluctuations in mesoscopic Josephson junctions". *Phys. Rev. Lett.* **67**, 3836–3839 (1991).

[82] A. A. Golubov, M. Y. Kupriyanov & E. Il'ichev. "The current-phase relation in Josephson junctions". *Rev. Mod. Phys.* **76**, 411–469 (2004).

[83] M. F. Goffman, C. Urbina, H. Pothier, J. Nygrd, C. M. Marcus & P. Krogstrup. "Conduction channels of an InAs-Al nanowire Josephson weak link". *New Journal of Physics* **19**, 092002 (2017).

[84] E. M. Spanton, M. Deng, S. Vaitieknas, P. Krogstrup, J. Nygrd, C. M. Marcus & K. A. Moler. "Currentphase relations of few-mode InAs nanowire Josephson junctions". *Nature Physics* **13**, 1177 (2017).

[85] D. J. van Woerkom, A. Proutski, B. van Heck, D. Bouman, J. I. Vyrynen, L. I. Glazman, P. Krogstrup, J. Nygrd, L. P. Kouwenhoven & A. Geresdi. "Microwave spectroscopy of spinful Andreev bound states in ballistic semiconductor Josephson junctions". *Nature Physics* **13**, 876 (2017).

[86] D. V. Averin. "Coulomb blockade in superconducting quantum point contacts". *Phys. Rev. Lett.* **82**, 3685 (1999).

[87] A. Wallraff, D. I. Schuster, A. Blais, L. Frunzio, J. Majer, M. H. Devoret, S. M. Girvin & R. J. Schoelkopf. "Approaching Unit Visibility for Control of a Superconducting Qubit with Dispersive Readout". *Phys. Rev. Lett.* **95**, 060501 (2005).

[88] A. Houck, J. Schreier, B. Johnson, J. Chow, J. Koch, J. Gambetta, D. Schuster, L. Frunzio, M. Devoret, S. Girvin & R. Schoelkopf. "Controlling the Spontaneous Emission of a Superconducting Transmon Qubit". *Phys. Rev. Lett.* **101**, 080502 (2008).

[89] D. I. Schuster, A. Wallraff, A. Blais, L. Frunzio, R.-S. Huang, J. Majer, S. M. Girvin & R. J. Schoelkopf. "ac Stark Shift and Dephasing of a Superconducting Qubit Strongly Coupled to a Cavity Field". *Phys. Rev. Lett.* **94**, 123602 (2005).

[90] D. I. Schuster, A. A. Houck, J. A. Schreier, A. Wallraff, J. M. Gambetta, A. Blais, L. Frunzio, J. Majer, B. Johnson, M. H. Devoret, S. M. Girvin & R. J. Schoelkopf. "Resolving photon number states in a superconducting circuit". *Nature* **445**, 515–518 (2007).

[91] D. Ristè, C. C. Bultink, K. W. Lehnert & L. DiCarlo. "Feedback Control of a Solid-State Qubit Using High-Fidelity Projective Measurement". *Phys. Rev. Lett.* **109**, 240502 (2012).

[92] Y. Salathé, P. Kurpiers, T. Karg, C. Lang, C. K. Andersen, A. Akin, S. Krinner, C. Eichler & A. Wallraff. "Low-Latency Digital Signal Processing for Feedback and Feedforward in Quantum Computing and Communication". *Phys. Rev. Applied* **9**, 034011 (2018).

[93] E. M. Purcell, H. C. Torrey & R. V. Pound. "Resonance Absorption by Nuclear Magnetic Moments in a Solid". *Phys. Rev.* **69**, 37–38 (1946).

[94] M. D. Reed, B. R. Johnson, A. A. Houck, L. DiCarlo, J. M. Chow, D. I. Schuster, L. Frunzio & R. J. Schoelkopf. "Fast reset and suppressing spontaneous emission of a superconducting qubit". *Applied Physics Letters* **96**, 203110 (2010).

[95] E. Jeffrey, D. Sank, J. Y. Mutus, T. C. White, J. Kelly, R. Barends, Y. Chen, Z. Chen, B. Chiaro, A. Dunsworth, A. Megrant, P. J. J. O'Malley, C. Neill, P. Roushan, A. Vainsencher, J. Wenner, A. N. Cleland & J. M. Martinis. "Fast Accurate State Measurement with Superconducting Qubits". *Phys. Rev. Lett.* **112**, 190504 (2014).

[96] E. A. Sete, J. M. Martinis & A. N. Korotkov. "Quantum theory of a bandpass Purcell filter for qubit readout". *Phys. Rev. A* **92**, 012325 (2015).

[97] N. T. Bronn, E. Magesan, N. A. Masluk, J. M. Chow, J. M. Gambetta & M. Steffen. "Reducing Spontaneous Emission in Circuit Quantum Electrodynamics by a Combined Readout/Filter Technique". *IEEE Transactions on Applied Superconductivity* **25**, 1–10 (2015).

[98] J. M. Chow, A. D. Córcoles, J. M. Gambetta, C. Rigetti, B. R. Johnson, J. A. Smolin, J. R. Rozen, G. A. Keefe, M. B. Rothwell, M. B. Ketchen & M. Steffen. "Simple All-Microwave Entangling Gate for Fixed-Frequency Superconducting Qubits". *Phys. Rev. Lett.* **107**, 080502 (2011).

[99] Y. Chen, C. Neill, P. Roushan, N. Leung, M. Fang, R. Barends, J. Kelly, B. Campbell, Z. Chen, B. Chiaro, A. Dunsworth, E. Jeffrey, A. Megrant, J. Y. Mutus, P. J. J. O'Malley, C. M. Quintana, D. Sank, A. Vainsencher, J. Wenner, T. C. White, M. R. Geller, A. N. Cleland & J. M. Martinis. "Qubit Architecture with High Coherence and Fast Tunable Coupling". *Phys. Rev. Lett.* **113**, 220502 (2014).

[100] N. J. S. Loft, M. Kjaergaard, L. B. Kristensen, C. K. Andersen, T. W. Larsen, S. Gustavsson, W. D. Oliver & N. T. Zinner. "High-fidelity conditional two-qubit swapping gate using tunable ancillas". *arxiv:1809.09049* (2018).

[101] F. Yan, P. Krantz, Y. Sung, M. Kjaergaard, D. Campbell, J. I. Wang, T. P. Orlando, S. Gustavsson & W. D. Oliver. "A tunable coupling scheme for implementing high-fidelity two-qubit gates". *arXiv:1803.09813* (2018).

[102] L. DiCarlo, J. M. Chow, J. M. Gambetta, L. S. Bishop, B. R. Johnson, D. I. Schuster, J. Majer, A. Blais, L. Frunzio, S. M. Girvin & R. J. Schoelkopf. "Demonstration of two-qubit algorithms with a superconducting quantum processor". *Nature* **460**, 240–244 (2009).

[103] J. M. Martinis & M. R. Geller. "Fast adiabatic qubit gates using only σ_z control". *Phys. Rev. A* **90**, 022307 (2014).

[104] A. Dewes, F. R. Ong, V. Schmitt, R. Lauro, N. Boulant, P. Bertet, D. Vion & D. Esteve. "Characterization of a Two-Transmon Processor with Individual Single-Shot Qubit Readout". *Phys. Rev. Lett.* **108**, 057002 (2012).

[105] J. Majer, J. M. Chow, J. M. Gambetta, J. Koch, B. R. Johnson, J. A. Schreier, L. Frunzio, D. I. Schuster, A. A. Houck, A. Wallraff, A. Blais, M. H. Devoret, S. M. Girvin & R. J. Schoelkopf. "Coupling superconducting qubits via a cavity bus". *Nature* **449**, 443–447 (2007).

[106] M. Reed. *Entanglement and Quantum Error Correction with Superconducting Qubits.* Ph.D. thesis, Yale University (2013).

[107] T. Tanamoto, K. Maruyama, Y.-x. Liu, X. Hu & F. Nori. "Efficient purification protocols using iSWAP gates in solid-state qubits". *Phys. Rev. A* **78**, 062313 (2008).

[108] J. Kelly, R. Barends, B. Campbell, Y. Chen, Z. Chen, B. Chiaro, A. Dunsworth, A. G. Fowler, I. C. Hoi, E. Jeffrey, A. Megrant, J. Mutus, C. Neill, P. J. J. O'Malley, C. Quintana, P. Roushan, D. Sank, A. Vainsencher, J. Wenner, T. C. White, A. N. Cleland & J. M. Martinis. "Optimal Quantum Control Using Randomized Benchmarking". *Phys. Rev. Lett.* **112**, 240504 (2014).

[109] A. Megrant, C. Neill, R. Barends, B. Chiaro, Y. Chen, L. Feigl, J. Kelly, E. Lucero, M. Mariantoni, P. J. J. OMalley, D. Sank, A. Vainsencher, J. Wenner, T. C. White, Y. Yin, J. Zhao, C. J. Palmstrm, J. M. Martinis & A. N. Cleland. "Planar superconducting resonators with internal quality factors above one million". *Applied Physics Letters* **100**, 113510 (2012).

[110] Z. Chen, A. Megrant, J. Kelly, R. Barends, J. Bochmann, Y. Chen, B. Chiaro, A. Dunsworth, E. Jeffrey, J. Y. Mutus, P. J. J. O'Malley, C. Neill, P. Roushan, D. Sank, A. Vainsencher, J. Wenner, T. C. White, A. N. Cleland & J. M. Martinis. "Fabrication and characterization of aluminum airbridges for superconducting microwave circuits". *Applied Physics Letters* **104**, 052602 (2014).

[111] A. Bruno, G. de Lange, S. Asaad, K. L. van der Enden, N. K. Langford & L. DiCarlo. "Reducing intrinsic loss in superconducting resonators by surface treatment and deep etching of silicon substrates". *Applied Physics Letters* **106**, 182601 (2015).

[112] C. Wang, C. Axline, Y. Y. Gao, T. Brecht, Y. Chu, L. Frunzio, M. H. Devoret & R. J. Schoelkopf. "Surface participation and dielectric loss in superconducting qubits". *Applied Physics Letters* **107**, 162601 (2015).

[113] F. Luthi, T. Stavenga, O. W. Enzing, A. Bruno, C. Dickel, N. K. Langford, M. A. Rol, T. S. Jespersen, J. Nygård, P. Krogstrup & L. DiCarlo. "Evolution of Nanowire Transmon Qubits and Their Coherence in a Magnetic Field". *Phys. Rev. Lett.* **120**, 100502 (2018).

[114] W. Chang. *Superconducting Proximity Effect in InAs Nanowires.* Ph.D. thesis, Harvard University (2014).

[115] A. D. Crcoles, J. M. Chow, J. M. Gambetta, C. Rigetti, J. R. Rozen, G. A. Keefe, M. Beth Rothwell, M. B. Ketchen & M. Steffen. "Protecting superconducting qubits from radiation". *Applied Physics Letters* **99**, 181906 (2011).

[116] R. Barends, J. Wenner, M. Lenander, Y. Chen, R. C. Bialczak, J. Kelly, E. Lucero, P. OMalley, M. Mariantoni, D. Sank, H. Wang, T. C. White, Y. Yin, J. Zhao, A. N. Cleland, J. M. Martinis & J. J. A. Baselmans. "Minimizing quasiparticle generation from stray infrared light in superconducting quantum circuits". *Applied Physics Letters* **99**, 113507 (2011).

[117] D. Schuster. *Circuit Quantum Electrodynamics.* Ph.D. thesis, Yale University (2007).

[118] L. Casparis, T. W. Larsen, M. S. Olsen, F. Kuemmeth, P. Krogstrup, J. Nygård, K. D. Petersson & C. M. Marcus. "Gatemon Benchmarking and Two-Qubit Operations". *Phys. Rev. Lett.* **116**, 150505 (2016).

[119] A. A. AU Houck, D. I. Schuster, J. M. Gambetta, J. A. Schreier, B. R. Johnson, J. M. Chow, L. Frunzio, J. Majer, M. H. Devoret, S. M. Girvin & R. J. Schoelkopf. "Generating single microwave photons in a circuit". *Nature* **449**, 328 (2007).

[120] u. Cywiński. "Dynamical-decoupling noise spectroscopy at an optimal working point of a qubit". *Phys. Rev. A* **90**, 042307 (2014).

[121] I. L. Chuang & M. A. Nielsen. "Prescription for experimental determination of the dynamics of a quantum black box". *Journal of Modern Optics* **44**, 2455–2467 (1997).

[122] R. Bhandari & N. A. Peters. "On the general constraints in single qubit quantum process tomography". *Scientific Reports* **6**, 26004 (2016).

[123] E. Magesan, J. M. Gambetta, B. R. Johnson, C. A. Ryan, J. M. Chow, S. T. Merkel, M. P. da Silva, G. A. Keefe, M. B. Rothwell, T. A. Ohki, M. B. Ketchen & M. Steffen. "Efficient Measurement of Quantum Gate Error by Interleaved Randomized Benchmarking". *Phys. Rev. Lett.* **109**, 080505 (2012).

[124] P. J. J. O'Malley, J. Kelly, R. Barends, B. Campbell, Y. Chen, Z. Chen, B. Chiaro, A. Dunsworth, A. G. Fowler, I.-C. Hoi, E. Jeffrey, A. Megrant, J. Mutus, C. Neill, C. Quintana, P. Roushan, D. Sank, A. Vainsencher, J. Wenner, T. C. White, A. N. Korotkov, A. N. Cleland & J. M. Martinis. "Qubit Metrology of Ultralow Phase Noise Using Randomized Benchmarking". *Phys. Rev. Applied* **3**, 044009 (2015).

[125] L. Casparis, N. J. Pearson, A. K. j, T. W. Larsen, F. Kuemmeth, J. N. rd, P. Krogstrup, K. D. Petersson & C. M. Marcus. "Voltage-Controlled Superconducting Quantum Bus". *arXiv:1802.01327* (2018).

[126] A. Kitaev. "Protected qubit based on a superconducting current mirror". *arXiv:0609441* (2006).

[127] P. Brooks, A. Kitaev & J. Preskill. "Protected gates for superconducting qubits". *Phys. Rev. A* **87**, 052306 (2013).

[128] B. Douçot & J. Vidal. "Pairing of Cooper Pairs in a Fully Frustrated Josephson-Junction Chain". *Phys. Rev. Lett.* **88**, 227005 (2002).

[129] C. W. J. Beenakker & H. van Houten. "The Superconducting Quantum Point Contact". 481–497 (Elsevier, 1992).

[130] Y.-H. Lin, L. B. Nguyen, N. Grabon, J. San Miguel, N. Pankratova & V. E. Manucharyan. "Demonstration of Protection of a Superconducting Qubit from Energy Decay". *Phys. Rev. Lett.* **120**, 150503 (2018).

[131] N. Earnest, S. Chakram, Y. Lu, N. Irons, R. K. Naik, N. Leung, L. Ocola, D. A. Czaplewski, B. Baker, J. Lawrence, J. Koch & D. I. Schuster. "Realization of a Λ System with Metastable States of a Capacitively Shunted Fluxonium". *Phys. Rev. Lett.* **120**, 150504 (2018).

[132] A. E. Antipov, A. Bargerbos, G. W. Winkler, B. Bauer, E. Rossi & R. M. Lutchyn. "Effects of Gate-Induced Electric Fields on Semiconductor Majorana Nanowires". *Phys. Rev. X* **8**, 031041 (2018).

[133] S. Vaitiekėnas, M.-T. Deng, J. Nygård, P. Krogstrup & C. M. Marcus. "Effective g Factor of Subgap States in Hybrid Nanowires". *Phys. Rev. Lett.* **121**, 037703 (2018).

[134] N. Didier, J. Bourassa & A. Blais. "Fast Quantum Nondemolition Readout by Parametric Modulation of Longitudinal Qubit-Oscillator Interaction". *Phys. Rev. Lett.* **115**, 203601 (2015).

[135] T. Karzig, C. Knapp, R. M. Lutchyn, P. Bonderson, M. B. Hastings, C. Nayak, J. Alicea, K. Flensberg, S. Plugge, Y. Oreg, C. M. Marcus & M. H. Freedman. "Scalable designs for quasiparticle-poisoning-protected topological quantum computation with Majorana zero modes". *Phys. Rev. B* **95**, 235305 (2017).

[136] S. Plugge, A. Rasmussen, R. Egger & K. Flensberg. "Majorana box qubits". *New Journal of Physics* **19**, 012001 (2017).

[137] V. Mourik, K. Zuo, S. M. Frolov, S. R. Plissard, E. P. A. M. Bakkers & L. P. Kouwenhoven. "Signatures of Majorana Fermions in Hybrid Superconductor-Semiconductor Nanowire Devices". *Science* **336**, 1003–1007 (2012).

[138] S. M. Albrecht, A. P. Higginbotham, M. Madsen, F. Kuemmeth, T. S. Jespersen, J. Nygård, P. Krogstrup & C. M. Marcus. "Exponential protection of zero modes in Majorana islands". *Nature* **531**, 206–209 (2016).

[139] D. Aasen, M. Hell, R. V. Mishmash, A. Higginbotham, J. Danon, M. Leijnse, T. S. Jespersen, J. A. Folk, C. M. Marcus, K. Flensberg & J. Alicea. "Milestones Toward Majorana-Based Quantum Computing". *Phys. Rev. X* **6**, 031016 (2016).

[140] E. Ginossar & E. Grosfeld. "Microwave transitions as a signature of coherent parity mixing effects in the Majorana-transmon qubit". *Nature Communications* **5**, 4772 (2014).

[141] K. Yavilberg, E. Ginossar & E. Grosfeld. "Fermion parity measurement and control in Majorana circuit quantum electrodynamics". *Phys. Rev. B* **92**, 075143 (2015).

[142] J. G. Kroll, F. Borsoi, K. L. van der Enden, W. Uilhoorn, D. de Jong, M. Quintero-Prez, D. J. van Woerkom, A. Bruno, S. R. Plissard, D. Car, E. P. A. M. Bakkers, M. C. Cassidy & L. P. Kouwenhoven. "Magnetic field resilient superconducting coplanar waveguide resonators for hybrid cQED experiments". *arXiv:1809.03932* (2018).

[143] X. Mi, J. V. Cady, D. M. Zajac, J. Stehlik, L. F. Edge & J. R. Petta. "Circuit quantum electrodynamics architecture for gate-defined quantum dots in silicon". *Applied Physics Letters* **110**, 043502 (2017).

[144] O. Erlandsson. *Circuit QED devices for probing Majorana zero modes.* Master's thesis, Lund University and University of Copenhagen (2018).

[145] G. W. Winkler, A. E. Antipov, B. van Heck, A. A. Soluyanov, L. I. Glazman, M. Wimmer & R. M. Lutchyn. "A unified numerical approach to semiconductor-superconductor heterostructures". *arXiv:1810.04180* (2018).

[146] S. Vaitieknas, M.-T. Deng, P. Krogstrup & C. M. Marcus. "Flux-induced Majorana modes in full-shell nanowires". *arXiv:1809.05513* (2018).

[147] R. M. Lutchyn, G. W. Winkler, B. van Heck, T. Karzig, K. Flensberg, L. I. Glazman & C. Nayak. "Topological superconductivity in full shell proximitized nanowires". *arXiv:1809.05512* (2018).

[148] C. Janvier, L. Tosi, L. Bretheau, Ç. Ö. Girit, M. Stern, P. Bertet, P. Joyez, D. Vion, D. Esteve, M. F. Goffman, H. Pothier & C. Urbina. "Coherent manipulation of Andreev states in superconducting atomic contacts". *Science* **349**, 1199 (2015).

[149] M. Hays, G. de Lange, K. Serniak, D. J. van Woerkom, D. Bouman, P. Krogstrup, J. Nygård, A. Geresdi & M. H. Devoret. "Direct Microwave Measurement of Andreev-Bound-State Dynamics in a Semiconductor-Nanowire Josephson Junction". *Phys. Rev. Lett.* **121**, 047001 (2018).

[150] D. J. van Woerkom, A. Proutski, B. van Heck, D. Bouman, J. I. Väyrynen, L. I. Glazman, P. Krogstrup, J. Nygård, L. P. Kouwenhoven & A. Geresdi. "Microwave spectroscopy of spinful Andreev bound states in ballistic semiconductor Josephson junctions". *Nature Physics* **13**, 876–881 (2017).

[151] A. Imamoğlu. "Cavity QED Based on Collective Magnetic Dipole Coupling: Spin Ensembles as Hybrid Two-Level Systems". *Phys. Rev. Lett.* **102**, 083602 (2009).